



**Università
degli Studi
di Ferrara**

DOTTORATO DI RICERCA in FISICA

CICLO XXXVI

COORDINATRICE Prof.ssa LUPPI Eleonora



Instrumentation for advanced Quantum Chromodynamics studies with flavor sensitivity

Settore Scientifico Disciplinare FIS/04

Dottorando

Dott. Vallarino Simone

Tutore

Prof. Contalbrigo Marco

ANNI 2020/2024

Contents

Scientific motivation	v
1 Investigate the non-perturbative QCD	1
1.1 Introduction	1
1.2 Measuring the Transverse-Momentum-Dependent distribution	6
1.3 Polarized Semi-Inclusive Deep Inelastic Scattering	10
1.4 Beam-Spin Asymmetry	12
2 The Ring Imaging Cherenkov detector for CLAS12	15
2.1 The CLAS12 spectrometer at Jefferson Lab	15
2.1.1 The detector	17
2.2 The CLAS12 Ring Imaging Cherenkov	19
2.2.1 RICH design	20
2.2.2 The radiator	21
2.2.3 The mirror system	22
2.2.4 The photon detector	24
2.3 The assembly and commissioning of the second module of the RICH	27
2.4 RICH efficiency in cleaning the kaon sample	31
3 SIDIS with CLAS12	41
3.1 Data	41
3.1.1 The CLAS12 SIDIS cuts	42
3.1.2 Binning	48
3.2 Analysis	48
3.2.1 The Unbinned Maximum Likelihood Fit	50
3.2.2 UML fit validation	51
3.3 Results	53
3.3.1 One-dimensional results	53
3.3.2 Four-dimensional results	53
3.3.3 Future SIDIS studies using the CLAS12 RICH	53

4 The EPIC dual-radiator RICH	59
4.1 The EPIC experiment at the Electron-Ion Collider	59
4.2 The recovery of SiPM radiation damage via annealing	65
4.3 The dual-radiator RICH prototype	67
4.3.1 Design	69
4.3.2 Aerogel characterization	72
4.3.3 Simulation	77
4.3.4 Test beams	77
4.4 Results of the prototype studies	85
4.4.1 Resolution expected and achieved	85
4.4.2 Aerogel study with the prototype	87
4.4.3 Studies using the beam PID system	92
4.5 Conclusions	92
Conclusions	101
Acronyms	103

Scientific motivation

Chapter 1

Investigate the non-perturbative QCD

This Chapter introduces non-perturbative Quantum Chromodynamics (QCD), outlining the importance of performing accurate measures of polarized Semi-Inclusive Deep Inelastic Scattering (SIDIS) to understand the internal structure of the nucleon deeply. It describes how the Beam-Spin Asymmetry (BSA) measurements permit access to the Transverse-Momentum-Dependent distributions (TMDs), which represent the three-dimensional imaging of nucleons. Finally, the instrumentation needed to perform this kind of measurement is introduced.

1.1 Introduction

Close to the ~~half of the~~ 20th century, the invention of the cyclotron and synchrotron ~~provided~~ new possibilities for scientists to investigate the nature of nucleons. Simultaneously, the invention of the bubble chamber as the first modern detector allowed the so-called “particle explosion”, meaning the discovery of many new particles in a few years. They include a lot of unstable particles and few ~~stables~~, all generically termed hadrons. This evidence suggested they are bound states of ~~more~~ elementary particles, and the unstable had a decay channel, unlike the stables. In trying to classify them, both Gell-Mann¹ and Ne’eman² developed the eight-fold way of inserting the light hadrons and meson into multiples of flavor SU(3). Gell-Mann and Zweig³ completed this idea by introducing the Quark Model (QM), which describes the mesons as bound states of quark and anti-quark pair and the

¹Murray Gell-Mann, September 15, 1929, Manhattan, New York City, U.S. - May 24, 2019, Santa Fe, New Mexico, U.S.; Winner of 1969 Nobel Prize in Physics.

²Yuval Ne’eman, 14 May 1925, Tel Aviv, Mandatory Palestine - 26 April 2006 Tel Aviv, Israel.

³George Zweig, May 20, 1937, Moscow, Russian SFSR, Soviet Union.

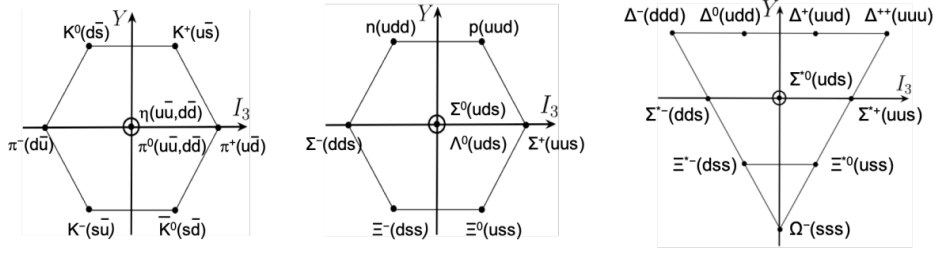


Figure 1.1: Representation of the Quark Model.

baryons as bound states of three quarks with different flavors *up*, *down*, and *strange* (u,d,s) as represented in Figure 1.1.

The QM was initially treated as a mathematical trick permitting the description of several particles, but the existence of elementary components of hadrons with spin- $\frac{1}{2}$ and fractional charge was not accepted. Moreover, the original version showed issues with not-trivial solutions, for example, the $\Delta^{++}(1232)$ baryon: it was a bound state of three up quarks uuu . It was a fermion described by a wave function symmetric under the exchange of any two quarks, assuming that the elementary particles in the fundamental state described by S-wave. Introducing a new quantum number called color permitted the solution to this issue. Indeed, assuming three possible color states, like the fundamental color *red*, *green*, and *blue*, the Δ^{++} wave functions became antisymmetric under the exchange of two quarks with different colors, as required for fermions. In 1964, this was the first step into Quantum Chromodynamics (QCD), the most modern theory describing the nucleon structure [13, 14]. A side effect of introducing the color quantum number was the expectation of eight colored statuses for each meson that were not observed. Moreover, it turned out to be completely impossible to isolate and detect individual quarks, requiring the addition of other constraints in the theory. The continuous necessity of introducing new hypotheses to solve the issues caused widespread skepticism toward the theory.

In 1969, there was a breakthrough due to the analysis of Deep Inelastic Scattering (DIS) data produced at Stanford Linear Accelerator Center (SLAC) by Bjorken⁴ and Feynman⁵. The confirmed nucleon contains point-like spin- $\frac{1}{2}$ particles, providing the first experimental measurement of the quark's existence. The DIS is the scattering of lepton l over a nucleon N , on which the scattered lepton is detected

$$\ell(l) + N(P) \rightarrow \ell(l') + X \quad (1.1)$$

where the quantities in parenthesis are the particles' momentum. A scheme

⁴June 22, 1934, Chicago, Illinois, United States

⁵Richard Phillips Feynman, May 11, 1918, New York City, U.S. - February 15, 1988, Los Angeles, California, U.S.; Winner of the 1964 Nobel Prize in Physics

of the DIS is shown in Figure 1.2a. Measuring the scattered lepton makes it possible to define the momentum transferred from the probe in the collision as

$$q = l - l' \quad (1.2)$$

and then defining the invariant momentum transferred

$$Q = \sqrt{-q^2} \quad (1.3)$$



If $Q \gg \frac{1}{R}$, where R is the proton radius, the Deep Inelastic Scattering (DIS) can be described as the short-range interaction of the electron with a point-like constituent of the nucleon. Feynman called these point-like spin- $\frac{1}{2}$ objects partons, building the Parton Model (PM). In this model, Feynman describes the DIS cross-section in the infinite momentum frame, where the partons are moving collinear, bringing a fraction of the total nucleon momentum x , and provides a formula to compute it:

$$E' \frac{d\sigma_{ep \rightarrow e'X}}{d^3l'} \approx \sum_i \left\{ \frac{2\alpha^2}{Q^2(\ell + P)^2} \left[\frac{1 + (1 - y)^2}{y} \right] \right\} f_{i/p}(x) \quad (1.4)$$



where the sum is over all the possible quarks, α is the electromagnetic fine constant, e is the fractional charge of the parton, $y = \frac{P \cdot q}{P \cdot \ell}$ is the fraction of energy loss by the lepton, and $x = x_B = \frac{Q^2}{2P \cdot q}$ is the Bjorken variable representing the fraction of the nucleon momentum carried by the parton.



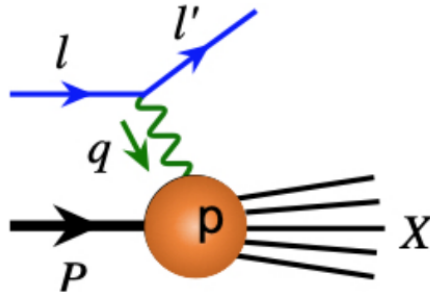
The most interesting term is the function $f_{i/p}(x)$, which represents the probability of finding a parton carrying a fraction x of the nucleon momentum. In the PM, these functions $f_{i/p}(x)$ take the name of Parton Distribution Functions (PDFs). From this formula, it is possible to show that the DIS cross-section is independent of transferred momentum but depends only on x_B , a phenomenon known as Bjorken scaling and experimentally verified at SLAC. These measurements provided the first credibility to the quark idea, pushing forward in the direction of theorizing the Quark Parton Model (QPM).

An independent confirmation of the QPM became from the so-called Drell-Yan process, the production of a lepton pair from the scattering of two hadrons:

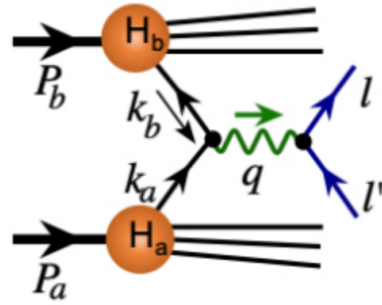
$$H_a + H_b \rightarrow l + \bar{l} \quad (1.5)$$

By describing it as the annihilation of a quark and anti-quark, it was possible to compute the expectation value of the cross-section using the PDFs obtained by the DIS measurement. Except for a kinematic factor ~ 2 , the theoretical and experimental cross-sections were found to be the same.

The QPM was a significant step toward understanding the nucleon's inner structure, but a new and more general gauge theory was developed: the Quantum Chromodynamics (QCD), where the quarks are held together by the gluons, the boson mediating the strong color force. In QCD, the nucleon



(a) Diagram of the Deep Inelastic Scattering.



(b) Diagram of the Drell-Yan process.

is described as a relativistic bound state of quarks and gluons, referred to collectively as partons. Despite more than fifty years of studies, there are still outstanding questions in QCD. Two of the most surprising effects of the QCD are the *color confinement*, which implies that a struck quark in the scattering process will generate new particles to obtain a colorless final state, and the *asymptotic freedom*, which made the strong force weakly coupled at a sufficiently short distance. The former automatically solves the impossibility of isolating the partons, causing the so-called process of “hadronization” on which a struck quark, ejected from the nucleon, generates other quarks and anti-quarks, forming a new hadron. The latter makes it possible to use the theoretical formalism of QCD factorization, which permits linking the quarks and gluons to the final states measured at modern high-energy physics experiments via a well-defined set of distribution functions encoding information on nucleon’s structure. The precise knowledge of these distributions provided by the experimental data permits exploring the quarks’ and gluons’ dynamics, accessing the nucleon structure, even without effectively “seeing” the quarks. As a direct consequence of asymptotic freedom, the perturbation theory is applicable in the high energy scale to evaluate the dynamic of strong interactions. This led to fundamental measurements in understanding the nature surrounding us; for example, the discovery of the Higgs boson occurred in 2012.



QCD is a quantum field theory, and its Lagrange density is built on two kinds of particle fields: the spin- $\frac{1}{2}$ Dirac fields ψ_f^i and the massless spin-1 vector field A_μ^a . The former is associated with the quarks, i can assume the value of the three colors *red*, *green*, and *blue*, and f is the six flavors of quarks *up*, *down*, *strange*, *charm*, *bottom*, and *top*. The latter is associated with the gluons, a can assume eight possible values corresponding to the square of the number of colors minus one. Having a SU(3) symmetry, the Lagrange

density is:

$$\mathcal{L}_{QCD}(\psi_f, A_\mu) = -\frac{1}{4}G_{\mu\nu,a}^2[A] + \sum_f \bar{\psi}_f (iD_\mu[A]\gamma^\mu - m_f) \psi_f \quad (1.6)$$

where the gluon field strength $G_{\mu\nu,a}[A]$ and the covariant derivative $D_\mu[A]$ contain the strong coupling constant, and the generator and structure constant defining the SU(3) color algebra. The QCD is a renormalizable theory, and ~~then~~ it is characterized by a running coupling $\alpha(\mu)$ depending on the energy scale at which the interaction is probed. Differently from the electromagnetic interaction, the $\alpha(\mu)$ decreases for increasing μ , ~~then~~ the strong interaction became weaker at a short distance or high ~~momentum transferred~~. This property is closely linked to the asymptotic freedom, making it possible to use the perturbation theory to describe the QCD dynamics at short distances.

The ~~nucleon internal strong interactions~~ occur in the scale of $\Lambda_{QCD} \sim 200$ MeV, making the coupling constant so large ~~and~~ the perturbation theory ~~not~~ applicable. It means that the ~~cross-section of scattering involving hadron~~ can not be computed using only the perturbative QCD. In the QPM, the information of non-perturbative components of the hadron is embedded inside the PDFs, while QCD factorization enables the systematic separation of physical phenomena occurring at distinct momentum scales. In particular, the nucleon's internal structure can be described by the matrix elements of gauge-invariant partonic operators composed of quark and gluon fields with different spin projections. These matrix elements are not observables, as could be expected for the color confinement, but the QCD factorization links them to measurable cross-sections.

Probing via scattering the spin- $\frac{1}{2}$ quark carrying momentum x , ~~four~~ possible polarization states can be ~~accessed~~: unpolarized, longitudinally, ~~and the two transverse direction polarization~~. Considering a spin- $\frac{1}{2}$ nucleon, three leading order collinear PDFs can be defined: the *unpolarized* collinear quark distribution of an unpolarized nucleon $f_{q/h}(x)$, the collinear quark *helicity* distribution of a longitudinally polarized nucleon $\Delta f_{q/h}(x)$, and the collinear *transversity* distribution of a transversely polarized nucleon ~~with the direction of quark transverse polarization parallel to the direction of nucleon's polarization~~ $\delta f_{q/h}(x)$ ⁶. The first is well-determined from experimental data, while precise measurements of the others are expected from ~~the~~ JLab and EIC.

~~Considering~~ scattering with high transferred momentum $Q \gg \frac{1}{R}$, ~~it~~ is not sensitive to the physics at the scale of $\Lambda_{QCD} \sim \frac{1}{R}$, including the parton confined transverse motion in the momentum space and its spatial distribution in position space. A high Q is needed to localize the parton and permit the probe to see it. On the other hand, a secondary $Q_2 \ll Q_1$ soft momentum scale ~~is~~ needed to access ~~the other~~ dimensions ~~than~~ the collinear momentum

⁶In literature, it is also written as $h_1(x)$ or $\delta q(x)$

space. Two different scales remain possible for the QCD factorization. For example, the Drell-Yan cross-section is a two-scale observable: by measuring it as a function of the module of the pair's transverse momentum $q_T = |\mathbf{q}_T|$ in addition to the invariant mass of the lepton pair Q . The \mathbf{q}_T is constituted by the sum of the transverse momentum components of the annihilated pair of quark and anti-quark, providing direct access to the transverse momentum of the quarks. The cross-section formula depends on $f_1(x_a, \mathbf{k}_{aT})$, a Transverse-Momentum-Dependent distribution (TMD) associated with the parton.

Accessing the two different scales allows us to define a class of functions called TMDs, similar to the PDFs, but providing the probability density of finding a parton carrying a fraction of the longitudinal momentum x and transverse momentum \mathbf{k}_T inside the nucleon. Then the TMDs provided more information on the three-dimensional hadron structure rather than the simple collinear PDFs. There are also TMDs not having a correspondent one-dimensional PDF; for example, the *Sivers function* $f_{1T}^\perp(x, \mathbf{k}_T)$ represents the correlation between the direction of the transverse spin of the nucleon and the direction of transverse motion of an unpolarized active quark, as well as its flavor dependence. Another example is the *pretzelosity* $h_{1T}^\perp(x, \mathbf{k}_T)$ representing how the nucleon spin and quark spin correlation can influence the quark's transverse motion: its moment in a model-dependent way can be interpreted as the contribution to the proton's spin of the quark orbital angular momentum.

Considering nucleon' and quark' spin polarization, eight TMDs can be defined. A scheme linking the TMD with the spins polarization is shown in Figure 1.3. Similar TMDs exist for anti-quark and gluon.

1.2 Measuring the Transverse-Momentum-Dependent distribution

The QCD factorization implies the possibility of accessing the three-dimensional nucleon structure via the TMDs measurement, relating them to physical observables, as described before for the Drell-Yan process. Despite this, the Drell-Yan process does not permit the disentangling of the different quarks' contribution or accessing to the gluon TMDs. A more well defined and factorizable two-scales observable is the polarized Semi-Inclusive Deep Inelastic Scattering (SIDIS), a polarized lepton ℓ hitting a polarized nucleon target N and produces a final state including the scattered lepton and at least one measured hadron H

$$\ell + N \rightarrow \ell + H + X \quad (1.7)$$

It can be described by the scheme shown in Figure 1.4. In this case, the hard scale is the transferred momentum $Q \gg \Lambda_{QCD}$, and the soft scale is the transverse momentum of the hadron observed in the final state $p_{H,T}$. Then SIDIS is another two-scale observable permitting access to the three-dimensional

Leading Quark TMDPDFs  Nucleon Spin  Quark Spin



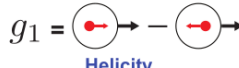

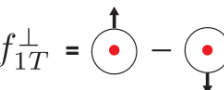
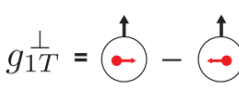


		Quark Polarization		
		Un-Polarized (U)	Longitudinally Polarized (L)	Transversely Polarized (T)
Nucleon Polarization	U	$f_1 = \text{Unpolarized}$ 		$h_1^\perp = \text{Boer-Mulders}$ 
	L		$g_1 = \text{Helicity}$ 	$h_{1L}^\perp = \text{Worm-gear}$ 
	T	$f_{1T}^\perp = \text{Sivers}$ 	$g_{1T}^\perp = \text{Worm-gear}$ 	$h_1 = \text{Transversity}$  $h_{1T}^\perp = \text{Pretzelosity}$ 

Figure 1.3: Recap of the Transverse-Momentum-Dependent distribution PDFs as a function of nucleon and quark polarization.

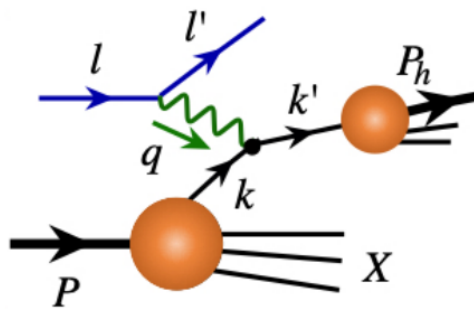




Figure 1.4: Scheme of the Semi-Inclusive Deep Inelastic Scattering (SIDIS).

Leading Quark TMDFFs  Hadron Spin  Quark Spin

		Quark Polarization		
		Un-Polarized (U)	Longitudinally Polarized (L)	Transversely Polarized (T)
Polarized Hadrons	L		$G_1 = \text{---} \text{---} \text{---}$ Helicity	$H_{1L}^\perp = \text{---} \text{---}$
	T	$D_{1T}^\perp = \text{---} \text{---}$ Polarizing FF	$G_{1T}^\perp = \text{---} \text{---}$	$H_1 = \text{---} \text{---}$ Transversity $H_{1T}^\perp = \text{---} \text{---}$
Unpolarized (or Spin 0) Hadrons		$D_1 = \text{---}$ Unpolarized		$H_1^\perp = \text{---} \text{---}$ Collins

Figure 1.5: Recap of the Transverse-Momentum-Dependent distributions as a function of nucleon and quark polarization.

structure of the nucleon. Writing the SIDIS cross-section regarding TMDs, it is necessary to introduce a new kind of distribution depending on the quark transverse momentum, the TMD Fragmentation Functions (FFs) $D_{h/q}(\zeta, \mathbf{k}'_T)$. They represent the probability of a quark q to hadronize in the hadron h carrying the momentum fraction ζ of the fragmenting quark momentum. Usually, the acronym TMDs includes both the TMD PDFs, describing the probability of finding a quark with a certain momentum inside the hadron, and the TMD FFs. As for TMD PDFs, it is possible to define eight leading-order TMD FFs for the quark, that are reported in Figure 1.5, as well it is possible to define the TMD FFs for anti-quark and gluon.

Another access to TMDs can be obtained by studying the di-hadron production in e^+e^- collisions

$$e^+ + e^- \rightarrow H_1(P_1) + H_2(P_2) + X \quad (1.8)$$

When the hadrons are almost back-to-back the momentum imbalance $\bar{p} = |\vec{P}_1 + \vec{P}_2| \ll \frac{|\vec{P}_1 + \vec{P}_2|}{2} = \bar{P}$ defines a soft-scale in addition to the hard scale of the invariant mass of the pair, providing a third possible channel to investigate the nucleon structure.

The TMDs are classified in terms of the correlation of polarization of partons and hadron polarization, then asymmetries of cross-sections with polarized beams can provide more independent observables from the three

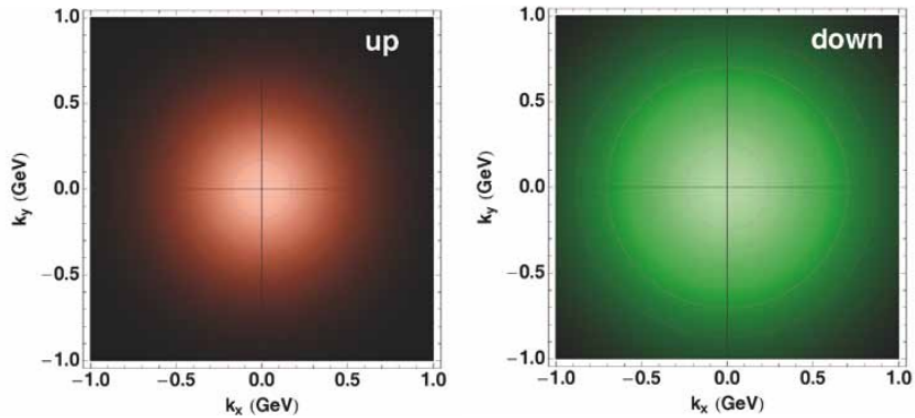


Figure 1.6: Distribution of up and down-quark transverse momentum. The down-quark distribution is larger than the top-quark.

classical two-scale observables alone. The TMDs can be accessed experimentally and are subject to intense studies at past, present, and future DIS experiments, like HERMES at DESY, COMPASS at CERN, CLAS12 and Hall A at Jefferson Lab, and the new Electron-Ion Collider (EIC) at Brookhaven National Laboratory.

Observing the target from the point of view of the probe, it does not look spherical but rather like a flat disk for the Lorentz contraction. Many questions about TMDs are currently unanswered; for example, it is unclear if the parton density in momentum space is higher in the disk's center and decreases monotonically to the edge or decreases in the center. The distributions change depending on the energy scale of the probe and on the value of the longitudinal fractional momentum. It is also unknown if there is a difference in the distribution of partons with different flavors. For example, it is unknown if one flavor is more concentrated in the center and the other on the sides, or if the flavors are uniformly mixed. There are first indications that the up-quark distribution is closer to the center of the nucleon than the down-quark distribution, as shown in Figure 1.6.

The introduction as a variable of the nucleon's spin direction causes even more strange effects. Suppose the nucleon's spin is moving toward us, and its spin is pointing upwards: it turns out that the up-quarks move preferentially to the right and down-quarks to the left, as shown in Figure 1.7. These distributions are not cylindrical symmetric in the momentum space.

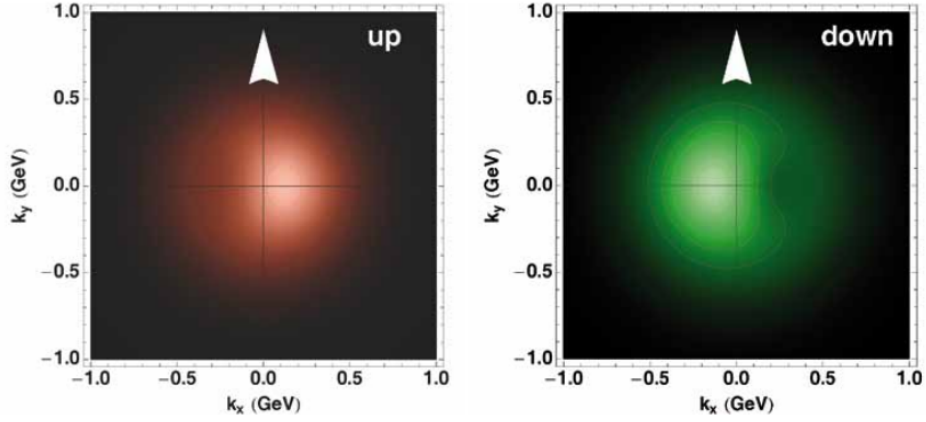


Figure 1.7: Distribution of up and down-quark transverse momentum, if the nucleon spin is pointing upward and the nucleon comes out of the paper.

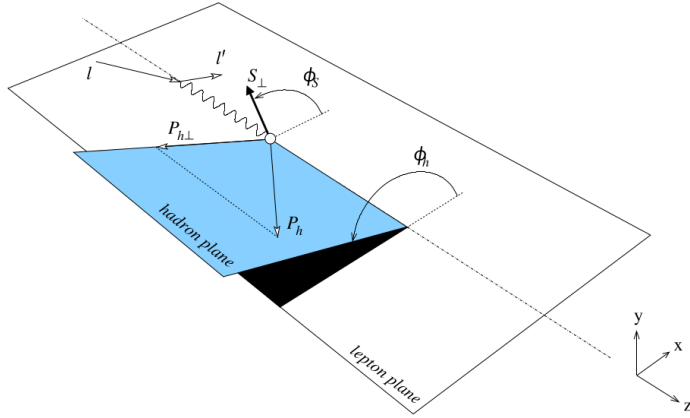


Figure 1.8: Definition of azimuthal angles for SIDIS

1.3 Polarized Semi-Inclusive Deep Inelastic Scattering

The polarized SIDIS ~~on which~~ a polarized lepton ℓ hits a polarized nucleon target N and produces a final state including the scattered lepton and at least one measured hadron h

$$\ell(l) + N(P) \rightarrow \ell(l') + h(P_h) + X \quad (1.9)$$

where the quantities in parentheses represent the four-momenta. The kinematic of the reaction is described in figure 1.8. In the limit of $Q \ll m_{W,Z}$ the interaction can be described as a single photon exchange, then the

cross-section can be expressed [2] as:

$$\begin{aligned}
& \frac{d\sigma}{dx_B dy d\psi dz d\phi_h dP_{h\perp}^2} = \\
& \frac{\alpha^2}{x y Q^2} \frac{y^2}{2(1-\varepsilon)} \left(1 + \frac{\gamma^2}{2x_B}\right) \left\{ F_{UU,T} + \varepsilon F_{UU,L} + \sqrt{2\varepsilon(1+\varepsilon)} \cos\phi_h F_{UU}^{\cos\phi_h} + \right. \\
& + \varepsilon \cos(2\phi_h) F_{UU}^{\cos 2\phi_h} + \lambda_e \sqrt{2\varepsilon(1-\varepsilon)} \sin\phi_h F_{LU}^{\sin\phi_h} + \\
& + S_{\parallel} \left[\sqrt{2\varepsilon(1+\varepsilon)} \sin\phi_h F_{UL}^{\sin\phi_h} + \varepsilon \sin 2\phi_h F_{UL}^{\sin\phi_h} \right] + \\
& + S_{\parallel} \lambda_e \left[\sqrt{1-\varepsilon^2} F_{LL} + \sqrt{2\varepsilon(1-\varepsilon)} \cos\phi_h F_{LL}^{\cos\phi_h} \right] + \\
& + |\mathbf{S}_{\perp}| \left[\sin(\phi_h - \phi_S) \left(F_{UT,T}^{\sin(\phi_h - \phi_S)} + \varepsilon F_{UT,L}^{\sin\phi_h - \phi_S} \right) + \right. \\
& + \varepsilon \sin(\phi_h + \phi_S) F_{UT}^{\sin(\phi_h + \phi_S)} + \varepsilon \sin(3\phi_h - \phi_S) F_{UT}^{\sin(3\phi_h - \phi_S)} \\
& + \left. \sqrt{2\varepsilon(1+\varepsilon)} \sin\phi_S F_{UT}^{\sin\phi_S} + \sqrt{2\varepsilon(1+\varepsilon)} \sin 2\phi_h - \phi_S F_{UT}^{\sin(2\phi_h - \phi_S)} F_{UT}^{\sin(2\phi_h - \phi_S)} \right] + \\
& + |\mathbf{S}_{\perp}| \lambda_e \left[\sqrt{1-\varepsilon^2} \cos(\phi_h - \phi_S) F_{LT}^{\cos(\phi_h - \phi_S)} + \sqrt{2\varepsilon(1-\varepsilon)} \cos\phi_S F_{LT}^{\cos\phi_S} + \right. \\
& \left. \left. \sqrt{2\varepsilon(1-\varepsilon)} \cos(2\phi_h - \phi_S) F_{LT}^{\cos(2\phi_h - \phi_S)} \right] \right\} \quad (1.10)
\end{aligned}$$

where α is the fine structure constant, and the $F_{XY,Z}^{weight}$ are the structure functions connecting the cross-section with the TMDs. The apex *weight* represents the modulation associated with each structure function, which depends on the angle between the hadron and lepton plane ϕ_h , and the angle between the lepton plane and the transverse component of the target spin ϕ_S . The first and second subscripts on the structure functions indicate the polarization *Longitudinal*, *Transverse*, or *Unpolarized* of the beam and the target. The third subscript, if present, indicates the polarization of the virtual photon, and the ε is the ratio between the longitudinal and transverse photon flux

$$\varepsilon = \frac{1 - y - \frac{\gamma^2 y^2}{4}}{1 - y + \frac{y^2}{2} + \frac{\gamma^2 y^2}{4}} \quad (1.11)$$

where y is the usual variable of the DIS

$$y = \frac{P \cdot q}{P \cdot l} \quad (1.12)$$

where P is the 4-momentum of the target nucleon, q the virtual photon one, and l the beam lepton one. The structure functions F_{XY}^{weight} can be expressed in the form of a combination of TMDs, and then their measurements will provide information about the nucleon structure. They are implicitly dependent on

the transferred momentum Q^2 , the Bjorken variable x_B , the transverse momentum of the hadron p_T , and the ratio between the hadron energy and the virtual photon energy z . Their definitions are recalled here, because these quantities will be used often in the following:

$$Q = \sqrt{(l' - l)^2} \quad (1.13)$$

$$x_B = \frac{Q^2}{2P \cdot q} \quad (1.14)$$

$$p_T = p_H - \left(\frac{p_H \cdot p_\gamma}{|p_\gamma|} \right) \quad (1.15)$$

$$z = \frac{P \cdot p_H}{P \cdot q} \quad (1.16)$$

The structure functions are the ~~Fourier terms~~ associated with spin asymmetries, which means there is an asymmetry depending on the angle ϕ_h and ϕ_s between the number of events obtained with different polarizations.

1.4 Beam-Spin Asymmetry

A possibility is to measure the Beam-Spin Asymmetry (BSA), the asymmetry related to the longitudinal polarization of the beam, will be used as a case study. The BSA can be expressed as

$$A_{LU} = \frac{d\sigma^+ - d\sigma^-}{d\sigma^+ + d\sigma^-} = \frac{A_{LU}^{\sin \phi} \sin \phi}{1 + A_{UU}^{\cos \phi} \cos \phi + A_{UU}^{\cos 2\phi} \cos 2\phi} \quad (1.17)$$

where $d\sigma^\pm$ is the differential cross-section for each beam helicity state (parallel or antiparallel), and $A_{LU}^{\sin \phi}$, $A_{UU}^{\cos \phi}$, $A_{UU}^{\cos 2\phi}$ are the asymmetry terms, which are related to the structure functions. From the measurement of $A_{LU}^{\sin \phi}$ it is possible to obtain the correspondent ~~term of the cross section~~ via

$$A_{LU}^{\sin \phi} = \frac{\sqrt{2\varepsilon(1-\varepsilon)} F_{LU}^{\sin \phi}}{F_{UU}} \quad (1.18)$$

where $F_{UU} = F_{UU,T} + \varepsilon F_{UU,L}$ and ε is defined in Equation 1.11. ~~The~~ structure functions are usually ~~expressed~~ as a ratio with the unpolarized one.

Experimentally, the BSA is defined as

$$A_{LU}(\phi) = \frac{1}{P_b} \frac{N^+ - N^-}{N^+ + N^-} \quad (1.19)$$

where P_b is the beam polarization and N^\pm the number of events with ~~beam helicity positive or negative~~.

The cross-section term $F_{LU}^{\sin\phi}$ is related to the TMDs by the following expression

$$F_{LU}^{\sin\phi} = \frac{2M}{Q} \mathcal{C} \left[\frac{\hat{\mathbf{h}} \cdot \mathbf{k}_T}{M_H} \left(x_B e H_1^\perp + \frac{M_h}{M} f_1 \frac{\tilde{G}^\perp}{z} \right) + \frac{\hat{\mathbf{h}} \cdot \mathbf{p}_T}{M} \left(x_B g^\perp D_1 + \frac{M_h}{M} h_1^\perp \frac{\tilde{E}}{z} \right) \right] \quad (1.20)$$

where M is the mass of the target, M_h the mass of the hadron, Q^2 the transferred momentum, \mathbf{p}_T is the intrinsic quark transverse momentum in the generic distribution function f_1 , \mathbf{k}_T is the intrinsic quark transverse momentum in the generic fragmentation function D_1 , and $\hat{\mathbf{h}}$ is the unitary vector in the direction of the hadron's transverse momentum. Furthermore, \mathcal{C} indicates a convolution of TMDs, e is a twist-3⁷ TMD, H_1^\perp is the Collins Fragmentation Function (FF), \tilde{G}^\perp is a twist-3 FF, g^\perp is a twist-3 T-odd distribution function, h_1^\perp is the Boer-Mulders function, and \tilde{E} is a twist-3 FF.

Nowadays, data from HERMES, COMPASS⁸, and Jefferson Lab (JLab) experiments⁹ provided the first ~~measurements and their consequences, that were mentioned previously.~~ Reference [5] contains a recap of the most recent results in polarized SIDIS. Recently, the CLAS collaboration, which runs the CLAS12 spectrometer at JLab, released a first high-precision measurement of polarized SIDIS for π^\pm , but an equivalent result for the kaon is still missed. The improvement on the Particle Identification (PID) performance generated by the installation of the Ring Imaging Cherenkov (RICH) in 2018 will ~~permit achieving this measurement. In the next decades, the new breakthrough measurement will probably come from the Electron-Ion Collider (EIC), the new large-scale collider for three-dimensional nucleon imaging.~~

⁷The twist describes the scaling behavior with respect to the transferred momentum. Generally, in QCD, the leading twist is the twist-2.

⁸COMPASS is a fixed-target experiment in the CERN north area. It acquired data from 2001.

⁹Jefferson Lab is a U.S. Department of Energy Office of Science Laboratory. It hosts a 12 GeV beam of polarized electrons and four experimental halls. In particular, Hall A and CLAS collaboration are involved in studying the hadronic structure via SIDIS.

Chapter 2

The Ring Imaging Cherenkov detector for CLAS12

To perform QCD measurement with flavor sensitivity, an efficient system to identify the hadrons in the final state is fundamental. This Chapter introduces the CLAS12 spectrometer focusing on the PID system and describes the Ring Imaging Cherenkov (RICH) detector. Particularly, the author was involved in the assembly and commissioning of the second module, in the efficiency study of the first module, and in the first physics analysis carried out using the RICH data. The first two of these activities are described in this Chapter.

2.1 The CLAS12 spectrometer at Jefferson Lab

The Thomas Jefferson National Accelerator Facility (JLab) is one of the most important laboratories dedicated to nuclear physics research that is carried out using the electron beam provided by the Continuous Electron Beams Accelerator Facility (CEBAF) and different apparatuses realized in four experimental halls. The JLab site is shown in Figure 2.1. The high intensity, highly polarized, 12 GeV electron beam permits to perform sophisticated measurements aiming to probe and possibly extend the Standard Model of particle physics via precise parity violation measurement, light dark matter searches, and exotic particle discovery, exploiting the peculiarities of the four halls. A scheme of CEBAF is represented in Figure 2.2.

The experimental Hall B hosts the CEBAF Large Acceptance Spectrometer for operation at 12 GeV (CLAS12)[6], a spectrometer developed by an international collaboration of 48 institutions. CLAS12 is based on a dual-magnet system, constituted by a torus magnet and a solenoid magnet, and it is designed to provide efficient detection of charged and neutral particles over a large fraction of the solid angle. The main tasks of the CLAS12 physics program are:

- Nucleon structure studies using exclusive and semi-inclusive deep in-

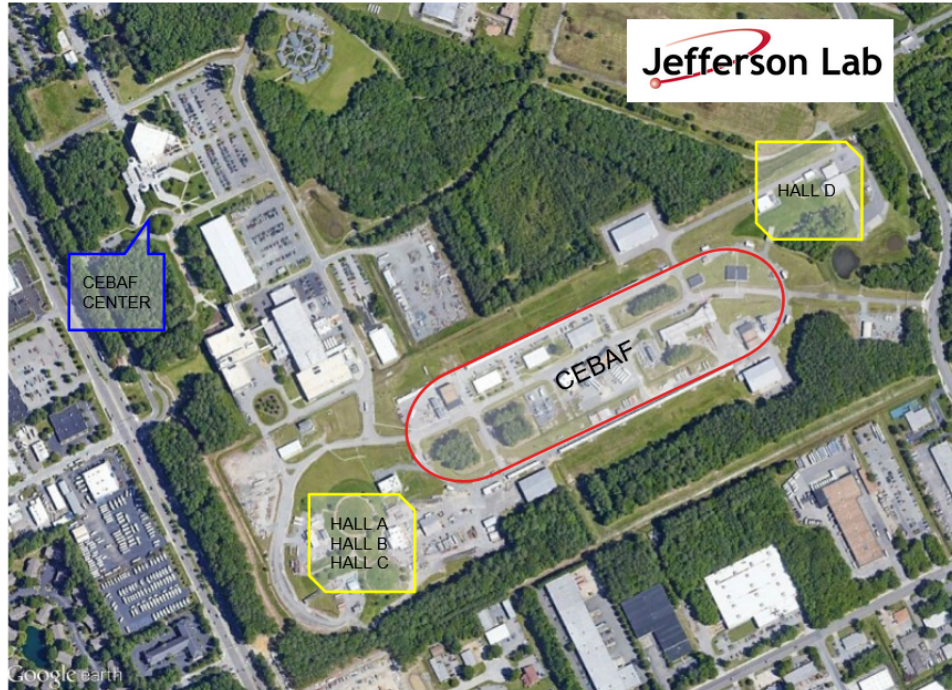


Figure 2.1: The JLab site



Figure 2.2: The CEBAF and experimental halls scheme

elastic scattering processes by mapping the Generalized Parton Distributions (GPDs)¹ and Transverse-Momentum-Dependent distributions (TMDs);

- Precision measurement of structure functions and forward parton distribution at high x_B ;
- Elastic and transition form factors at high momentum;
- Hadronization and color transparency;
- Hadron spectroscopy, studying heavy baryons and mesons with ordinary and exotic quantum numbers.

The magnets

The solenoid (Figure 2.3a) is made by self-shielded superconducting coils surrounding the beamline and used to generate a magnetic field primary in the beam direction. This design allows us to achieve the physics requirements of shielding the Moeller electron background, tracking particles with large angles, and providing a uniform field in the center to operate dynamically polarized proton and deuteron targets. The solenoid generates a 5 T field at its center at the maximum current.

The torus (Figure 2.3b) magnet comprises six identical superconducting coils, symmetrically arranged to obtain a toroidal field around the beamline. The geometrical coverage seen from the target is between 5° and 40° . The peak field is 3.58 T, while the field is zero at the center for reasons of symmetry.

2.1.1 The detector

CLAS12 can be divided into the Central Detector (CD) and the Forward Detector (FD).

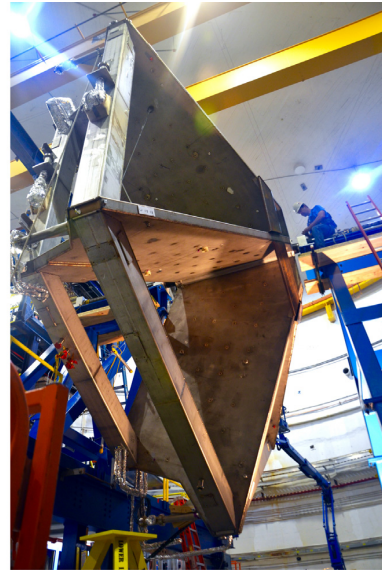
The Central Detector

The CD is designed to detect particles covering the polar angle between 35° and 125° and almost the whole azimuthal angle. The CD is placed inside the solenoid magnet. The tracking and the measure of the momentum are provided by the Central Vertex Tracker (CVT), while the charged particle identification is entrusted to the Central Time-Of-Flight (CTOF). Moreover, the CD includes two neutron detectors, the Central Neutron Detector (CND) and the Back Angle Neutron Detector (BAND). These detect neutrons with momentum up to 1.25 GeV and polar angle up to 175° .

¹GPDs are a different way of accessing the nucleon structure. They are like tomographic slices of the form factors at a fixed value of the momentum fraction x_B



(a) CLAS12 solenoid



(b) CLAS12 torus

Figure 2.3: The CLAS12 superconducting magnets.

The Forward Detector

The Forward Detector (FD) covers polar angles between 5° and 35° , with tracking, particle identification, and momentum measurement provided by different detectors. The FD structure is based on the torus magnet, so it is divided into six sectors that are identical in dimensions and almost identical in composition. All the sectors include three regions of Drift Chamber (DC) for tracking and two calorimeters, the Electromagnetic Calorimeter (EC) and Pre-shower Calorimeter (PCAL) for identification and kinematical reconstruction of electrons, photons, and neutrons. The only differences between sectors regard the Particle Identification (PID) components. Indeed, all six are equipped with a High Threshold Cherenkov Counter (HTCC) and a Forward Time-Of-Flight (FTOF), four sectors host a Low Threshold Cherenkov Counter (LTCC), and the other two a Ring Imaging Cherenkov (RICH) detector; more details about the PID are discussed in the following. Moreover, the FD includes the Forward Tagger (FT) to extend the capability of detecting electrons and photons at very forward polar angles between 2.5° and 4.5° , consisting of a calorimeter, a hodoscope, and a micro-strip gas tracker.

The FD Particle Identification

The PID plays a crucial role in QCD studies with flavor sensitivity, particularly the capability to distinguish charged hadrons and leptons. Indeed,

aiming to perform SIDIS measurements, the precise identification of the final states acquires great importance. The following detectors concur in the PID:

- The Forward Time-Of-Flight (FTOF) measures the time-of-flight of charged particles from the production target. The system is designed to reach an average time resolution of 80 ps to distinguish pions and kaons up to 3 GeV.
- The Low Threshold Cherenkov Counter (LTCC) is a Cherenkov counter that uses C₄F₁₀ as a radiator; it allows the tag of the charged pions up to 3.5 GeV.
- The High Threshold Cherenkov Counter (HTCC) separates the electrons and positrons with momenta below 4.9 GeV from charged hadrons. It operates in dry CO₂ gas at 1 atm pressure.
- Two Ring Imaging Cherenkov (RICH) detectors were added (the first in 2018 and the second in 2022) in two opposite sectors to improve the identification of charged kaons in higher momentum range inaccessible with the FTOF and LTCC. They are based on the measurement of the Cherenkov angle of the photons emitted by the charged particle passing through an aerogel radiator, which, combined with the kinematic information, allows the separation of the hadron species.

A scheme of the RICH and LTCC positions is shown in Figure 2.4. The author was directly involved in the assembly of the second module of the RICH, in the efficiency studies of the first module, and in the first analysis of SIDIS based on the RICH to identify the kaons.

2.2 The CLAS12 Ring Imaging Cherenkov

In 2018, a first Ring Imaging Cherenkov (RICH) detector [7] was incorporated into the CLAS12 spectrometer at JLab. A RICH exploits the Cherenkov photons produced by a charged particle crossing a radiator with a speed greater than the speed of light in that medium to identify the velocity of the particle. This information, combined with the momentum measured by other detectors, allows to identify the mass of the particle. The Cherenkov effect is described by

$$\cos \theta_{Ch} = \frac{1}{\beta n(\lambda)} \quad (2.1)$$

where θ_{Ch} is the opening angle of the photon from the particle trajectory, β is the particle's speed, and $n(\lambda)$ is the refractive index of the medium depending on the wavelength. After a gap region, the projection of the Cherenkov cone is the so-called “ring”, which has to be detected by light detectors operating in single-photon mode. A generic RICH functioning scheme is shown in

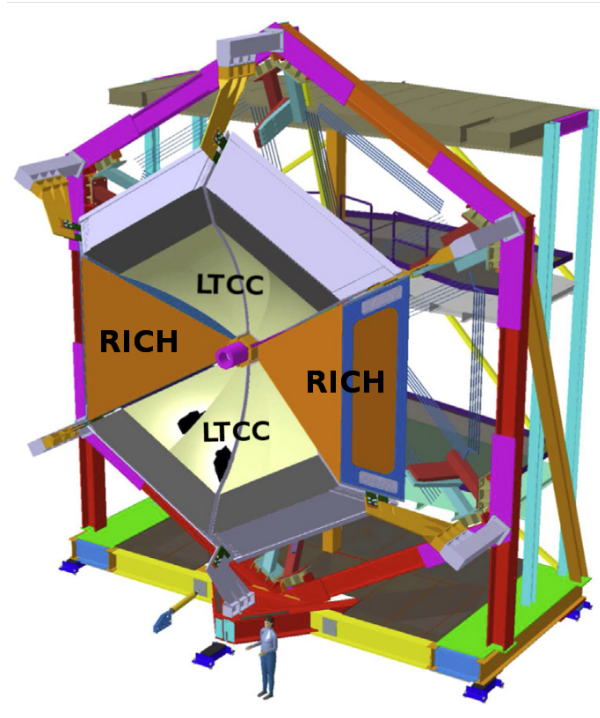


Figure 2.4: Scheme of the RICH and LTCC detectors position in CLAS12.

Figure 2.5a. The CLAS12 RICH was explicitly designed to facilitate efficient kaon identification in the momentum range between 3 GeV/c and 8 GeV/c. Indeed, the original PID system based on FTOF, LTCC, and HTCC does not provide sufficient separation in this momentum range between kaons, pions, and protons for effective SIDIS studies on kaons. In 2022, a second module was installed, identical to the first. Figure 2.15b shows CLAS12 with the two RICH modules.

2.2.1 RICH design

According to the CLAS12 Monte Carlo studies, the kaons identification needs to achieve a rejection factor for pions in the order of 1 : 500, corresponding to a separation of 4σ between pions and kaons. As shown in Figure 2.6, the only possible radiator is the silica aerogel, which has a very low macroscopic density and a refractive index between the gas and the liquids. The RICH has to match inside the Forward Carriage of CLAS12, which imposes several constraints: a projective geometry, a limited depth of 1.2 m, and $\sim 4.5 \text{ m}^2$ entrance windows. Based on the simulation, the RICH is designed to integrate the aerogel radiators, visible light photon detectors, and a focusing mirror system in a compact hybrid-optics design. The mirrors allow the reduction of the photon detector area to $\sim 1 \text{ m}^2$, minimizing the cost and the impact on the

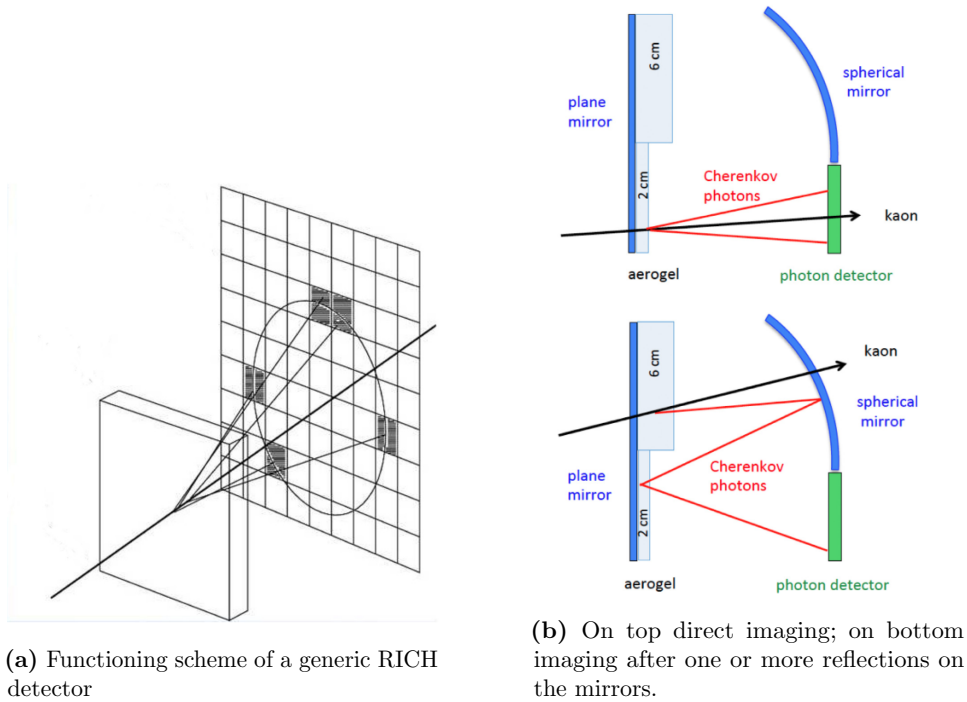


Figure 2.5

downstream detectors. Depending on the polar angle of the incident particles, the photons can hit the photo-detection area directly, as shown in Figure 2.5b. To minimize the total material budget, the mechanical structure is made almost entirely of light materials, particularly carbon fiber. A complete detector scheme is shown in Figure 2.7.

2.2.2 The radiator

The radiator selected for the RICH was the silica aerogel, the only possible choice, as shown from the plot in Figure 2.6, where the expected Cherenkov angle for different hadrons is plotted as a function of the particle momentum. The aerogel is an amorphous solid network of SiO_2 nanosphere, and it has a very low macroscopic density and a refractive index intermediate between gas and liquid radiators. The aerogel was produced by Budker and the Boreskov Institute of Nuclear Physics (Russia), which made all the 102 tiles of different shapes and thicknesses needed for each detector module. The tiles were assembled into two sections. The first, made of one layer of 2-cm-thick tiles, covers the region between the beam pipe up to the polar angle of 17.5° . The second region covers the polar angle between 17.5° and 26° and is made of two layers of 3-cm-thick tiles. Most tiles are squared $20 \times 20 \text{ cm}^2$ bricks, but triangular, trapezoidal, and pentagonal shapes became necessary on the edges

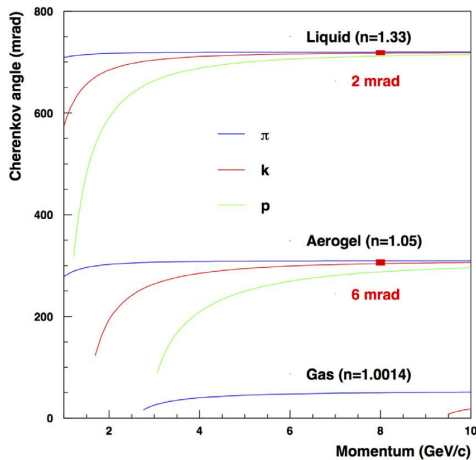


Figure 2.6: Expected Cherenkov angle for different hadron as a function of momentum for different radiators.

to cover the entire entrance window. Each tile was tested [3] to determine the side length, thickness, and surface planarity. Also, the optical parameters were measured, particularly the refractive index at the reference wavelength of 400 nm and the light transmission as a function of the wavelength. Using the Hunt parametrization [1], the parameters of transparency A_0 , clarity C , and scattering length at 400 nm Λ_S were extracted. From these measurements, the expected mean photon yield is 19 photoelectrons (p.e.) for the 2-cm-thick layer and 25 p.e. for the 6-cm-thick layer.

2.2.3 The mirror system

According to the simulation, the mirror system was designed to minimize the loss of photons and direct most of them to the photon detector. A drawing of the entire mirror system is shown in Figure 2.8.

The spherical mirror

It comprises ten sub-mirrors produced by the *Composite Mirror Applications* company [19]. It covers a total surface of 3.6 m^2 and has a curvature radius of 2.7 m. This mirror is placed in front of the entrance window to collect the photons produced by particles entering with the larger polar angle. The accuracy of each sub-mirror spherical surface was quantified via the spot size measurement, illuminating the mirror with a point-like source and observing the size of the reflected spot with a CCD camera in its center. The size spot is quantified by D_0 , the minimum diameter containing 90% of the reflected light, which is related to the angular resolution by

$$\sigma_\theta = \frac{D_0}{8R} \quad (2.2)$$

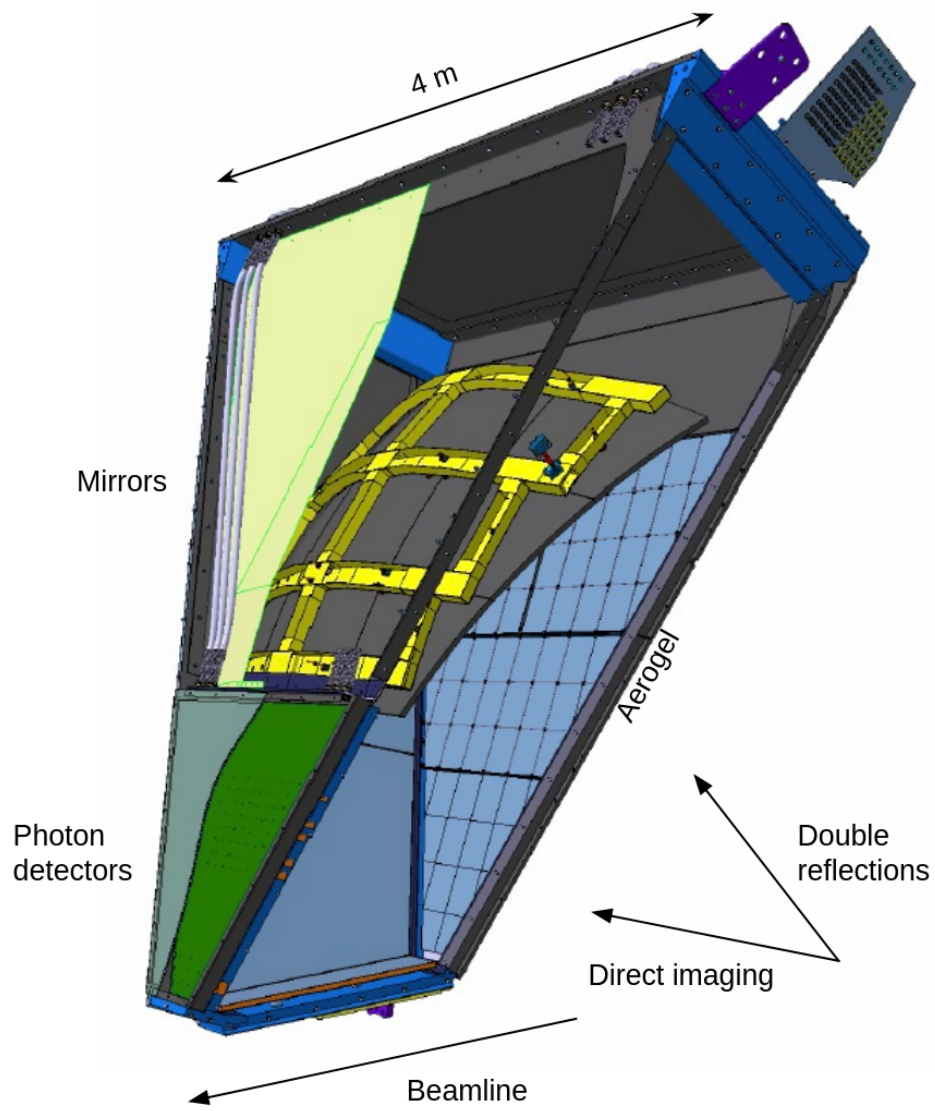


Figure 2.7: Sketch of the full RICH: the aerogel tiles, the structure supporting the spherical mirrors, and the photo-detection plane are indicated.

where R is the curvature radius. The mirror mechanical substrate is made by a sandwich of two carbon fiber layers with a honeycomb core that achieves a high rigidity and a low material budget of $0.01X_0$. The mirrors were coated with a reflective SiO_2 layer by the *Evaporated Coating* company [20]. The reflectivity of the mirrors is measured to be between 88% and 90% in the 300 – 700 nm wavelength range of interest.

The planar mirrors

There are seven planar mirrors, two placed on each side of the detector, one on the bottom, and two on the front panel supporting the aerogel, covering a total surface of 6.5 m^2 . They were produced by the *Media Lario* company [21], which is used to work for terrestrial telescope applications. The mirrors are made of two skins of glass glued on an aluminum honeycomb core; the front mirror skins are 0.7 mm thick to reduce the mirror material budget to $\sim 0.01X_0$ in the detector acceptance, and the other mirror skins are 1.6 mm thick. The reflectivity of the planar mirrors has been measured to be greater than 90% in the 300 – 700 nm range of wavelength and shows a maximum of about 95% at 400 nm.

2.2.4 The photon detector

The mirrors made it possible to reduce the photo-detection area to $\sim 1 \text{ m}^2$, in the region close to the beamline where most of the particles are produced and carrying the most demanding high momenta.

The photo-sensor

To make imaging possible, the photo-sensor has to work efficiently in the Single PhotoElectron (SPE) regime and be sensitive to visible light (to match the aerogel emission spectrum). Moreover, it must have the spatial resolution required to achieve the designed angular resolution, provide an active area with minimal dead space, and be insensitive to the low torus fringe field where the RICH readout is located (estimated to be no more than 3.5 G). The Hamamatsu flat-panel Multi-Anode Photo-Multiplier (MAPMT) H8500, an 8×8 array of $6 \times 6 \text{ mm}^2$ pixels covering a $5 \times 5 \text{ cm}^2$ area, was initially selected as photo-sensor. However, it was not optimal for the SPE regime. Just after the start of the build of the first module of the RICH, Hamamatsu released the H12700 MAPMT, which has the same layout and an optimized dynode structure for the SPE. The first RICH combines 80 H8500 and 311 H12700 for 391 photo-sensors, while the second module is fully equipped with H12700. This configuration results in 25024 pixels covering the $\sim 1 \text{ m}^2$ trapezoidal active area of each RICH module. Figure 2.9a, shows a view of the MAPMTs side of the electronic panel.

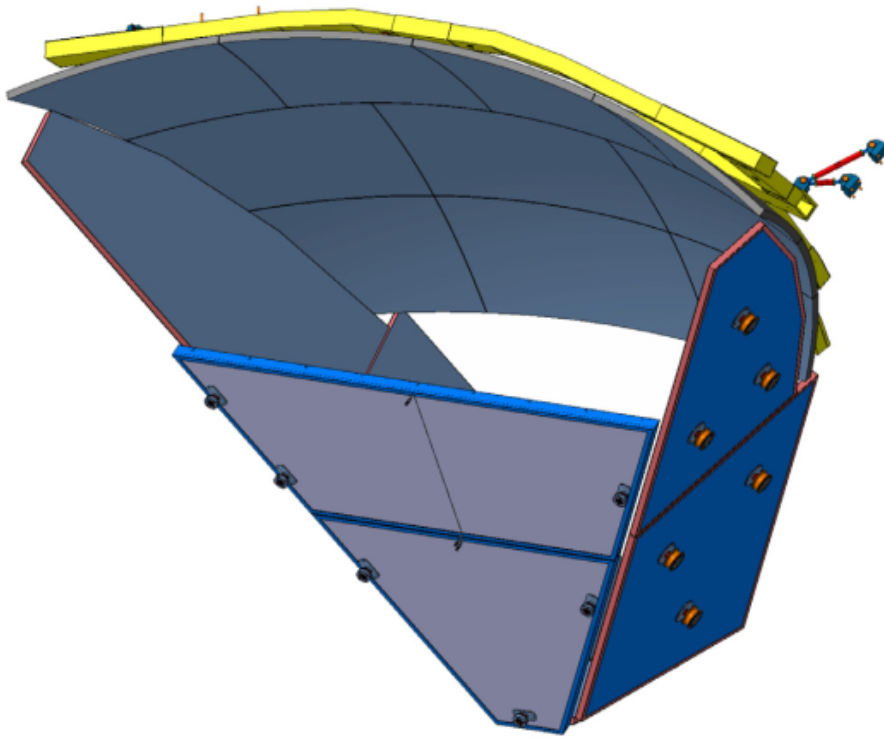


Figure 2.8: RICH mirror system draw. The spherical mirror has ten different spherical mirrors reflecting the light backward. Two mirrors upstream on the aerogel reflect the photons a second time in the direction of the MAPMTs, as shown in figure 2.5b. To minimize the photon loss, two planar mirrors on each side and one on the bottom surround the rest of the RICH module.

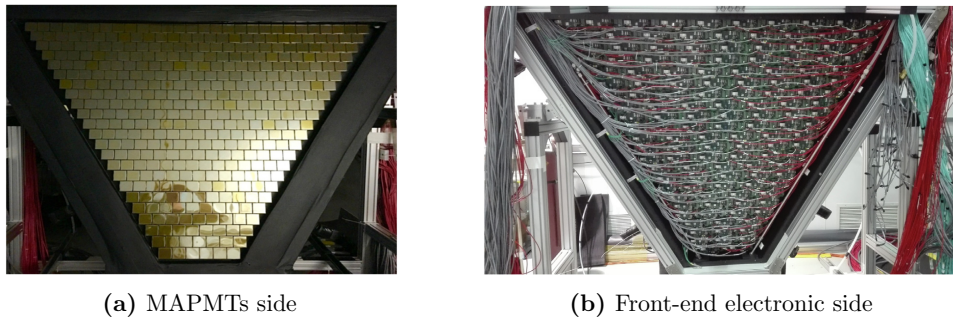


Figure 2.9: The RICH electronic panel.

The readout electronics

The front-end electronics is organized in compact modules called tiles serving two or three MAPMTs. The tile scheme is shown in Figure 2.10. The front-end electronics is intended to ensure a 100% efficiency at $\frac{1}{3}$ of the average photoelectron signal level, 1 to 4 gain spread compensation, and time resolution of the order of 1 ns to distinguish direct from reflected hits. Additionally, it has to sustain a 20 kHz trigger rate with 8 μ s latency and negligible dead time. Three different boards make each readout unit:

- The adapter board provides the electrical connectivity of the sensors with the readout, preserving the light and gas tightness when the electronic panel is mounted in the detector. It also distributes the power to the MAPMTs, nominally -1000 V.
- The ASIC board mounts two or three Multi-Anode ReadOut Chip (MAROC) chips, a 64-channel microcircuit dedicated to processing MAPMTs signal.
- The FPGA board hosts a Xilinx7 FPGA chip responsible for configuring and reading the MAROC chips, distributing the trigger, and interfacing with the DAQ system.

To complete the readout system, three kinds of cable have been connected to each tile: the low-voltage cables to power the FPGA, the high-voltage cable to power the MAPMTs, and the optical fiber for the communication between the FPGA and the DAQ system. The last step to complete the electronic panel was to add a grounding grid, which attenuates the electronic noise, and the cooling system, based on a flow of compressed dry air that allows to maintain the temperature of the FPGA below the critical temperature of 75°C . A picture of the full readout electronics of the RICH is reported in Figure 2.9b.

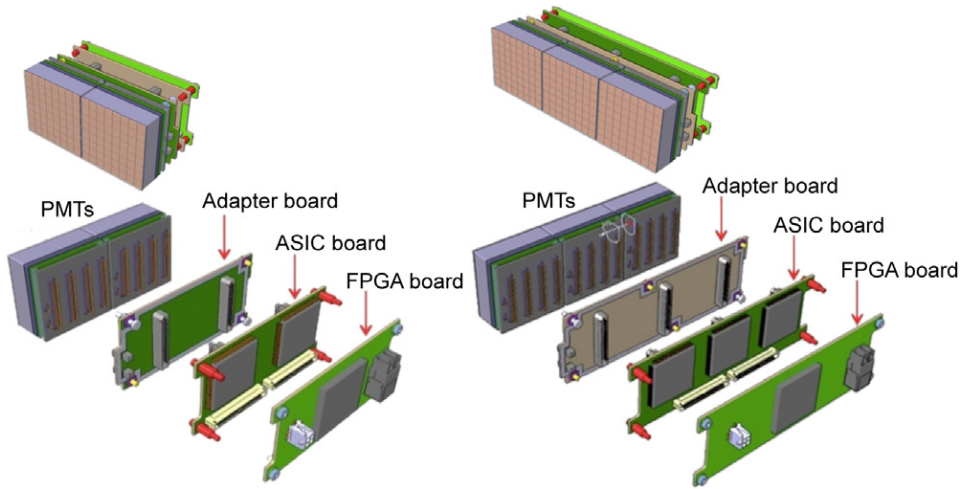
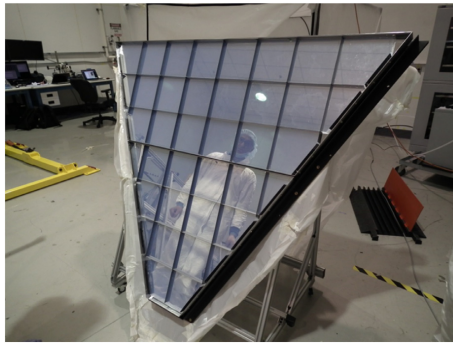


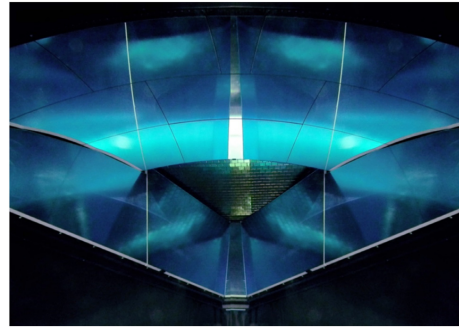
Figure 2.10: Scheme of the front-end electronic tiles serving two (left) or three (right) MAPMTs.

2.3 The assembly and commissioning of the second module of the RICH

In the spring of 2022, the author was directly involved in assembling the second module of the RICH, particularly concerning the electronic panel mounting and the installation of the detector inside the CLAS12 experiment. The assembling process before the installation was performed inside a clean room at JLab, and each subsystem was installed in the detector structure after the completion of the relative characterization tests. The expert of mechanics from INFN Frascati took care of the assembly of the RICH vessel (see Figure 2.12a), which has to sustain the entire detector structure. The spherical mirrors were characterized and then placed in their sustain structure inside the vessel, while the planar mirrors were directly placed on the vessel's walls (Figure 2.12d). The characterization includes measurements of the reflectivity in several points and of the light spot size. The spherical sub-mirrors were aligned using a point-like source and converging the reflected spot on the same point (Figure 2.12c). The hydrophobic aerogel was purged with a flux of nitrogen and mounted on the inner side of the frontal panel, in the section with (Figure 2.11a) and without (Figure 2.12b) mirrors. The INFN Ferrara team, including the author, worked mainly on the electronic panel, placing the adapter boards on the inner side and connecting them with the ASIC boards on the other side (Figure 2.12e). Then, they added the FPGA boards to the ASIC boards and cabled all the 138 tiles (Figure 2.12f). After completing this step, the 391 MAPMTs were put in place by members of the Ferrara team, JLab and Duquesne University. All the readout units were connected to the power and DAQ system and tested. Under the



(a) The 2-cm-thick section of the aerogel mounted on the two frontal mirrors.



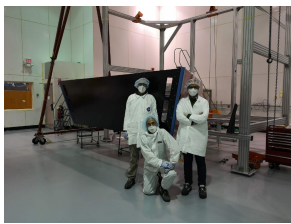
(b) Inside the RICH detector, the mirror system is seen from the entrance panel. From the top, clockwise, there are the ten spherical sub-mirrors, the two right mirrors, the bottom mirror, and the two left mirrors. At the center, the MAPMTs are visible.

Figure 2.11

supervision of the Frascati and Ferrara experts, the electronic panel was placed in the RICH vessel and tested again to ensure all the readout units worked correctly.

The last step was placing the frontal panel with the aerogel into the detector; the picture in Figure 2.11b was taken during this operation. This operation was particularly critical since the aerogel was resting on its supports. A CCD camera and a small portable light were placed inside the detector to check if any problem occurred during the moving phase. The completed RICH was tested for light leaks, which can cause problems for the SPE, and gas leaks because the inner humidity needs to be minimized to maintain the aerogel properties. At the beginning of June 2022, the RICH was moved into Hall B (Figure 2.13), about 1 km from the clean room, using a truck with a special trolley. The assembly and transportation were made with the detector in a horizontal position; in Hall B, it was rotated to orient it vertically, placing the short side on the bottom and the large on top. Then, it was rotated along the axis which passes through the detector to place it in the final configuration of having the short side on the right, close to the beamline, and the large side on the left. Finally, the RICH was raised to take its place inside the CLAS12 spectrometer. Since the moving phase was another critical step in the installation, the internal CCD camera was used to check again that no problem occurred to the aerogel. Figure 2.14 shows a picture taken inside the RICH after the installation.

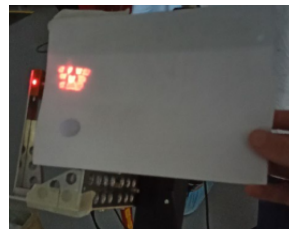
Finally, the author was directly involved in cabling the RICH to the infrastructure of the CLAS12 experiment (Figure 2.15a). The picture of the complete array of RICH and LTCC modules of CLAS12 after the second



(a) RICH vessel



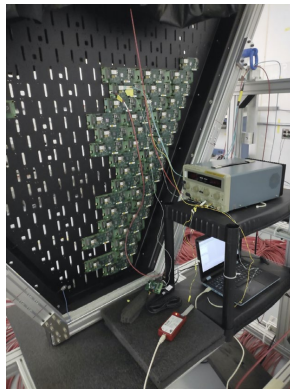
(b) Aerogel preparation



(c) Spherical mirror alignment



(d) Latera mirror assembly

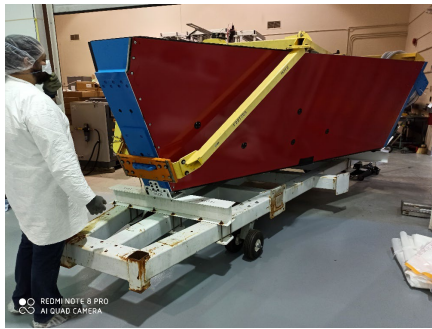


(e) Electronic Panel assembly and testing



(f) Electronic Panel cabling

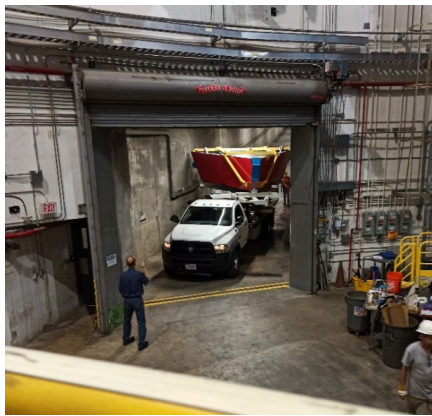
Figure 2.12



(a)



(b)



(c)



(d)

Figure 2.13: Moving of the RICH from the clean room to Hall B.



Figure 2.14: View of the aerogel inside the RICH after placing it in Hall B.

RICH module installation is reported in Figure 2.15b. The RICH was included in the CLAS12 DAQ chain, and all the calibration and control procedures were extended from the first module. The first signals from the two modules are reported in Figures 2.15c and 2.15d.

2.4 RICH efficiency in cleaning the kaon sample

The first aim of the RICH was to enhance the kaon identification and improve the pion rejection, then the first efficiency study was performed to evaluate the percentage of correct identification of pions and the percentage of misidentification of pions as a kaon, which was not negligible phenomenon using the standard PID of CLAS12. This can be carried out by comparing the missing mass of final states like eH^+X selected using the PID of CLAS12 without the RICH or the PID provided by the RICH.

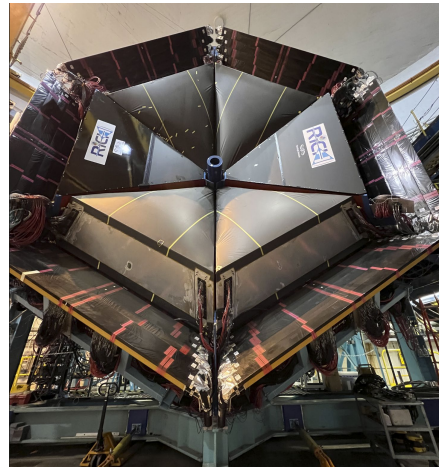
The event selection for this analysis is based on the request that the electron is a trigger particle, its momentum is greater than 1.5 GeV, and both the RICH and CLAS12 identify the hadron. Currently, the range of the hadron polar angle is partially limited because the calibration of part of the spherical sub-mirrors in the reconstruction code has yet to be finalized. The polar angle covers values up to $\sim 15^\circ$, as shown in Figure 2.16.

To evaluate the efficiency, it focuses on the neutron peak of the missing mass at 0.94 GeV. Indeed, the exclusive final state $e\pi^+n$ is allowed, while the eK^+n is forbidden for strangeness conservation. Then, in the missing mass plot of events that include a kaon, the neutron peak should not be present, while it is expected if the selected events include a pion.

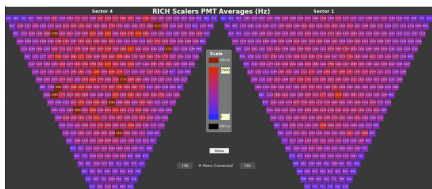
A first qualitative idea of the RICH effectiveness in cleaning the kaon sample can be the plots in Figure 2.17 and Figure 2.18, showing the missing mass of $e\pi^+X$ and eK^+X selected using the CLAS12 or the RICH PID. It is possible to see the neutron peak being present on the plot eK^+X using the CLAS12 PID, while it is strongly reduced using the RICH PID. In the



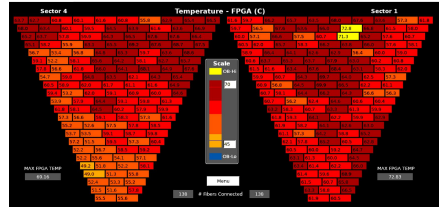
(a) Cabling the RICH



(b) Section of CLAS12 after installing the two modules of the Ring Imaging Cherenkov detector.



(c) First scalers of the two modules.



(d) First temperatures of the two modules.

Figure 2.15

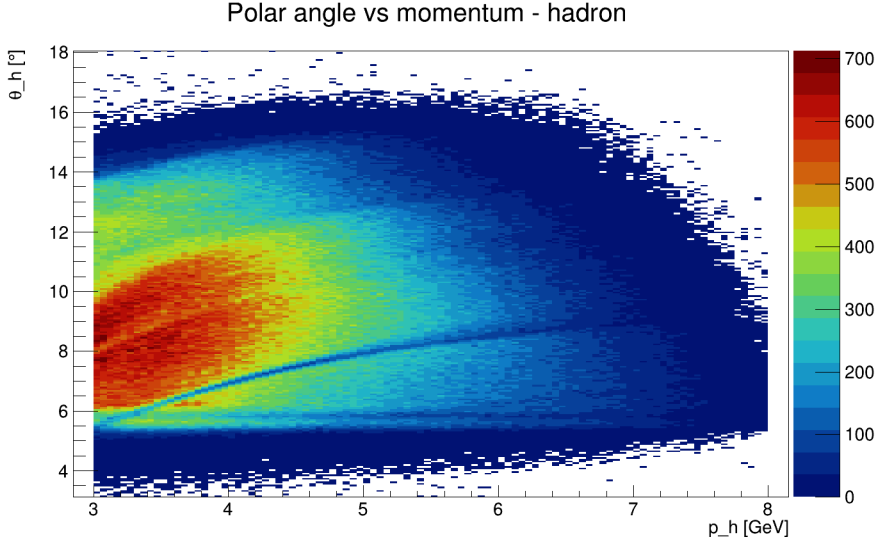


Figure 2.16: Polar angle and momentum of the hadron used for the efficiency study.

$e\pi^+X$ plot, the number of events is larger if using the RICH instead of the CLAS12 PID: this is because a part of the hadrons recognized by CLAS12 as kaons are actually pions, and the RICH correctly identified them. For the same reason, the statistic of the sample selected by the RICH in the missing mass plot of eK^+X is lower than that of the sample identified by CLAS12.

For a quantitative evaluation of the efficiency, it was decided to extract the number of neutrons associated with the peak at 0.94 GeV and to define the pion identification efficiency ($\eta_{\pi \rightarrow \pi}$) as

$$\eta_{\pi \rightarrow \pi} = \frac{\text{Number of exclusive neutrons in } e\pi^+X \text{ events}}{\text{Number of exclusive neutrons in } (e\pi^+X + eK^+X) \text{ events}} \quad (2.3)$$

and the percentage of pion misidentified as kaon ($\eta_{\pi \rightarrow K}$) as

$$\eta_{\pi \rightarrow K} = \frac{\text{Number of exclusive neutrons in } eK^+X \text{ events}}{\text{Number of exclusive neutrons in } (e\pi^+X + eK^+X) \text{ events}} \quad (2.4)$$

that substantially means

$$\eta_{\pi \rightarrow \pi} = 1 - \eta_{\pi \rightarrow K} \quad (2.5)$$

having evaluated that the number of exclusive neutrons in the epX final state is negligible to obtain the accuracy required for this preliminary study.

To estimate the number of neutrons, the missing mass plots were fitted using a Gaussian function for the neutron peak, one or more Gaussian or Breit-Wigner functions for the other peaks, and three different shapes for the

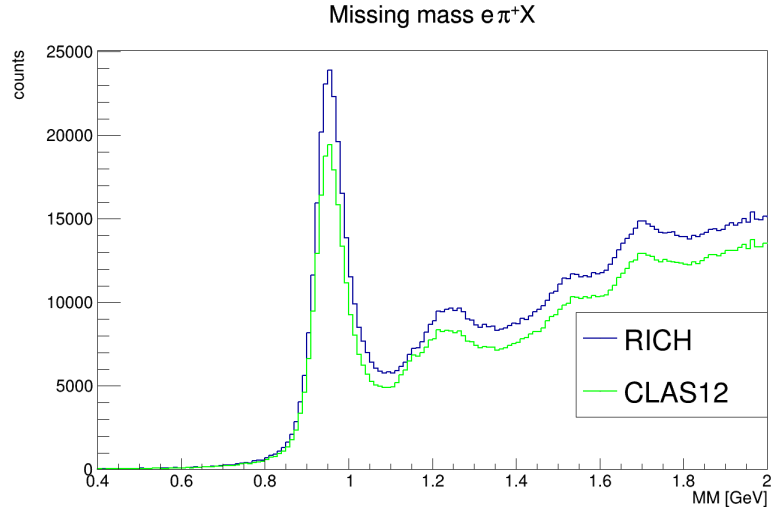


Figure 2.17: Missing mass of final state $e\pi^+X$ for CLAS12 PID (green) and RICH PID (blue). The peak at 0.94 GeV signals the exclusive $e\pi^+n$ final state. The total number of events selected by CLAS12 is less than that selected by RICH because the first misidentified part of the hadrons as if they were kaons.

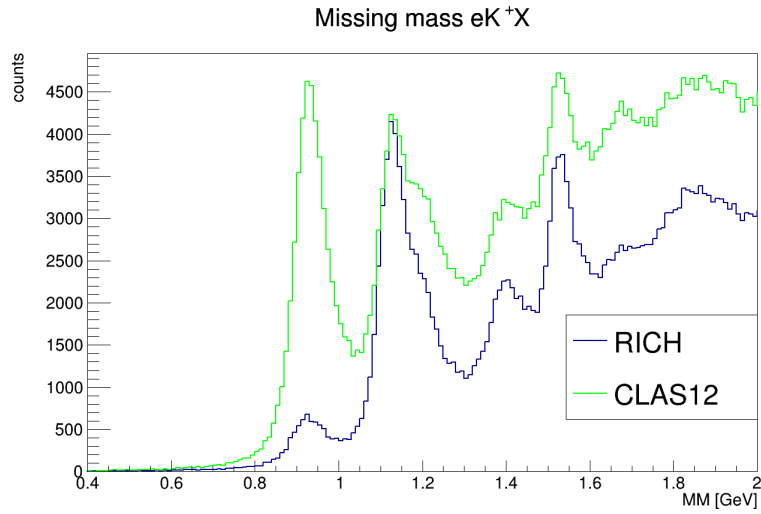


Figure 2.18: Missing mass of final state eK^+X for CLAS12 PID (green) and RICH PID (blue). The clear reduction of the peak at 0.94 GeV using the RICH shows that the number of exclusives state $e\pi^+n$ decreases; this corresponds to a lower number of pions misidentified as kaon, being forbidden the exclusive final state eK^+n . The total number of events selected by CLAS12 is more than that selected by RICH because the first misidentified part of the hadrons as if they were kaons.

SIDIS background distribution: a similar-Weibull function, a second-order Chebyshev polynomial or a crystal-ball distribution.

$$bk g_{Weib}(x; p_0, p_1, p_2) = p_0 x^{p_1-1} \left(-\frac{x}{p_2} \right)^{p_1} \quad (2.6)$$

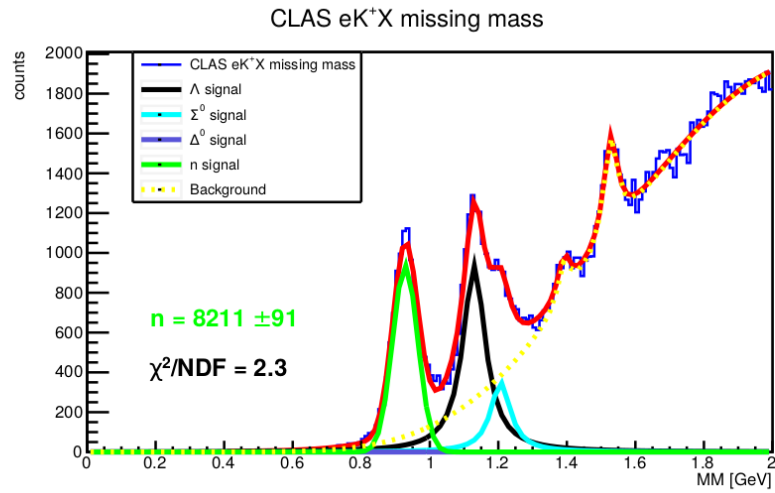
$$bk g_{Cheb}(x; p_0, p_1, p_2) = p_0 + p_1 x + p_2 (2x^2 - 1) \quad (2.7)$$

$$bk g_{Crys}(x; p_0, p_1, p_2, p_3, p_4) = p_0 \cdot \begin{cases} e^{-\frac{1}{2} \left(\frac{x-p_1}{p_2} \right)^2}, & \text{if } \frac{x-p_1}{p_2} > -p_3 \\ \left(\frac{p_4}{|p_3|} \right)^{p_4} \cdot e^{-\frac{|p_3|}{2}}, & \text{if } \frac{x-p_1}{p_2} \leq -p_3 \end{cases} \quad (2.8)$$

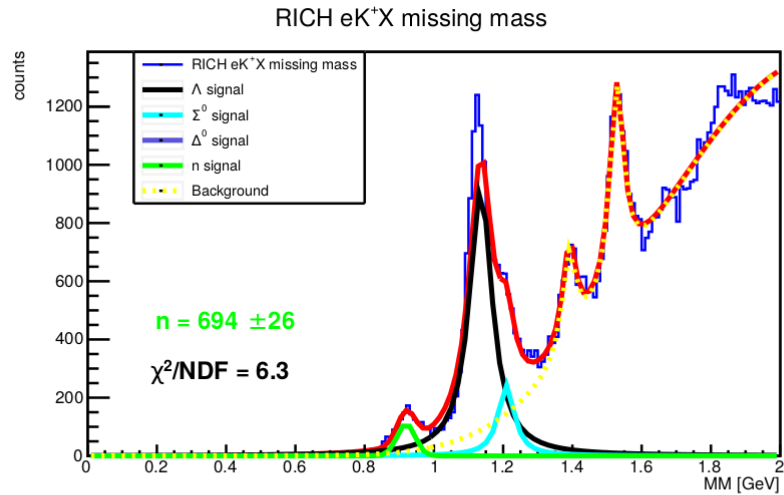
where p_0, p_1, p_2, p_3, p_4 are the parameters of the background. An example of the fits with the three backgrounds is reported in Figure 2.19, Figure 2.20, and Figure 2.21. Two quantities are shown in the plots: the number of neutrons estimated in the peak (green) and the reduced χ^2 of the fit (black). The former is used to compute the efficiency; the latter permits the evaluation of the fit. In particular, the fit performed with the Chebyshev background is not good enough to be used in the efficiency evaluation, while there are no significant differences between the Weibull and Crystalball fits. The number of neutrons is estimated as the integral in $(\mu - 3\sigma, \mu + 3\sigma)$ region of the Gaussian associated with the peak at 0.94 GeV, the associated error is only the statistical error obtained as the square root of the count. Being the Weibull and Crystalball similar, their average was taken to evaluate $\eta_{\pi \rightarrow \pi}$ and $\eta_{\pi \rightarrow K}$. The data were binned in the hadron momentum p_H inside the working range of the detector: (3, 4), (4, 5), (5, 6), (6, 8). The results are reported in Figure 2.22, and they show that the RICH effectively reduces contamination of pions into the kaon sample. In particular:

- The CLAS12 efficiency on pion detection, obtained using the FTOF and the HTCC, is maximum below the 3 GeV and decreases while the hadron momentum increases;
- The RICH efficiency is essentially flat and close to the 100% in the RICH nominal momentum range
- The contamination of pion into the kaon sample using the CLAS12 PID increases with the momentum of the hadron.
- The contamination of pion into the kaon sample is strongly reduced using the RICH in the nominal momentum range between 3 and 8 GeV.

The last point is the main result of this preliminary study on the RICH efficiency because it validates the use of the RICH to select events for kaon Semi-Inclusive Deep Inelastic Scattering studies. The next Chapter will show how the kaon sample can be used to extract a Beam-Spin Asymmetry (BSA), the first step to obtain a new measurement of the nucleon structure functions.

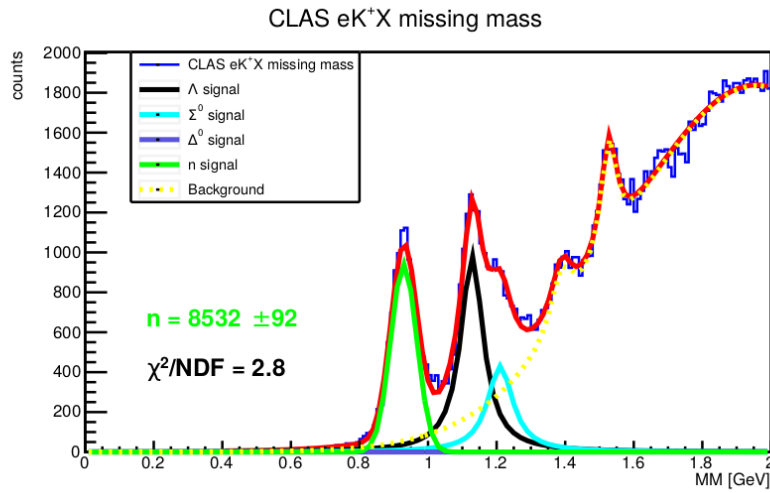


(a) Missing mass of eK^+X selected by CLAS12 PID fitted using Weibull background.

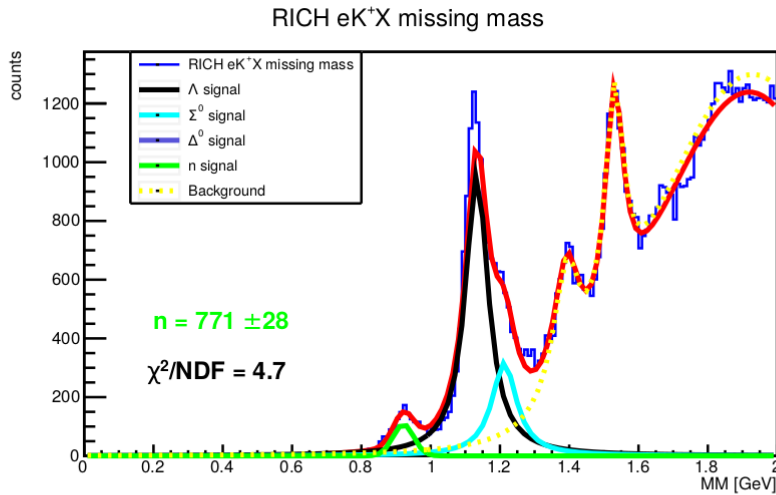


(b) Missing mass of eK^+X selected by RICH fitted using Weibull background

Figure 2.19: Example of missing mass of eK^+X with SIDIS background fitted using the weibull function. The green number is the number of neutrons associated with the peak; the black number is the reduced χ^2 used to evaluate the fit quality.

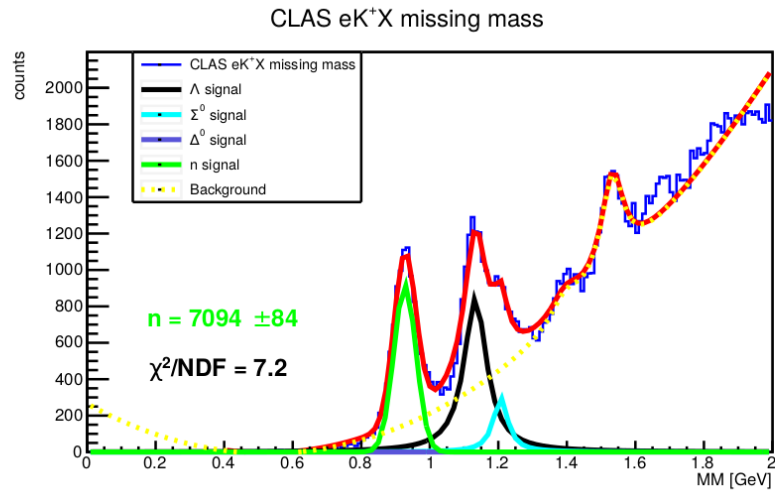


(a) Missing mass of eK^+X selected by CLAS12 PID fitted using Crystalball background.

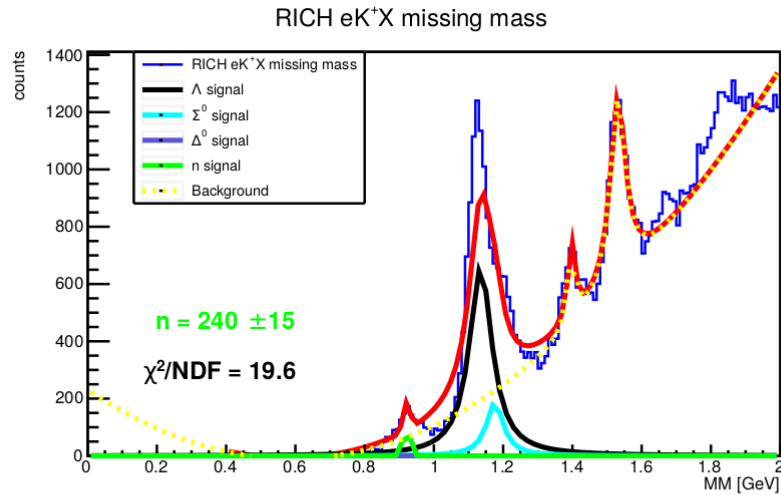


(b) Missing mass of eK^+X selected by RICH fitted using Crystalball background

Figure 2.20: Example of missing mass of eK^+X with SIDIS background fitted using the Crystalball function. The green number is the number of neutrons associated with the peak; the black number is the reduced χ^2 used to evaluate the fit quality.

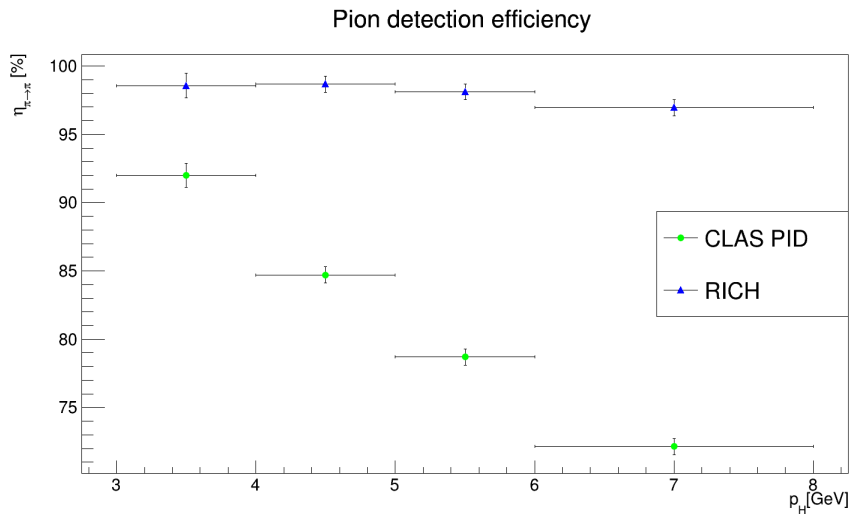


(a) Missing mass of eK^+X selected by CLAS12 PID fitted using Chebysev background.

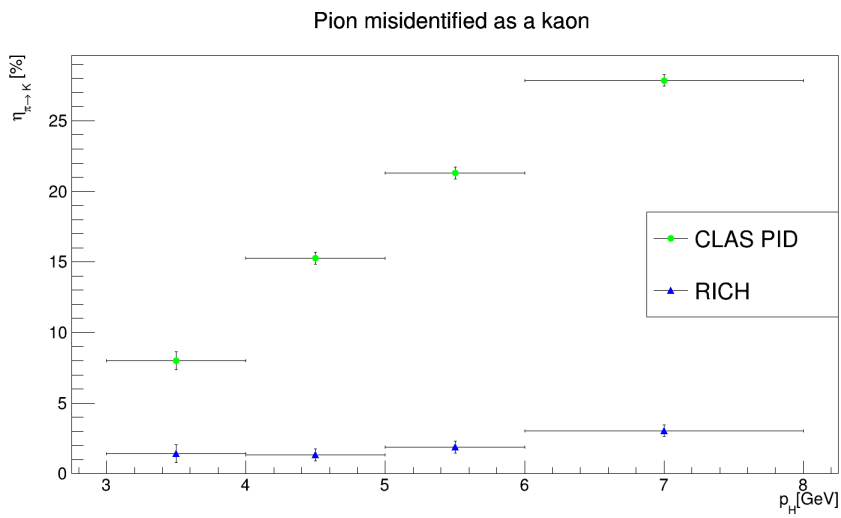


(b) Missing mass of eK^+X selected by RICH fitted using Chebysev background

Figure 2.21: Example of missing mass of eK^+X with SIDIS background fitted using the Chebysev function. The green number is the number of neutrons associated with the peak; the black number is the reduced χ^2 used to evaluate the fit quality.



(a) Pion detection efficiency as a function of the hadron momentum.



(b) Percentage of pion misidentified as being a kaon as a function of the hadron momentum.

Figure 2.22: Results of the efficiency analysis

Chapter 3

SIDIS with CLAS12

Chapter 1 introduced polarized Semi-Inclusive Deep Inelastic Scattering (SIDIS) as a powerful tool for investigating the nucleon's internal structure, allowing access to the Transverse-Momentum-Dependent distributions (TMDs). This Chapter aims to outline a preliminary analysis of the Beam-Spin Asymmetry (BSA) associated with the structure-function $F_{LU}^{\sin\phi}$. It is treated as a case study of a possible measurement of non-perturbative QCD with flavor sensitivity made possible by having an efficient PID apparatus. The analysis is performed on data acquired by the CLAS12 experiment at JLab, using the first module of the RICH installed in 2018; the second module was not available then. It is based on the efficiency study reported in Chapter 2, which guarantees minimal pion contamination in the eK^+X sample. The study aims to show that it is possible to extract the Beam-Spin Asymmetry on kaons despite the reduction of the statistics caused by the relatively smaller phase space covered by the RICH compared to the full CLAS12 spectrometer. The SIDIS data selection criteria, the analysis method, and the results are included in this Chapter.

3.1 Data

The CLAS12 Run Group B (RG-B) acquired the analyzed data in the spring of 2019. The target was unpolarized liquid deuterium, and the longitudinally polarized electron beam was run at 10.6 GeV and 10.2 GeV with a current of 50 nA. The average beam polarization was 84.8 ± 1.5 ; it was monitored during the data-taking period by frequent Moeller scans. The beam helicity was swapped with a frequency of 30 Hz to minimize the systematic effects. The torus magnet was full-field inbending, pushing positive particles forward.

The analysis is performed on positive kaons: the final state is eK^+X . The standard CLAS12 reconstruction provides the electron identification and the kinematic of the particles, while it is expressly required that the RICH identify the kaon. These conditions reduce the available statistic because, at





the time of data collection, only one of the six CLAS12 sectors was equipped with a RICH module. The analyzed data sample constitutes approximately one-third of the available statistics of electroproduction on deuterium and one-tenth of that on hydrogen and deuterium.

3.1.1 The CLAS12 SIDIS cuts

The final states, which include one electron and one positive kaon, are considered in this analysis. For the electron selection, the standard CLAS12 conditions for SIDIS were applied [9]:

- It has to be in the Forward Detector, ~~then~~ the polar angle is between 5° and 40° .
- It has to be a trigger particle for the experiment.
- The number of photoelectrons in the HTCC has to be greater than 2.
- The energy in the PCAL has to be greater than 0.07 GeV.
- The DC fiducial cut developed for Run Group A was applied (running conditions were quite similar, except for the target that was hydrogen instead of deuterium).
- The z coordinate of track vertex was selected to be between -8 mm and 3 mm.
- The so-called “diagonal cut” is applied for the electron with momentum larger than 4.5 GeV. In this momentum range, the HTCC showed some inefficiency in distinguishing electron and pion, which can be cured using this cut based on the ratio of the energy deposited in the pre-shower and inner calorimeter.

For the kaon selection, ~~the~~ following conditions were applied:

- It has to be identified by the RICH;
- ~~Aiming to show the role of the RICH,~~ the momentum is selected to be included in the detector working range ($3 \div 8$ GeV);
- The number of photoelectrons in the RICH has to be greater than 2, to well-define the ring.
- The DC fiducial cut developed for Run Group A was applied (running conditions were quite similar, except for the target).
- The z coordinate of track vertex was selected to be between -10 mm and 2.5 mm.



- Having the particle track a key role in the ring reconstruction, which is based on a ray-tracing algorithm, it requests of having a reduced $\chi_{track}^2 < 8$.

After the selection of the particle, the following cuts based on the kinematic were applied:

- $y < 0.75$;
- $Q^2 > 1 \text{ GeV}^2$;
- $z > 0.2$;
- $x_F > 0.0$;
- $W > 2$;
- $MM > 1.6 \text{ GeV}$;

where y is the fraction of electron energy transferred to the target, Q^2 is the transferred momentum, z is the fraction of electron energy acquired by the kaon, x_F is the so-called Feymann x , the fraction of the nucleon momentum carried by the parton struck by the electron, W is the center of mass energy, and MM is the missing mass of the reaction.

The selection criteria mostly reducing the statistics are the fiducial cut on DC for the kaon ($\sim 47\%$ events survive), the reduced χ_{track}^2 cut ($\sim 51\%$), the minimum number of photons in RICH ($\sim 55\%$), and the cut on y ($\sim 57\%$). A not negligible effect is also associated with the z-vertex hadron cut, the missing mass cut, and the “diagonal” cut ($\sim 80\%$ events survive). The other cuts have an event-survival rate larger than 90%. These values are the specific effect of each selection criterion. The total survival rate, computed as the ratio between the number of events after applying all cuts and the initial number of events, including a kaon passing through the RICH, is $\sim 4\%$.

The effect of the DC fiducial is not directly shown because of the implementation based on a function appositely defined by another member of the collaboration and provided as boolean information; they are based on the evaluation of the track reduced χ^2 variation, as represented in Figure 3.1. An example of the area covered by the DC applying the fiducial cut is shown in Figure 3.2. The effects of the other main cuts are shown in Figures 3.3, 3.4, 3.5, 3.6, and 3.7, where the blue and the red lines represent the distribution of the variables before and after the application of all the cuts, and the green lines show (if present) the value of the cut applied. It is difficult to directly show the “diagonal cut” effect on the electron. However, its effect is clearly in the reduction of the statistics below and above 4.5 GeV in the electron momentum distribution reported in Figure 3.8b. The phase space covered by the particles surviving the selection is shown in Figure 3.8, while the distributions as a function of Q^2, x_B, z, p_T are represented in Figure 3.9.

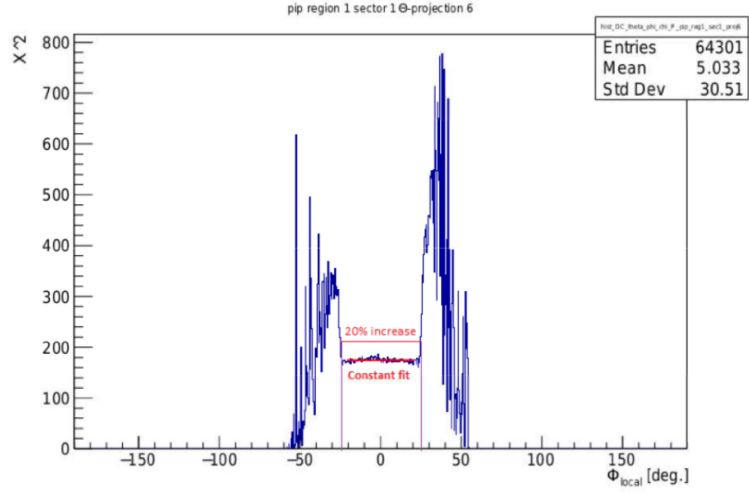


Figure 3.1: Procedure of the DC fiducial cut definition. For each region (3) of the DC and for each sector (6), a study of the χ^2 variation was performed to define the fiducial cuts.

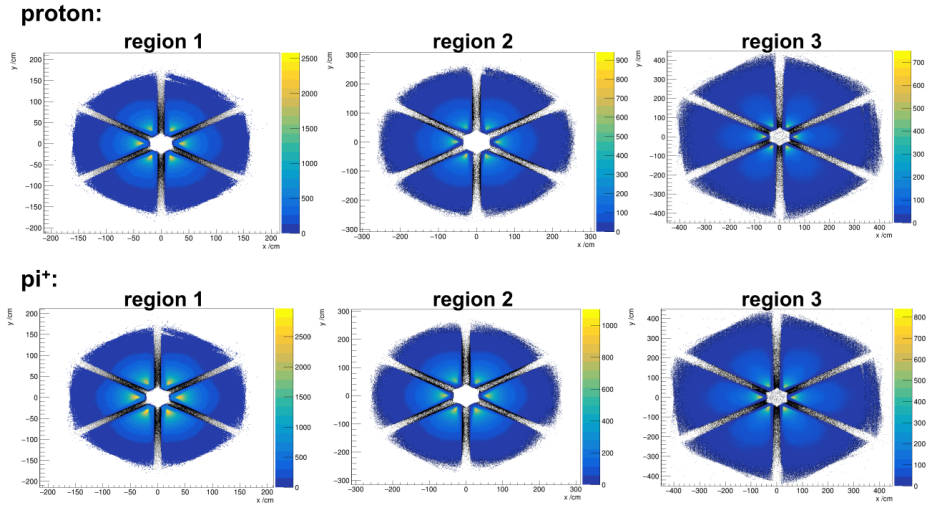


Figure 3.2: Area covered by the DC applying the fiducial cut. Example of the three region distribution for proton and pion.

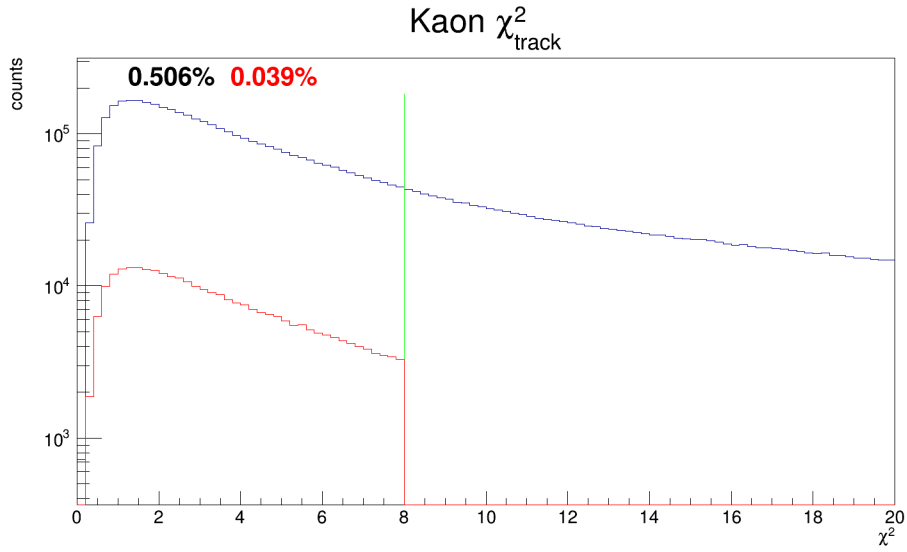


Figure 3.3: Reduced χ^2 of the hadron's track before (blue) and after (red) the application of all selection criteria. The cut applied on this distribution is represented by the green line. The numbers represent the percentage of events surviving this cut (black) or all cuts (red).

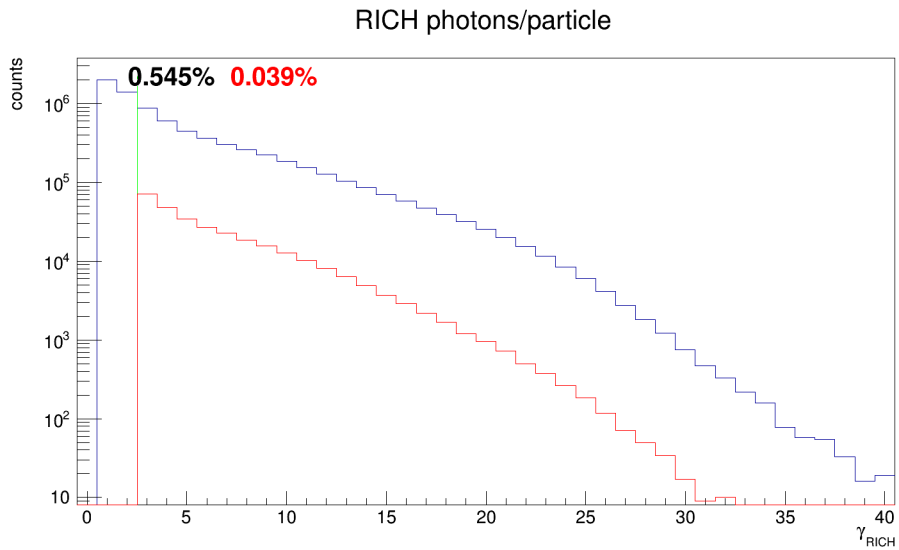


Figure 3.4: Number of photons for particle detected by the RICH before (blue) and after (red) the application of all selection criteria. The cut applied on this distribution is represented by the green line. The numbers represent the percentage of events surviving this cut (black) or all cuts (red).

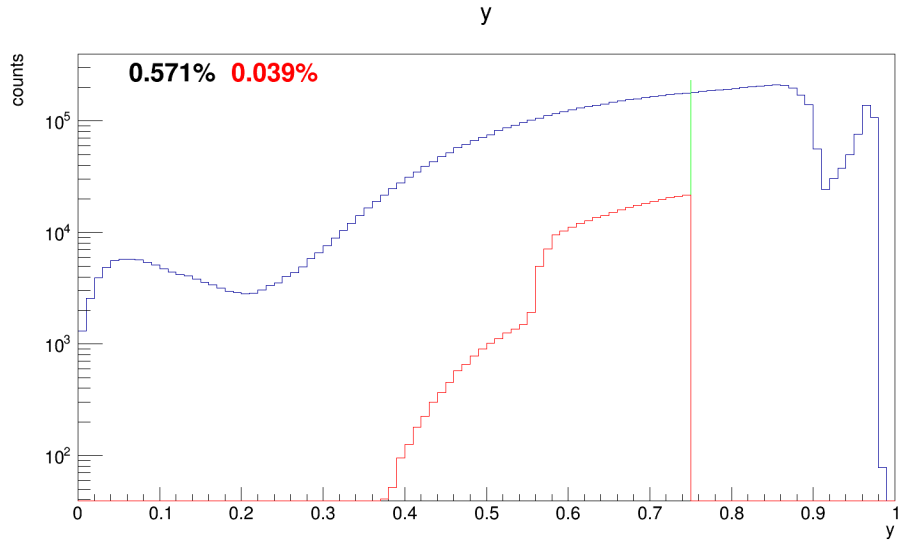


Figure 3.5: Distribution of the DIS y variable before (blue) and after (red) the application of all selection criteria. The cut applied on this distribution is represented by the green line. The numbers represent the percentage of events surviving this cut (black) or all cuts (red).

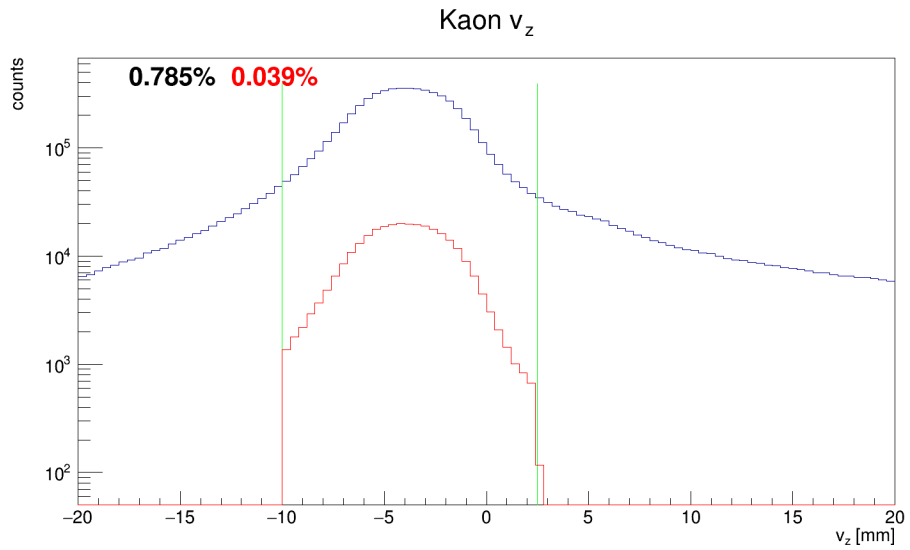


Figure 3.6: Distribution of the z component of the hadron vertex before (blue) and after (red) the application of all selection criteria. The cut applied on this distribution is represented by the green line. The numbers represent the percentage of events surviving this cut (black) or all cuts (red).

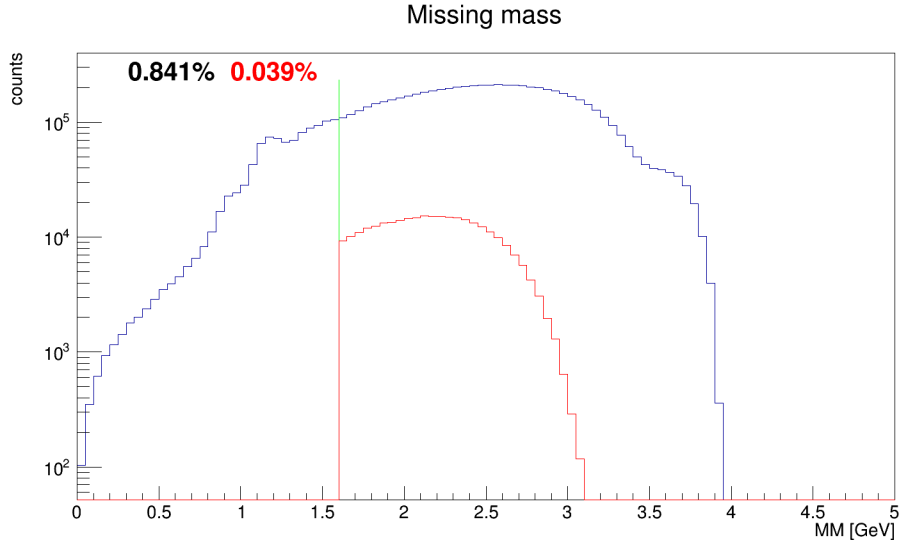
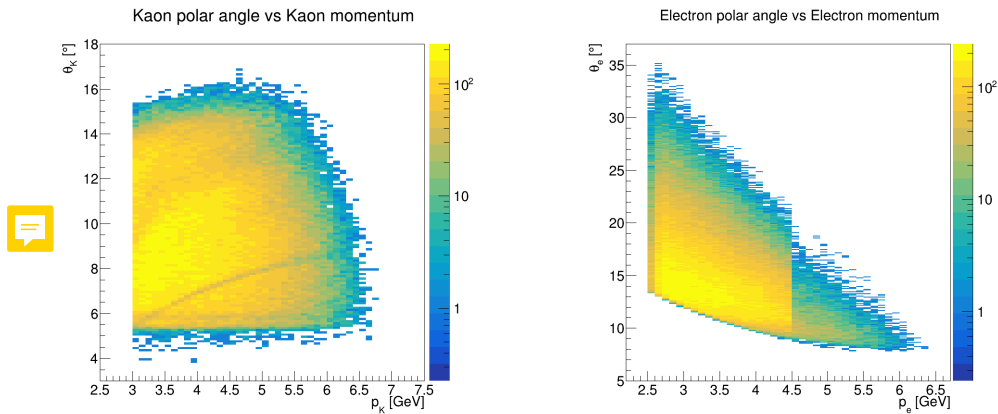


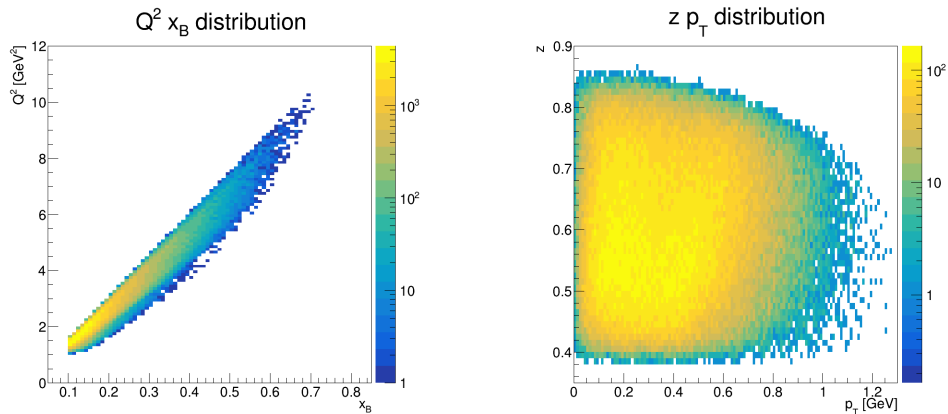
Figure 3.7: Missing mass distribution before (blue) and after (red) the application of all selection criteria. The cut applied on this distribution is represented by the green line. The numbers represent the percentage of events surviving this cut (black) or all cuts (red).



(a) Distribution of the polar angle and momentum of the selected kaons. The slightly darker line depends on the small separation between the two regions covered by the aerogel.

(b) Distribution of the polar angle and momentum of the selected electrons. The separation line visible at 4.5 GeV is due to the “diagonal cut”.

Figure 3.8: Phase space covered by the selected events.



(a) Distribution of events as a function of the Q^2 and x_B variables.

(b) Distribution of events as a function of the z and p_T variables.

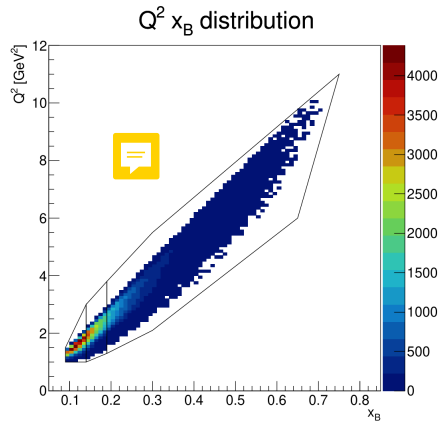
Figure 3.9: Distribution of events in the four-dimension of interest.

3.1.2 Binning

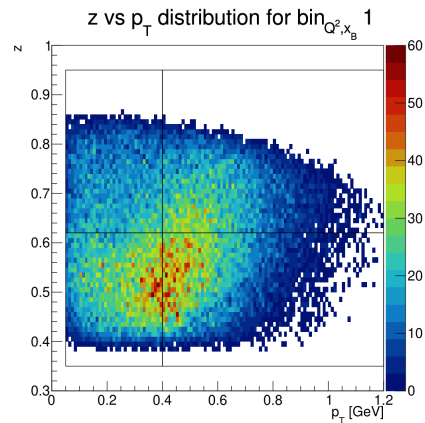
Section 1.4 reported the structure functions are dependent on x_B , Q^2 , z , and p_T . To provide most information on TMDs, trying to add constraints for theoretical models, the BSA is evaluated by applying a four-dimensional binning in x_B, Q^2, z, p_T . Aiming to show a preliminary measurement of the asymmetry and evaluate the PID system effects, the BSA is evaluated using a one-dimensional binning also on the same variables. The one-dimensional binning is defined independently from the number of events included in each bin, aiming to show the existence of the asymmetry and that it depends on the variables. The four-dimensional binning is defined in two steps; the first is applying a binning on Q^2 and x_B , each for each of these bins, a specific division on z and p_T . This procedure follows the one used for the $e\pi^+X$ analysis in Reference [11]. The criteria to define the four-dimensional binning are to maximize the number of bins having a sufficient statistic to perform the analysis, decided to be in the order of 10^4 events. The binning for the kaon sample is shown in Figure 3.10.

3.2 Analysis

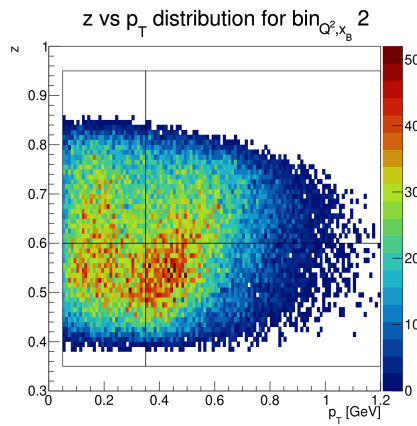
Since the available statistic is limited, the Unbinned Maximum Likelihood (UML) method was selected to obtain the measurement. It requires more computational resources but provides more reliable results with low statistics because it computes the asymmetry term event-by-event instead of using a cumulative histogram. The analysis software was developed by the author using C++ and Clas12root, a framework derived from ROOT CERN that includes methods to read the CLAS12 data files, that are in Highly



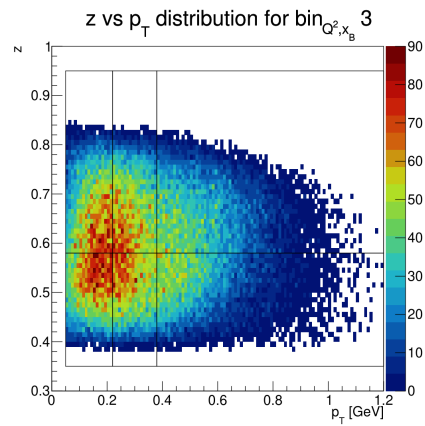
(a) Binning applied to the Q^2, x_B variables for kaons.



(b) Binning applied to the z, p_T variables for the first bin of Q^2, x_B .



(c) Binning applied to the z, p_T variables for the second bin of Q^2, x_B .



(d) Binning applied to the z, p_T variables for the third bin of Q^2, x_B .

Figure 3.10: Distribution of events in the four-dimension of interest.

Performance Output (HIPO) format.

3.2.1 The Unbinned Maximum Likelihood Fit

The UML Fit method is based on the assumption that the Probability Density Function (PDF) associated with the i event has the same functional form of the cross-section

$$PDF(x_i, \alpha) = \sigma_{UU}(1 + A_i(\alpha)) \quad (3.1)$$

where x_i is the set of variables associated with the event, α is a set of parameters, σ_{UU} is the unpolarized cross-section, and A_i is a term to take account of the researched asymmetry. If the unpolarized cross-section does not depend on the parameters of the fit, as it happens in this case, the PDF became

$$PDF(x_i, \alpha) = 1 + A_i(\alpha) \quad (3.2)$$

The likelihood function for a set of N events can be obtained as

$$\mathcal{L} = \prod_{i=1}^N PDF^{norm}(x_i, \alpha) \quad (3.3)$$

where PDF^{norm} is the normalized PDF. Applying the logarithm to the \mathcal{L} permits the transformation of the product into a sum, making easier the computation. It obtains

$$\log \mathcal{L} = \sum_i^N \log [PDF^{norm}(x_i, \alpha)] \quad (3.4)$$

Under the hypothesis of a large sample of independent measurements, the logarithm of the likelihood behaves like a χ^2 .

$$\chi^2 = -2 \log \mathcal{L} \quad (3.5)$$

so it is possible to extract the most probable value of the asymmetry by minimizing the χ^2 .

To extract the $A_{LU}^{\sin \phi}$ asymmetry, the PDF is

$$PDF_{\pm}(x_i, A_{LU}^{\sin \phi}) = 1 \pm P_b(A_{LU}^{\sin \phi} \sin \phi_i) \quad (3.6)$$

where the sign changes following the helicity of the beam, and P_b is the beam mean polarization. This PDF is automatically normalized, so it can be used directly in the definition of the likelihood

$$\log \mathcal{L} = \sum_i^{N^+ + N^-} \log \left[1 \pm P_b \left(A_{LU}^{\sin \phi} \sin \phi_i \right) \right] \quad (3.7)$$

The $F_{LU}^{\sin\phi}$ term is related to the BSA $A_{LU}^{\sin\phi}$ by equation

$$A_{LU}^{\sin\phi} = \frac{\sqrt{2\varepsilon(1-\varepsilon)}F_{LU}^{\sin\phi}}{F_{UU}} \quad (3.8)$$

where ε is a kinematic factor defined in Equation 1.11. Then, the likelihood is

$$\log \mathcal{L} = \sum_i^{N^++N^-} \log \left[1 \pm P_b \left(\frac{\sqrt{2\varepsilon(1-\varepsilon)}F_{LU}^{\sin\phi}}{F_{UU}} \sin \phi_i \right) \right] \quad (3.9)$$

and it is sufficient to minimize $-2\mathcal{L}$ to find the value of the asymmetry.

This method has the advantage of being independent of the binning in ϕ and provides results also if applied to relatively small samples. Against the UML method, it requires large computation resources to perform the minimization over thousands of events, and it is not always easy to define the PDF and its normalization. In the case of the extraction of $F_{LU}^{\sin\phi}$ for kaon, the pros appeared more relevant than the cons, so the UML was selected.

3.2.2 UML fit validation

The UML fit is implemented using the ROOT::Math::Minimizer class, which allows the minimization of a function depending on one or more parameters. The software was validated on $e\pi^+X$ data acquired by the Run Group A (RG-A). They are a subsample of data used for the π^+ BSA measurement described in Reference [11], constituting $\sim 5\%$ of the data available from RG-A. The validation process was made using the CLAS12 reconstruction software, excluding the RICH. The same 4-dimensional binning of the paper was used. The events are divided into 9 bins in Q^2, x_B , each one containing $\sim 35 \div 40$ bins for a total of 344. The binning in the first two variables and one example for the other two are reported in Figure 3.11. Not all the bins were used for validation because of the limited number of events and the dense bins. They are considered acceptable if the number of events is larger than 10^4 . The results reported satisfy this requirement on the number of events.

The comparison of the part of the results is reported in Figure 3.12. The plots show that the results, which are reported with just the statistical error, are comparable with the values taken from the attached material to the Reference [11].

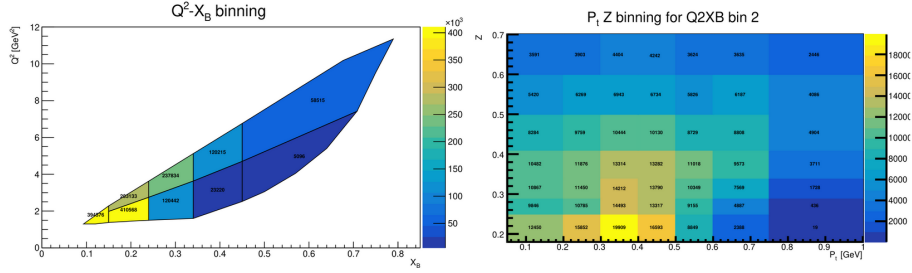


Figure 3.11: Binning defined for pion sample. On left the binning in Q^2, x_B , on right the binning in z, p_T for the second bin in Q^2, x_B .

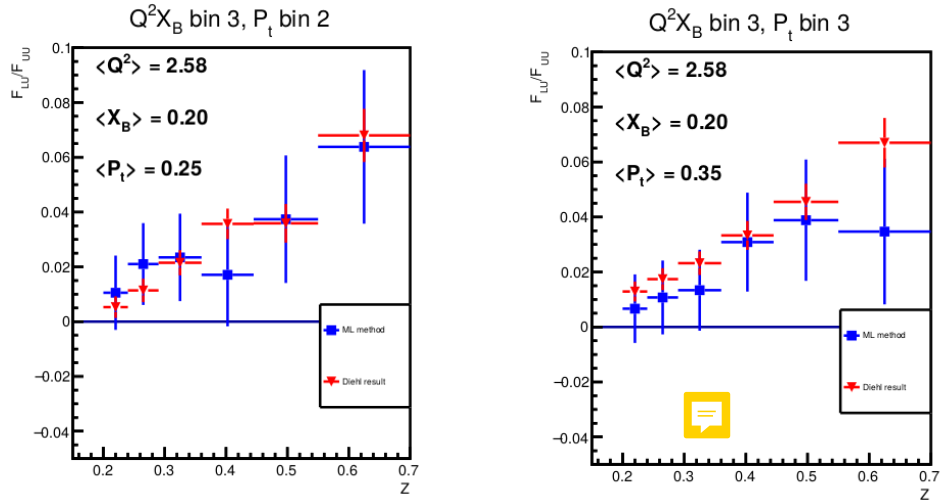


Figure 3.12: Validation of the Unbinned Maximum Likelihood (UML) fit. The plots show the comparison of $\frac{F_{LL}}{F_{UU}}$ values obtained from the UML fit (blue) and reported in the Reference [11] (red).

3.3 Results

The analysis is still incomplete because it is beyond the scope of this work¹. The aim is to show that the BSA exists for kaons and it is detectable at CLAS12, and that the BSA is not simply caused by the pion contamination on the kaon sample. For this reason, the systematic error is not evaluated; the statistical error provided by the minimization methods is reported in the plots.

3.3.1 One-dimensional results

The one-dimensional results are shown as a function of one of the variables Q^2 , x_B , z , p_T in Figure 3.13 and Figure 3.14. They show that the asymmetry is detectable using the CLAS12 spectrometer for kaons identified by the RICH. Moreover, for Q^2 and p_T , a dependence of the asymmetry from the variable is visible in the respective plots. The dependence does not appear in the x_B and z plots; investigating it will require more study, increasing the statistics, and comparing it with the simulation.

3.3.2 Four-dimensional results

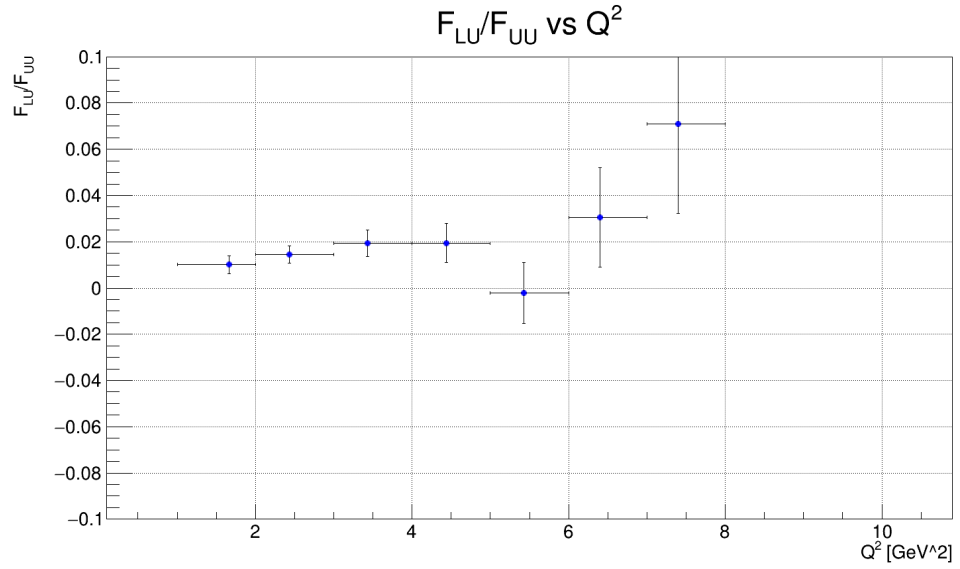
The results obtained after applying the four-dimensional binning described in the previous section to the kaon sample identified by the RICH are shown in Figure 3.15, Figure 3.16, and Figure 3.17.

3.3.3 Future SIDIS studies using the CLAS12 RICH

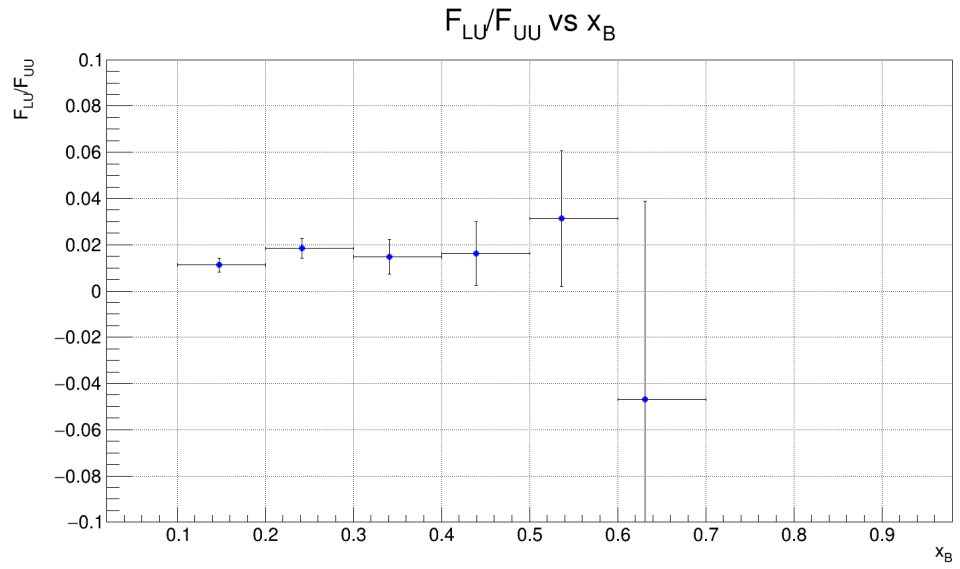
This Chapter showed it is possible to extract an asymmetry for kaon despite the reduction of statistics it caused. The addition of the second module of the detector, which occurred in 2022, will increase the available statistics, allowing us to divide the data in more dense bins, providing more information to constrain the TMDs. In the immediate future, the analysis will be extended to the full sample of scattering on deuterium, including several runs acquired with the torus with opposite polarization. Moreover, the completion of the RICH alignment in the reconstruction software will permit the extension of the phase space covered up to the expected value of 26° . To ultimate the measurement, the data for kaons with momentum lower than 3 GeV, identified by the standard CLAS12 PID without the RICH will be added to extend the phase space. The evaluation of the systematic error will complete the analysis.

Confirming that the kaon sample provided by the RICH permits obtaining the asymmetries, will help several studies that are ongoing on kaons, like the

¹The analysis work will not remain unfinished. It was impossible to complete it before the end of the Ph.D. period, but the author will continue to work with the CLAS12 spectrometer and conclude the analysis, aiming to obtain a publication.

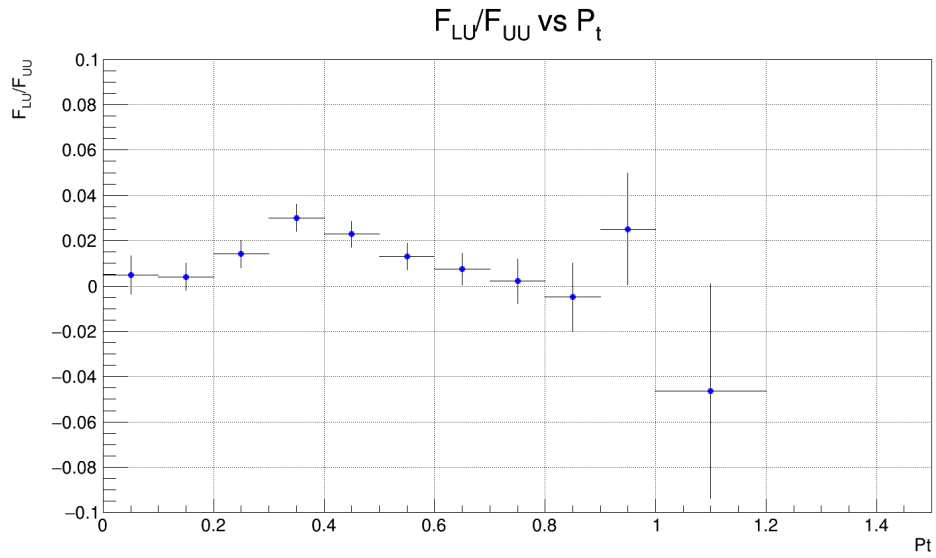


(a) F_{LU}/F_{UU} as a function of Q^2 .

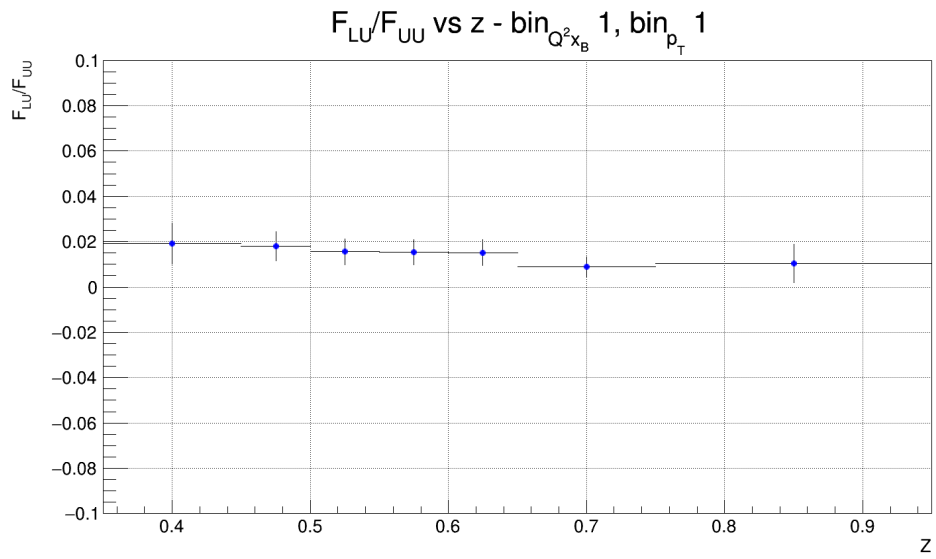


(b) F_{LU}/F_{UU} as a function of x_B .

Figure 3.13: Plots of the asymmetry expressed as a function of Q^2 and x_B . It shows that the asymmetry for kaon is present also after removing the pion contamination.



(a) F_{LU}/F_{UU} as a function of p_T .



(b) F_{LU}/F_{UU} as a function of z .

Figure 3.14: Plots of the asymmetry expressed as a function of p_T and z . It shows that the asymmetry for kaon is present also after removing the pion contamination.

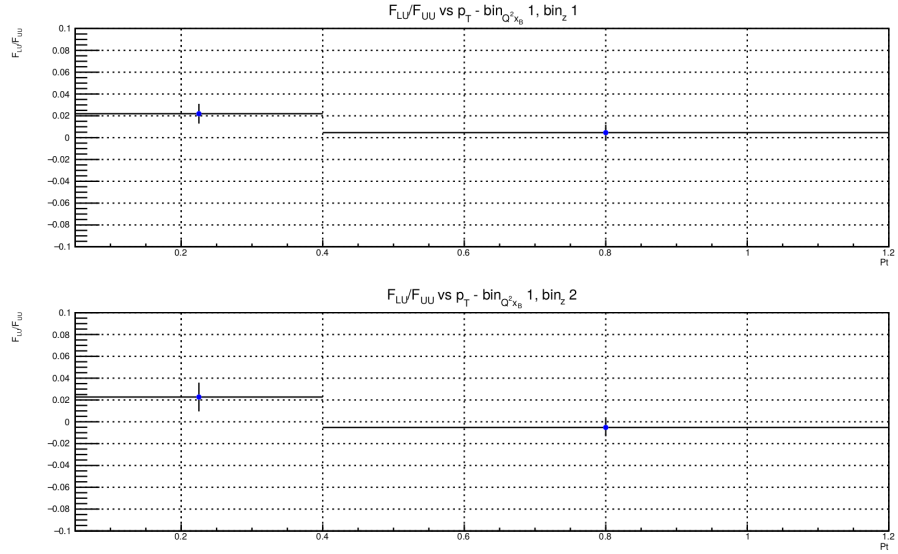


Figure 3.15: F_{LU}/F_{UU} for the first bin in Q^2, x_B and for the two bins in z , as a function of p_T .

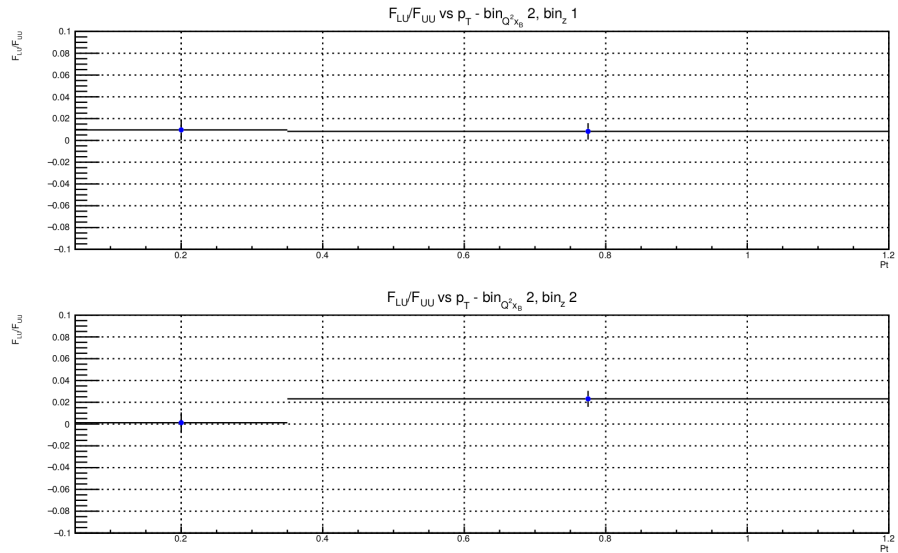


Figure 3.16: F_{LU}/F_{UU} for the second bin in Q^2, x_B and for the two bins in z , as a function of p_T .

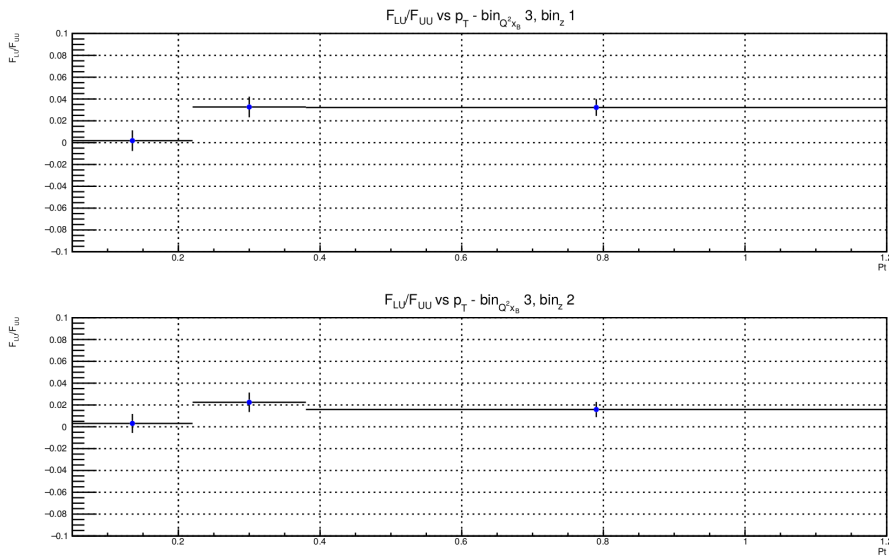


Figure 3.17: F_{LU}/F_{UU} for the third bin in Q^2, x_B and for the two bins in z , as a function of p_T .

measurement of other terms of the SIDIS cross-section or the dihadron SSAs including at least one kaon. Moreover, the study of the higher-momentum kaon SIDIS permits access to the high z region, providing the possibility of more investigation, for example, about the role of vector mesons.

Chapter 4

The EPIC dual-radiator RICH

This Chapter focuses on the new world-leading tool to explore the low energy Quantum Chromodynamics (QCD), the Electron-Ion Collider (EIC), providing precision 3D imaging of protons and nuclei, aiming to solve the proton spin puzzle, investigating the quark and gluon confinement, and measuring the distribution of quarks and gluons in the nuclei. The author developed the dual-radiator Ring Imaging Cherenkov (dRICH) for the Electron-Proton/Ion Collider Experiment (ePIC) experiment, a key component for identifying the hadrons produced in the collisions. Mainly, the author contributes to the studies on the prototype performed on several test beams between 2021 and 2023, developing the analysis software and the simulation, characterizing the aerogel radiator elements, and handling the tracking system during the data acquisition. The results obtained by the prototype are comparable with the expectation derived from the simulation and satisfy the requirements for the experiment.

4.1 The EPIC experiment at the Electron-Ion Collider

The EIC [10] is the new large-scale accelerator machine, which will be built at Brookhaven National Laboratory (BNL) on Long Island, New York, USA. The EIC will collide high-energy electron beams with high-energy proton and ion beams. By colliding these polarized beams, the EIC will access the nucleon's structure functions with unprecedented precision. It will exploit high-intensity beams that will allow running with higher luminosity. The EIC will be the instrument allowing the investigation of the new frontier of the QCD. The main design requirements of the EIC are:

- Large ion species for the beam, from proton to uranium;

- Highly polarized beams $\sim 70\%$;
- Variable e+p center-of-mass energies from $20 \div 140$ GeV;
- High collision electron-nucleon luminosity $10^{33} \div 10^{34} \text{ cm}^{-2}\text{s}^{-1}$;
- Up to two general-purpose detectors.

The EIC will replace the Relativistic Heavy Ion Collider (RHIC), the machine at BNL that will operate until 2025. A scheme of the new accelerator is represented in Figure 4.1.

The first detector will be run by the 2022-born Electron-Proton/Ion Collider Experiment (ePIC) collaboration and placed into the IP6. The ePIC collaboration includes 171 institutions from 24 countries and more than 500 participants. According to the scheme in Figure 4.2, ePIC will be made by a barrel-shaped central detector built around a 2 T solenoidal magnet, a far-forward electron detector, and a far-backward hadron spectrometer. These three detectors contribute to covering the whole phase space of the asymmetric lepton-hadron collider. Indeed, the three parts of the experiment can see very different particles in terms of both momentum and particle types.

The magnet

The ePIC magnet will be the MAgnet with Renewed COils (MARCO), a 3.5 m long superconductive solenoid measuring 2.84 m of bore diameter at room temperature, providing a 2 T on-axis field directed along the beamline. The MARCO will operate at 4.5 K.

The tracking and vertexing system

The ePIC tracking has to efficiently recognize patterns, provide a low material budget not exceeding $5\%X/X_0$, work inside the magnetic field, satisfy the geometrical constraints imposed by the solenoid in the barrel detector, and disentangle signal and background. The system under development is a concept detector based on semiconductor and gaseous tracking technologies to ensure satisfactory space resolution, the measured space point coordinates redundancy and good time resolution. In particular, it will be based on the Monolithic Active Pixel Silicon (MAPS) tracker, providing the spacial resolution, and Multi-Pattern Gas Detectors (MGPDs), that can be implemented as μ MEGAS or μ RWELL to provide the redundancy and the time resolution lower 10 ns.

The calorimetry system

The ePIC calorimetry system had to measure the particle's energy, provide continuous acceptance over the entire rapidity spectrum, be insensitive to

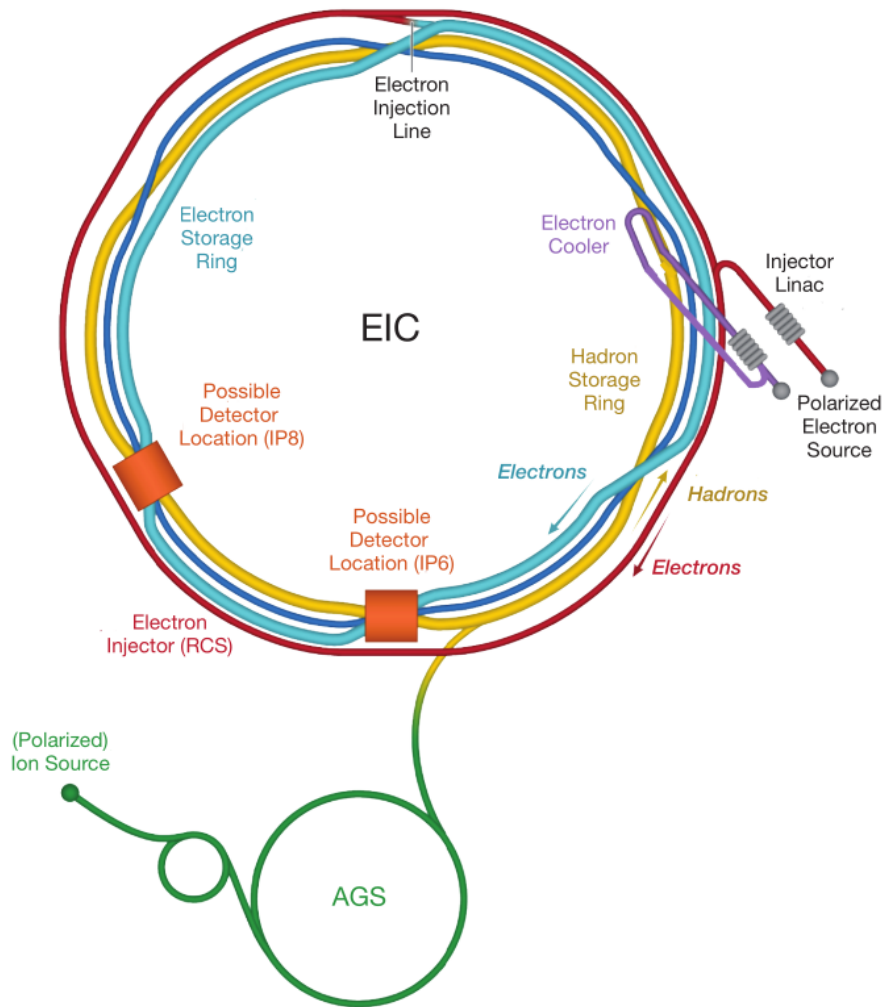


Figure 4.1: Scheme of the Electron-Ion Collider. The ePIC experiment will be placed into IP6.

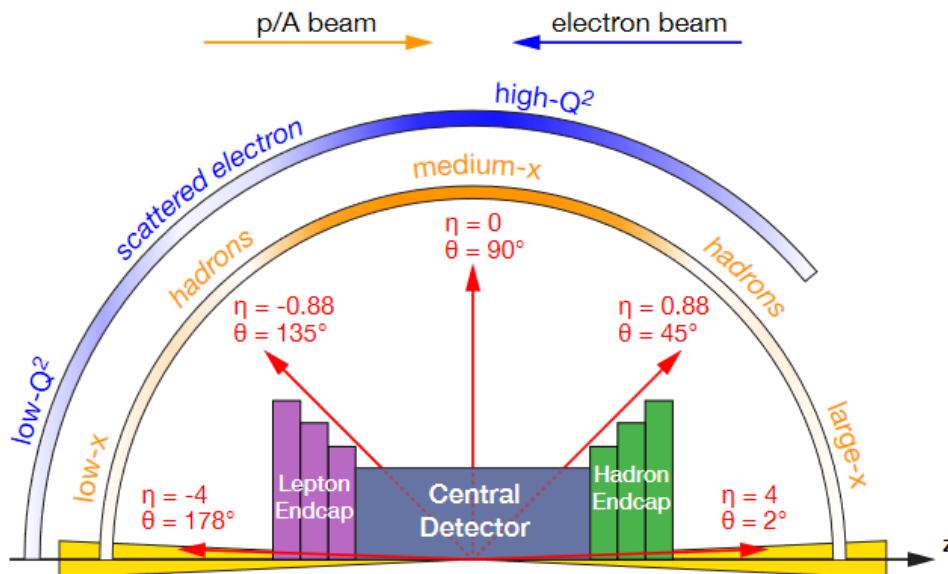


Figure 4.2: Scheme of the ePIC detector

the magnetic field, and operate at the total luminosity in the expected background conditions. It must also contribute to distinguishing electrons and photons and measure the particle's angle and position.

The Barrel Electromagnetic Calorimeter requires an energy resolution lower than $\frac{7\%}{\sqrt{E}} \oplus 1\%$ and a fine granularity for good $\gamma - \pi^0$ separation. It has to measure energy low to 100 MeV and up to 10 GeV. These requirements must be achieved in a minimal space due to the geometrical constraints imposed by the solenoid. The detector will be a sampling calorimeter based on 6 layers of Astropix sensors alternate by 5 layers of lead and scintillating fibers 2-sided read by SiPMs. The Astropix are SiPM developed for the Amegox NASA missions and are used for electromagnetic shower imaging. The 2-sided read scintillating fibers are used to profile the longitudinal dimension. This permits to obtain a deep but still very compact calorimeter ($\sim 17X/X_0$ in 40 cm), an excellent energy resolution ($\frac{5.2\%}{\sqrt{E}} + 1\%$), an unrivaled low-energy electron-pion separation by combining energy measurement and imaging, and exceptional position resolution. Moreover, it is deep enough to serve as the inner layer of the hadronic calorimeter.

The Barrel Hadronic Calorimeter aims to reconstruct jet energy precisely, provide a secondary determination of scattered electron kinematics, and help in muon identification. Moreover, it will also serve as part of the solenoid flux return. These will be done by refurbishing the sPHENIX outer HCAL, a cylinder of inner and outer radius 1.9 m and 2.6 m, 6.5 m long, made by 32 sectors including 48 towers of scintillators. The refurbishment plan includes:

- To substitute the SiPMs and the readout electronics

- To check and re-characterize the scintillators, mapping them again.
- Eventually, to replace damaged scintillating tiles.
- To replace the slow control boards
- To repeat the sector-level calibration with cosmic rays.

This procedure, combined with the studies on simulation about the difference between minimum ionizing particles and jet signals, will allow it to achieve all the requirements.

The Backward Electromagnetic Calorimeter plays a crucial role in almost every physics channel that can be studied because it is responsible for detecting and measuring the kinematic of the scattered electron in the backward region, with rapidity $-3.5 < \eta < -1$. In particular, its goals are to separate electrons and pions, to provide a suitable resolution for electron detection at large $|\eta|$, to measure photons with good resolution, and to separate the 2γ from π^0 at high energy. The requirements for this detector are:

- Energy resolution of $\frac{2\%}{\sqrt{E}} + (1 \div 3)\%$
- Pion suppression $1 : 10^4$
- Minimum detection energy 50 MeV

It will comprise ~ 2850 $20 \times 20 \times 20$ cm³ PWO crystals that fill a circle around the beamline. Each crystal will be read by 16 SiPMs connected to the front-end electronics. One of the most critical points regards the cooling system; thermal studies are ongoing to find the best solutions for efficiently cooling the system.

The Backward Hadronic Calorimeter shall provide the functionality of a tail catcher for the electromagnetic calorimeter in electron identification and for the jet kinematics measurement at small x_B . 10 alternating layers will make the detector of 4 cm-thick stainless steel and 4 mm-thick plastic scintillator Kuraray SCSN-81. The scintillator's light will be extracted by 0.83 mm wavelength shifter fibers and collected by SiPM. The front-end electronics will be selected to follow the other calorimetry systems.

The Forward Electromagnetic Calorimeter will cover the pseudo-rapidity range $\sim 1 < \eta < 4$, achieving an energy resolution of $\frac{10\% \div 12\%}{\sqrt{E}} + 2\%$, a good π^0/γ separation up to 50 GeV and contributing to the jet reconstruction. Moreover, it has to work in a magnetic region with expected neutron fluxes up to 10^{12} n/cm². It will be a sampling calorimeter of tungsten and scintillating fibers.

The Forward Hadronic Calorimeter will measure the energy with a resolution of $\frac{50\%}{\sqrt{E}} + 10\%$, with a minimum detected energy of 500 MeV. A high-granularity sampling calorimeter will cover the whole azimuthal angle by alternating small scintillator tiles and absorbing layers.

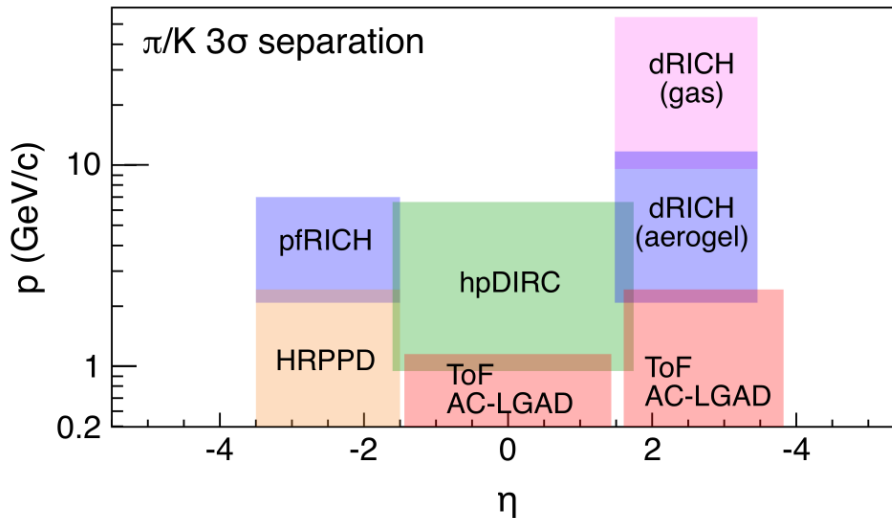


Figure 4.3: Phase space that needs to be covered by each PID subsystem.

Particle Identification System

The Particle Identification (PID) system plays a key role in QCD studies with flavor sensitivity, particularly for SIDIS. A plot reporting the phase space that needs to be covered by each PID subsystem is shown in Figure 4.3. In the backward direction, the proximity-focusing RICH will provide a 3σ separation between π and K up to 7 GeV. Moreover, using the High Rate Picosecond Photo-Detector, the pFRICH will provide a 20 ps-resolution time measurement for the Time-Of-Flight and a spatial resolution of ~ 1 mm. The TOF will provide 3σ separation of lower momentum pion and kaon in the barrel ($-1.4 < \eta < 1.4$, $0.2 < p < 1.2$ GeV) and in the forward endcap ($-1.74 < \eta < 3.83$, $0.2 < p < 2.3$ GeV).

The higher momentum hadrons will be detected in the barrel by the high-performance Detection of Internally Reflected Cherenkov light, a fast-focusing DIRC using a high-resolution 3D reconstruction. It will be made of 120 bars of radiator producing Cherenkov light over a focusing lens, and then the photons will pass through an expansion volume, hitting the photo-detector. It will provide a 3σ separation for π/K up to 6 GeV and for e/π up to 1.2 GeV.

This work focuses on designing the dual-radiator Ring Imaging Cherenkov (dRICH), a compact and cost-effective solution for broad momentum coverage at forward rapidity essential for SIDIS physics. It will interpolate the measurement of Cherenkov angles of photons produced crossing two different radiators to identify charged hadrons passed through the detector. This design is due to the most intriguing challenge for this detector: to identify charged hadrons in the momentum range between 3 and 50 GeV. Indeed, this

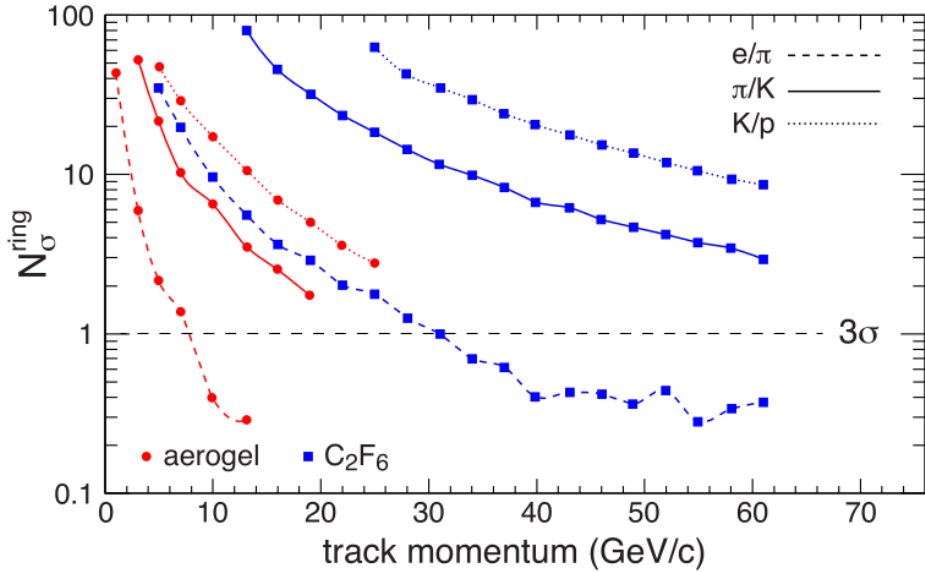


Figure 4.4: Expected separation achievable from the dRICH for a variety of particle species. Combining the aerogel and gas information provides uninterrupted PID across the full range.

momentum range crosses the region where the radiator is usually the aerogel and the one on which a gas is used. The dRICH will identify particles with pseudo-rapidity $1.5 < \eta < 3.5$ and help identify electrons with momenta lower than 15 GeV. This detector will challenge the specific challenge of working in a high magnetic field, in the order of 1 T, so the magnetic-insensitive sensors Silicon Photo-Multipliers (SiPMs) are expected to be used. Using the SiPM will face a different problem related to the radiation damage that will occur on them, increasing the dark count: a study on the recovery of the sensors via annealing was performed and described later in this work. The expected performance of the detector is described in Reference [10] and is reported in Figure 4.4. The rest of the Chapter will describe the ongoing studies on the recovery of SiPM radiation damage and the performances achieved with the prototype of dRICH assembled in Ferrara in 2021.

4.2 The recovery of SiPM radiation damage via annealing

It is expected that during the lifetime of the ePIC experiment, the photosensors of the dRICH will receive radiation in the order of $10^{11} \text{ n}_{\text{eq}}/\text{cm}^2$, which will dramatically affect the Dark Count Rate (DCR), increasing it over the acceptable rate of $\sim 100 \text{ kHz}$. Several options are available to maintain the DCR to an acceptable rate, namely by reducing the SiPM operating

temperature (cooling), using the timing information with high-precision Time-to-Digital converter electronics (gating), and recovering the radiation damage with high-temperature annealing cycles (curing). The cooling and gating procedures are known and will be used for the dRICH; the curing via annealing has been the subject of testing since 2021 and showed positive results that confirmed the possibility of using it for the final detector [15]. The following SiPM sensors have been studied:

- Hamamatsu S13360-3050VS and S13360-3025VS
- Hamamatsu S14160-3050HP and S14160-3015PS
- Fondazione Bruno Kessler (FBK) NUV-HD-CHK and NU-HD-RH prototype
- Onsemi MICROFJ-30035

The SiPM sensors have been irradiated on several occasions between 2021 and 2023 in the experimental room of the Trento Proton Therapy facility; this was done with 140 MeV protons produced in a large and uniform irradiation field [8]. The NIEL-scaling hypothesis is used to normalize the proton fluence to the corresponding 1-MeV neutron equivalent [22]. A dedicated collimator system was designed to deliver the uniform irradiation field in a 3 mm wide window such that thanks to a precision micrometric translation system, a single column of sensors (6 or 8 SiPM) in the matrix is irradiated at a given time. For each board, three different columns have been exposed at three different levels of irradiation: 10^9 , 10^{10} , and 10^{11} n_{eq} . The fourth column was used to control the background neutrons generated by the scattering system and the collimators. Background neutrons received by each board are estimated to correspond to $\sim 2 - 3 \times 10^8$ n_{eq} . Two pictures of the custom boards are shown in Figure 4.5. The sensors were characterized in a climate chamber, which provides a stable room temperature of -30 °C to control the background DCR.

The effect of the irradiation is represented in Figure 4.6a, which shows the increase of the dark current of the SiPM as a function of the radiation dose. It shows a linear increase with respect to the dose. The first annealing test was performed using an oven and with slow temperature increases, carrying out various characterization of the sensors during each phase with ~ 30 h annealing time between them. The results of these measurements are reported in Figure 4.6b, which shows the value of the DCR during this long annealing period. A reduction of the DCR of factor 20 is visible on the yellow points between the start and the end of the annealing. The systematic comparison of the annealing effect on different sensors is shown in Figure 4.7. It can be noted that the Hamamatsu S13360-3050VS had the lowest DCR before the irradiation and before and after the annealing, which makes it the most probable candidate to be used for the dRICH detector.

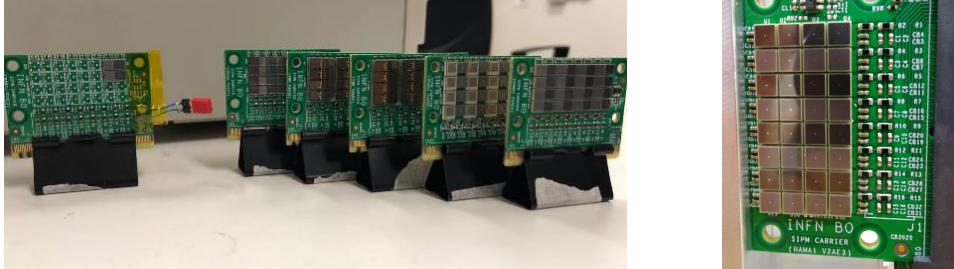


Figure 4.5: On the left, picture of the boards used for irradiation and annealing campaign. On the right is a close view of one board of SiPM. Each board hosts 4, 24, or 32 $3 \times 3 \text{ mm}^2$ sensors.

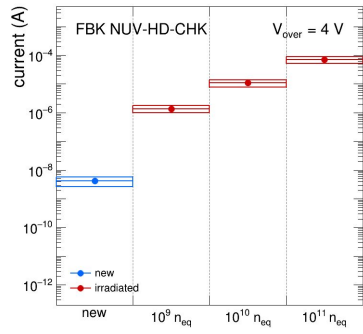
After the operation of ePIC starts, removing the sensors from the detector for the needed annealing cycles in the oven will be very complex. So, preliminary tests of online on-situ annealing made directly polarizing the SiPM are being performed. The online procedure consists of cycles of 30 min at $175 \text{ }^\circ\text{C}$ each time the sensor received a dose of $2 \times 10^8 \text{ n}_{\text{eq}}$. The temperature of the sensor can't overcome the threshold of $180 \text{ }^\circ\text{C}$, which is the operating limit of the protective layer of the entrance window and was kept under control using a thermal camera, as shown in Figure 4.8a. The plot to compare the oven and the online annealing is reported in Figure 4.8b and shows that the online annealing permits the reduction of the DCR of one order of magnitude. The oven annealing performance is better by a factor of 2, but the online procedure has several advantages:

- it is ~ 100 times faster;
- it can be done in situ, without removing the sensor from the detector;
- it can be repeated many times.

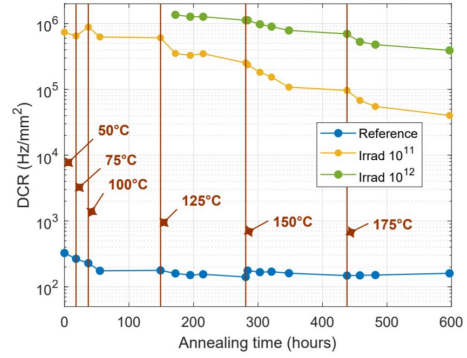
Consequently, the final design of the dRICH detector will probably include several online annealing phases and, at most, one big operation of sensors removing for long annealing in the oven.

4.3 The dual-radiator RICH prototype

A prototype [16] of the dRICH detector was built in Ferrara in the summer of 2021, aiming to test it during several test beams in the following years. On a lower scale, it reproduces the expected behavior of the entire dRICH detector. It was used to test the hadron separation capabilities that can be achieved. This section identifies the prototype using the acronym dRICH.

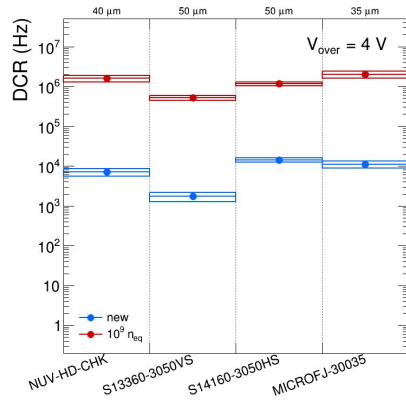


(a) Dark current of a SiPM as a function of the irradiation dose received. It increases linearly with the dose.

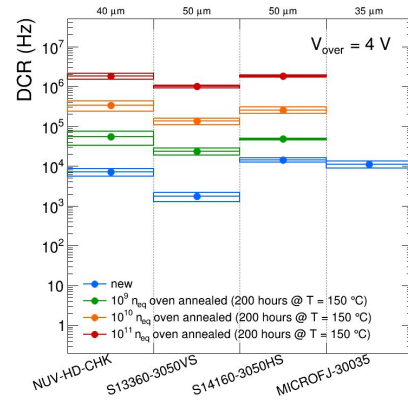


(b) Results of the first annealing test performed in the oven, showing decreased DCR. Moreover, it shows that most of the annealing effect occurs in the first tens of hours.

Figure 4.6: Effects of the irradiation and first annealing test.



(a) Dark count rate measured for different sensors when they were new and before the annealing).

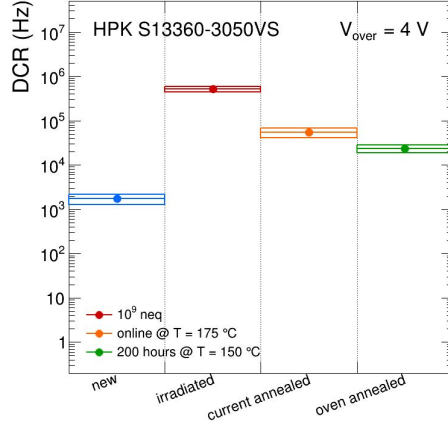


(b) Dark count rate measured for different sensors and different irradiation dose after 200 h of annealing at 150 °C.

Figure 4.7: Results of irradiation and annealing on different sensors.



(a) Picture of the thermal camera measuring the directly polarized SiPM. It can reach more than 175 °C.



(b) Comparison of the dark count rate measured for the same sensor kind of sensor applying the online (“current”) or the oven annealing.

Figure 4.8: Temperature control during the online annealing and results of the annealing performed through the direct polarization of the sensors.

4.3.1 Design

A scheme of the prototype is reported in Figure 4.9. A charged particle crossing the prototype starts passing through the aerogel ($n \simeq 1.02$), producing a Cherenkov-photon cone with an aperture of about 11°. The photons are reflected by a first spherical mirror and focused on the photon detector array. Then, the particle passes through the gas ($n \simeq 1.00085$), which fills the detector and produces a Cherenkov-photon cone with an aperture of about 2°. The first mirror has a central hole to allow the photons made in the gas at small angles to fly towards a second spherical mirror and be focused back on the same photon detector array. The information from the two imaged Cherenkov rings combined with the beam momentum will be used to identify pions, kaons, and protons in the momentum range from 3 GeV up to 50 GeV.

Mechanical structure

The dRICH is 1.3 m long and is composed of a 50 cm long cylinder with a 50 cm diameter and an 80 cm long extension with a 25 cm diameter. This volume is called the “gas chamber”, and the C_2F_6 fills it. It has to bear under and over-pressurization, allowing the change of air with the gaseous radiator and preserving light tightness, allowing the single-photon operation mode of photo-sensors. Moreover, it includes the mechanics of regulating the angle and position of the mirrors along the detector axis. The curvature radius

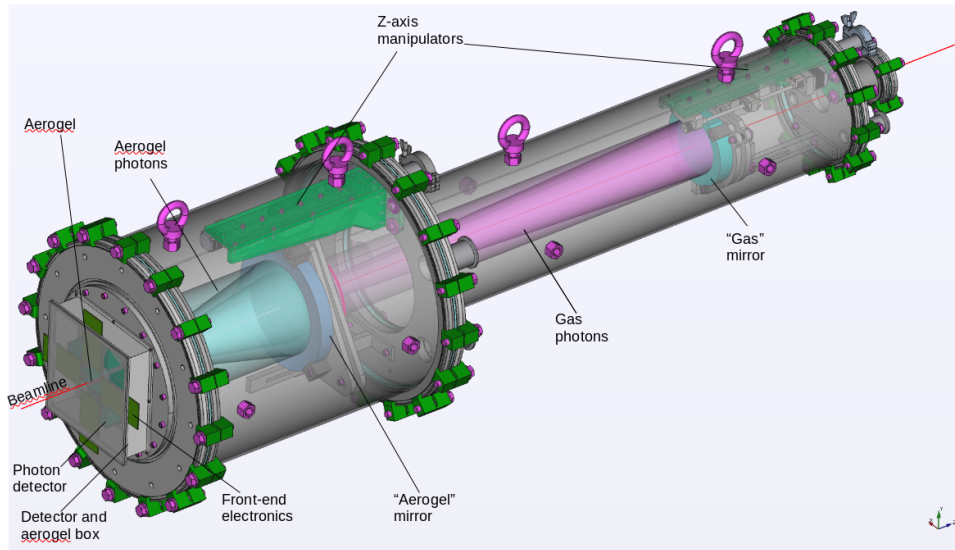


Figure 4.9: dRICH prototype scheme.

of each mirror was designed to put the focus at the same z coordinate of the photo-detector plane, allowing it to collect the light produced over the full length of the radiator and focus it to the same point. The mechanical structure that hosts each mirror can be aligned using three different screws and, without opening the detector, can be moved along the detector axis using an engine to have a fine regulation of the focus position. A series of pictures of the dRICH components is shown in Figure 4.10.

The aerogel container completes the mechanical structure. It is a 3D-printed black box containing the aerogel radiator placed upstream of the detector box on the beamline. Black rubber is used to seal the contact edge between the aerogel box and the aperture of the detector box, preserving it from light leaks. The box permits operation in the EIC configuration, a 4-cm-thick layer of aerogel, but also to test other configurations with 2-cm or 6-cm-thick layers of aerogel.

Detector box

In front of the prototype is the detector box, which hosts the photosensors with their sensitive faces directed forward. For the prototype, three different kinds of detector boxes were used:

- The MAPMT box hosts four Multi-Anode Photo-Multipliers Hamamatsu H12700 (the same as the CLAS12 RICH), used as reference detectors to study the prototype's performance.
- The MPPC box hosts three Multi-Pixel Photon Counters, matrices of SiPMs used during the first test beams as reference detectors to study

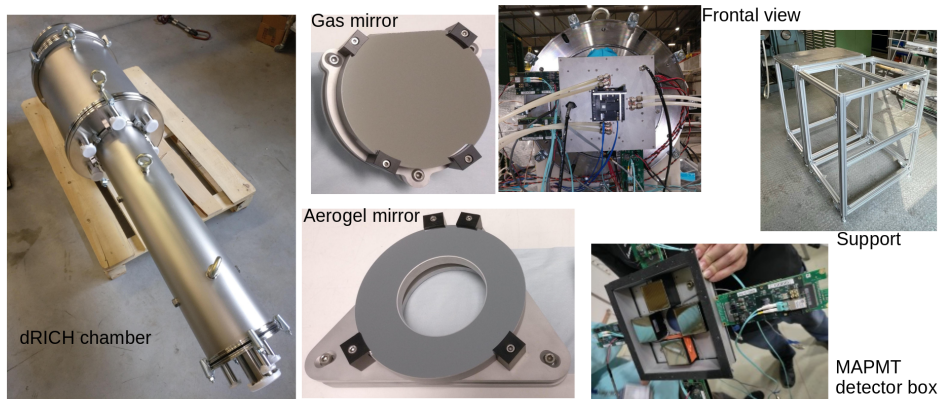
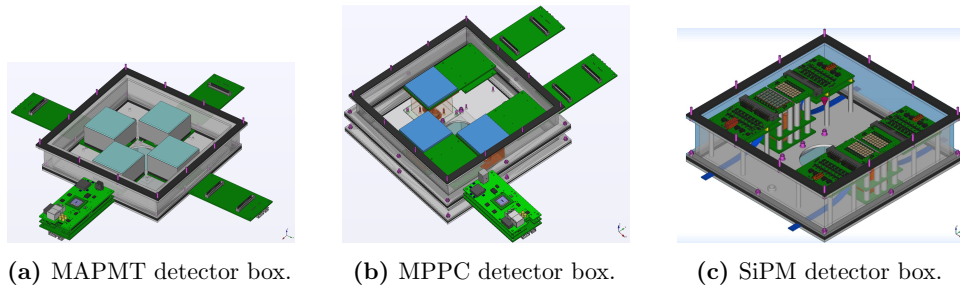


Figure 4.10: Collection of pictures of the prototype components



(a) MAPMT detector box. (b) MPPC detector box. (c) SiPM detector box.

Figure 4.11: Drawing of the three detector boxes.

the silicon-based sensors and their cooling system.

- The SiPM box hosts four matrices of Silicon Photo-Multipliers used to evaluate the most suitable sensor for the EIC full dRICH detector.

The detector boxes are represented in Figure 4.11. The data of MAPMT and MPPC detector boxes are acquired using the Multi-Anode ReadOut Chip (MAROC) as well as done for the CLAS12 RICH. Instead, for the SiPM detector box, a streaming readout system based on A Low Power Chip for Optical Sensor Readout (ALCOR) was tested. Initially, the SiPM box was designed to host four of the custom matrices used to study the annealing procedure. Then, in the last version, it was modified to host up to 8 readout units made following the current design for the final detector, covering almost the entire ring.

Radiators

The radiators are the C_2F_6 gas and the aerogel, with refractive index $\simeq 1.00085$ and $\simeq 1.02$, respectively. They present different challenges:

- C_2F_6 is a greenhouse gas, so its use is critical from the point of view of respecting the environment. For the prototype, the relatively small amount and the presence of a recovering system make it possible to use it. For the design of the final detector, solutions based on the use of pressurized not-greenhouse gases are being studied.
- Silica aerogel is a fragile material and not easy to handle, but in the group working on the dRICH, there are enough capabilities to do it. The main issue regards the aerogel producer because the most important in the world is the Budker and Boreskov Institute of Nuclear Physics (Russia); for example, they delivered the aerogel for the CLAS12 RICH. Then, the invasion of Ukraine introduced insurmountable complications in buying from them. At the moment of writing this document, the aerogel of the final detector will probably be provided by the Aerogel Factory Co. [18], a new large-scale producer that emerged in 2021 from Chiba University, Japan. They declare the capability of producing aerogel in a wide range of refractive index, between 1.003 to 1.18, which makes them a credible option for purchasing dRICH aerogel. Being not a unique method to produce aerogel, and its properties can be very different, even slightly changing the refractive index. This makes it necessary to conduct careful tests before deciding on the producer and characterizing each element.

This thesis deals with the resolution achieved for gas and aerogel, but more attention is paid to aerogel because the author was mainly involved in its study. To evaluate the aerogel produced by the Aerogel Factory Co., several samples were characterized in the laboratory of INFN Ferrara division and tested using the prototype at CERN.

4.3.2 Aerogel characterization

Table 4.1 reports a recap of the aerogel tiles studied. A Perkin Elmer UV/VIS spectrophotometer Lambda 365 was used to characterize the aerogel. The spectrophotometer measures the transmittance of the sample placed inside it as a function of the photon wavelength. The transmittance was analyzed using the extended Hunt formula [12]

$$T(\lambda) = e^{-\frac{t}{\Lambda_T}} = e^{-t\left(\frac{1}{\Lambda_A} + \frac{1}{\Lambda_S}\right)} = Ae^{-\frac{Bt}{\lambda^8}} e^{-\frac{Ct}{\lambda^4}} \quad (4.1)$$

where T is the transmittance, λ is the wavelength of the photon, $\Lambda_{A,S}$ are respectively the Absorption and Scattering length, and A, B , and C are the parameters. An example of fitted transmittance is reported in Figure 4.12. From this formula, it is possible to obtain the values of absorption and scattering length

$$\Lambda_S = \frac{\lambda^4}{C} \quad (4.2)$$

Tile ID	Producer	Production year	Refractive index		Side [mm]	Width [mm]
			Nominal	Measured		
TSA2-1a	Japanese	2021	1.020	1.0206	50	20.5
TSA1-2b	Japanese	2021	1.020	1.0206	50	20.8
TSA1-3b	Japanese	2021	1.020	1.0199	50	20.8
TSA2-4a	Japanese	2021	1.020	1.0204	50	20.8
TSA3-1a	Japanese	2021	1.030	1.0301	90	21.1
TSA3-2a	Japanese	2021	1.030	1.0303	90	21.0
TSA3-3a	Japanese	2021	1.030	1.0304	90	21.3
TSA3-3b	Japanese	2021	1.030	1.0304	90	21.1
AG22J001	Japanese	2022	1.020	1.0210	50	20.5
AG22J002	Japanese	2022	1.020	1.0201	50	20.6
AG22J003	Japanese	2022	1.020	1.0207	50	20.4
AG22J004	Japanese	2022	1.020	1.0218	50	19.5
AG22J005	Japanese	2022	1.015	1.0152	50	19.9
AG22J006	Japanese	2022	1.015	1.0158	50	21.7
AG22J007	Japanese	2022	1.015	1.0158	50	21.4
AG22J008	Japanese	2022	1.015	1.0158	50	21.4
AG22J009	Japanese	2022	1.024	1.0260	50	21.3
AG22J010	Japanese	2022	1.024	1.0261	50	21.2
AG22J011	Japanese	2022	1.024	1.0232	50	19.1
AG22J012	Japanese	2022	1.024	1.0232	50	19.4
AG22J013	Japanese	2022	1.020	1.0205	110	20.3
AG22J014	Japanese	2022	1.020	1.0208	110	20.3
AG22J015	Japanese	2022	1.020	1.0208	110	20.4
AG22J016	Japanese	2022	1.020	1.0207	110	19.7

Table 4.1: Recap of the aerogel tiles tested using the prototype. The values of the measured refractive index were provided by the producer. If the ID reported is **bold**, the correspondent tile was used to form the 4-cm-thick layer of aerogel in the prototype measurement.

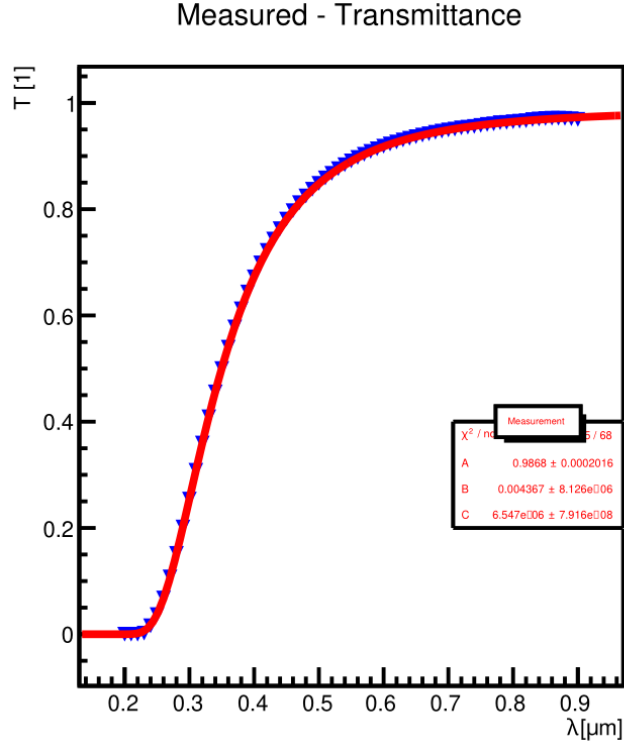


Figure 4.12: Measured transmittance (blue arrows) fitted using the extended Hunt formula (red).

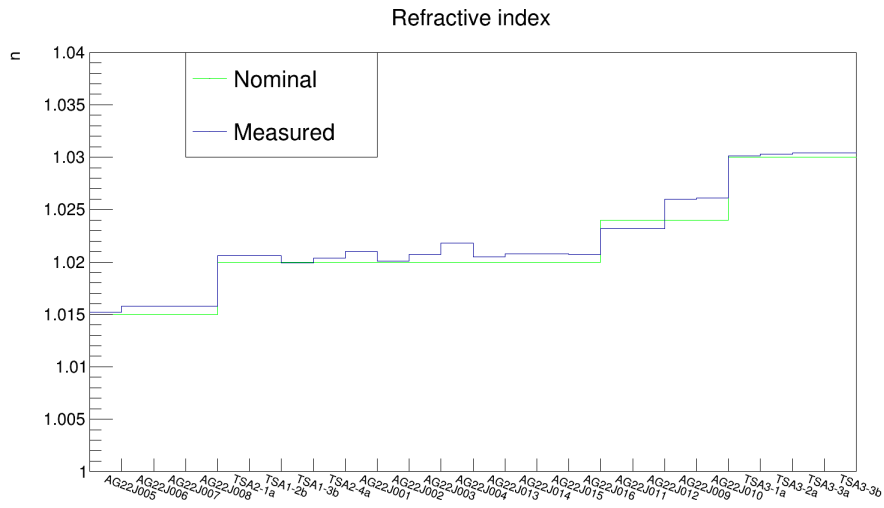
and

$$\Lambda_A = \frac{\lambda^8 t}{Bt - \lambda \cdot \ln A} \quad (4.3)$$

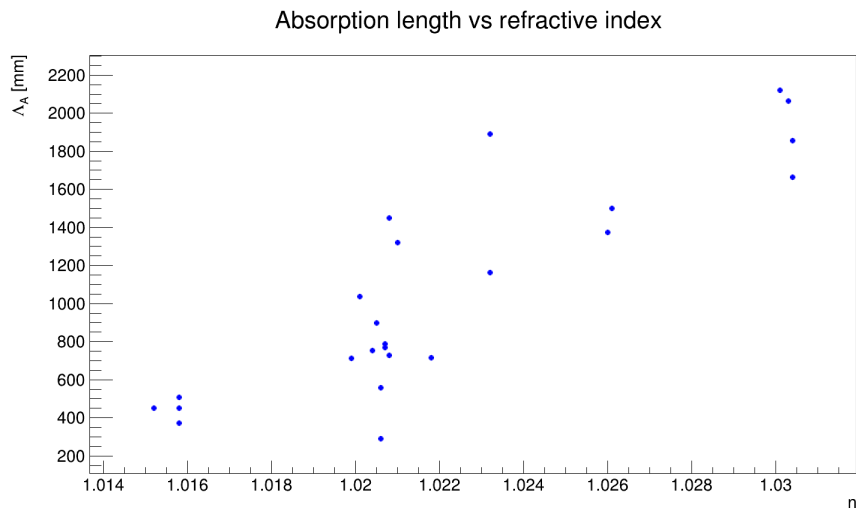
The total transmission length is defined as

$$\frac{1}{\Lambda_T} = \frac{1}{\Lambda_A} + \frac{1}{\Lambda_S} \quad (4.4)$$

The main results are shown in Figures 4.13 and 4.14. The first plots report the tiles' nominal and measured refractive index; both were provided by the producer (and the precise numerical values are reported in Table 4.1). The second shows the absorption length, which is not uniform for different tiles with the same refractive index. This fact can be neglected because the absorption length is at least one order of magnitude larger than the scattering length, and then it has a second-order effect on the total transmission length. The last two plots describe the scattering and total transmission length, showing an almost linear correlation with the refractive index. This relation implies that aerogel with a larger refractive index will have a larger yield of photons, permitting a lower single-particle resolution.

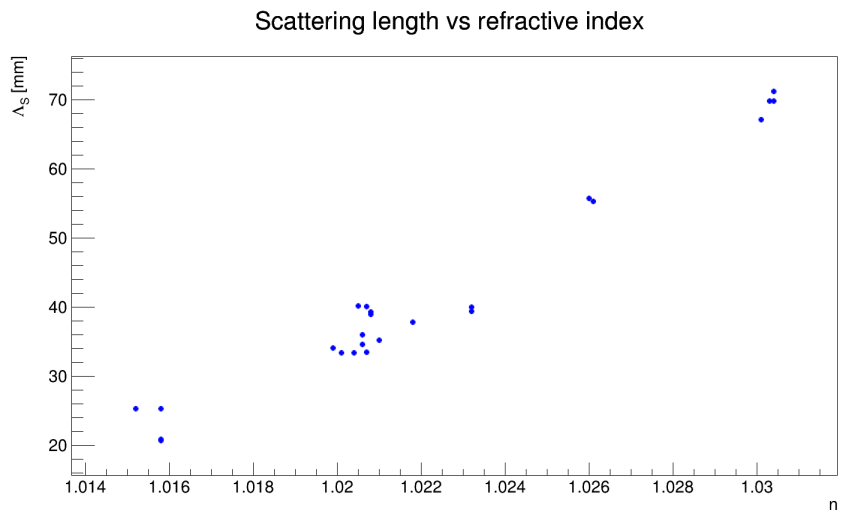


(a) Refractive index of the aerogel tiles.

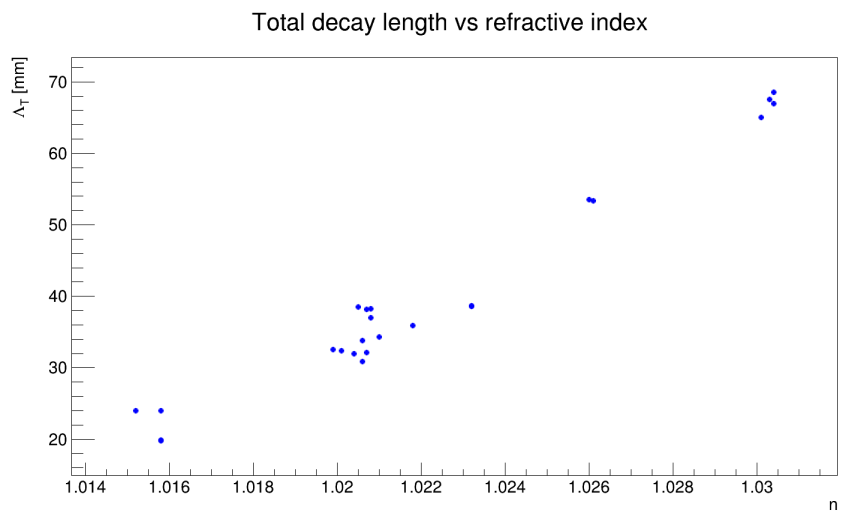


(b) Absorption length of the aerogel tiles versus the refractive index.

Figure 4.13: Aerogel tiles characterization plots 1



(a) Scattering length of the aerogel tiles versus the refractive index.



(b) Total transmission length of the aerogel tiles versus the refractive index.

Figure 4.14: Aerogel tiles characterization plots 2.

Not all the tiles characterized can be studied with this prototype. Indeed, the aperture of the Cherenkov cone produced by tiles with $n = 1.03$ is larger than the border of the mirror, and the photons are not reflected to the photo-detector. Then, the aerogel study is upper limited to $n = 1.026$, and tiles with larger refractive index could be tested with the next prototype. The characterization results are used in the process of selecting the most uniform aerogel tiles to test them into the prototype, which is designed to work in the EIC configuration with a 4-cm-thick aerogel layer, corresponding to two stacked tiles. The final selection was based on the uniformity of the refractive index and maximizing the total transmission length. These conditions led to the definition of a pair of tiles of each nominal refractive index used during the test beams with the prototype. The identifier of the selected tiles is reported in bold characters in Table 4.1.

4.3.3 Simulation

A simulation was developed using GEant4 Monte-Carlo (GEMC) [8][17], a framework dedicated to the simulation of low and medium-energy particle physics, to evaluate the performance of the prototype. A relatively simple model of the prototype was implemented using CAD drawings of the main elements and textual implementation of their physical properties of reflection (mirrors), refractive index, and total transmission length (aerogel and gas). The photo-detectors were simulated as a solid plane absorbing all the photons in a thin thickness; the physics effects of quantum efficiency and pixelation were applied during the analysis. The drawings of the model are shown in Figure 4.15. In addition to the main components of the dRICH, the simulation model includes two objects representing the GEM detectors composing the tracking system at the test beams. This model was used during the design phase to establish the value of some important parameters, like the curvature radius of the mirrors, and to evaluate the expected resolution achievable with the prototype. The software was adapted to produce simulation data in a format compatible with the same analysis software used for the test beams data, so the same analysis chain is used. However, this simulation does not perfectly reproduce the prototype; for example, the simulated beam was punctiform and divergence-less, or the background was negligible with respect to the real case. For this reason, the results are also compared with the single photon resolution values provided by the simulation group of the full detector: 1 mRad for the gas Cherenkov angle and 3 mRad for the aerogel one.

4.3.4 Test beams

The prototype was tested in several test beams at the European Council for Nuclear Research (CERN) between 2021 and 2023 using the experimental

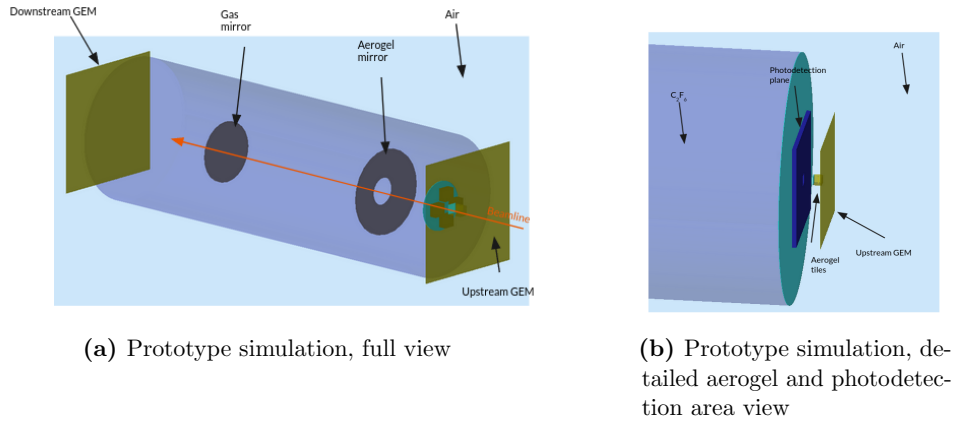


Figure 4.15: Prototype simulation draws.

halls available at Proton Synchrotron (PS) and Super Proton Synchrotron (SPS), accelerators providing beams of charged mixed hadrons, respectively, with momentum up to 12 GeV and up to 200 GeV. Aiming the dRICH to distinguish particles with momentum up to 50 GeV and having the aerogel a refractive index larger than the C_2F_6 one, the test beams goals were:

- at PS to perform studies on several aerogel tiles with different refractive index and stack compositions, applying wavelength filters and exploiting the Cherenkov threshold detectors of the beam to identify particles of different species with the dRICH.
- At SPS, measure the resolution achievable with a high-momentum beam that saturates the two rings for each particle species and identifies different particle species using the gas and the beam PID system.

During the first test beams, the SiPM detector box was used mainly to operate the photosensors, their cooling system, and the data acquisition chain. In the 2023 Fall test beam, the latest version of the SiPM detector box, represented in Figure 4.16a, allows the first almost complete double-ring of photons to be obtained, as shown in Figure 4.16b.

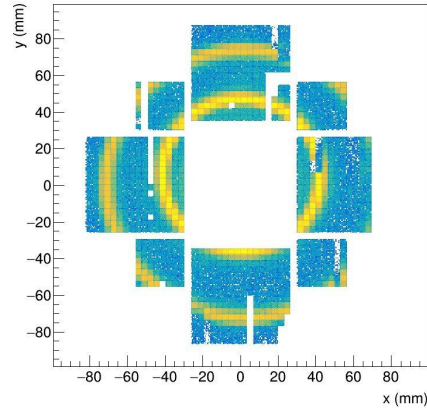
The MAPMT detector box was used during all the test beams to measure the prototype's performance and the achievable resolution of aerogel and gas Cherenkov angles. The following sections will present the analysis developed and the results obtained.

Experimental setup

The test beam setup included a tracking system, a trigger apparatus, and an external PID detector; a picture of this is shown in Figure 4.17. The tracking is based on two Gas Electron Multiplier (GEM) detectors placed upstream



(a) Picture of the photo-detector side of the SiPM detector box.



(b) The two rings obtained in the last test beam using the SiPM detector box.

Figure 4.16: The latest version of the SiPM detector box includes 4 readout units with 256 sensors and 4 readout units with 64 sensors. It allows the detection of almost the whole two rings, both from aerogel and gas.

and downstream of the dRICH. The GEM detects the position in which the beam crossed it, and the coincidence of the signals from the two detectors is used to find the track of the particle with a resolution better than $100\ \mu\text{m}$. The GEMs were a smaller version of those described in the Reference [4]. The GEMs had their power supplies providing high ($\sim 4\ \text{kV}$) and low voltage, front-end boards, and data acquisition software; the author developed his expertise on operating the tracking system and became the expert-on-call since the 2022 test beams.

The trigger system was based on four scintillators measuring $2 \times 1\ \text{cm}^2$ each, two placed in front of the aerogel box and two just downstream of the prototype, and read with SiPMs. The components of each pair of scintillators work in coincidence to avoid random triggers. The logical AND and OR of the scintillator pairs were available for the trigger and could be selected from the control room without accessing the experimental hall. The tracking signal was added in logical AND to the trigger to pair the track with the corresponding event detected by the prototype.

Figure 4.18 reports the plots relative to the tracking system from two runs acquired at the two accelerators, showing clear differences. The beam profile and the divergence of the SPS beam are smaller than the PS beam. At PS, the coincidence with the trigger scintillators is also used to limit the beam profile, which could also be larger than the one shown in Figure 4.18b; instead, at SPS, the beam spot is smaller than the area covered by the trigger system.

The test beam setup included an external PID apparatus consisting of two (at PS) or three (at SPS) gaseous threshold Cherenkov detectors. They

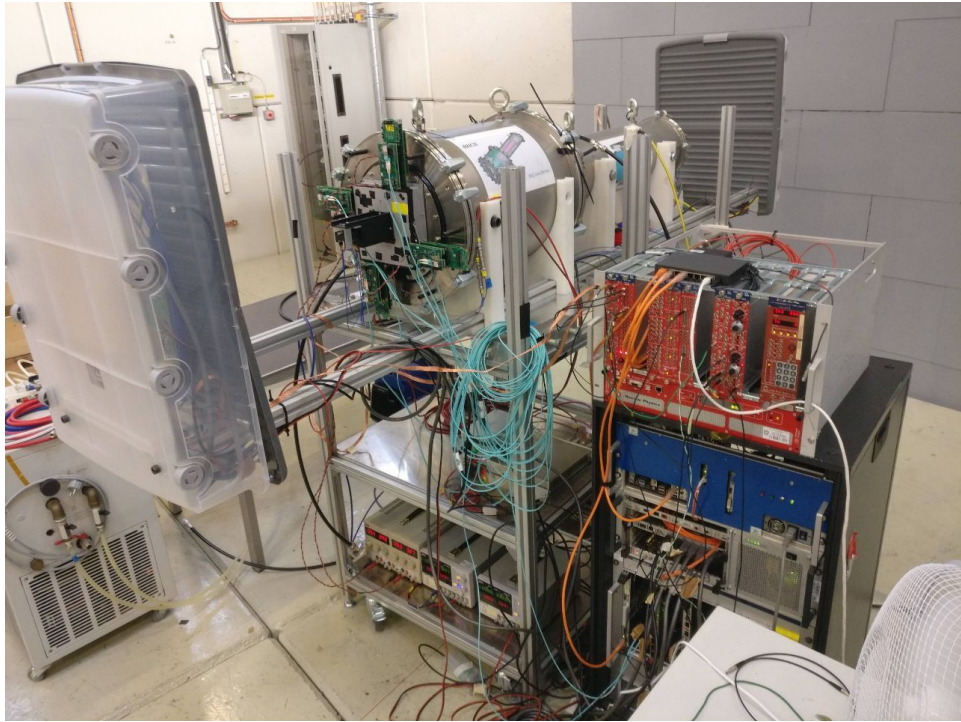
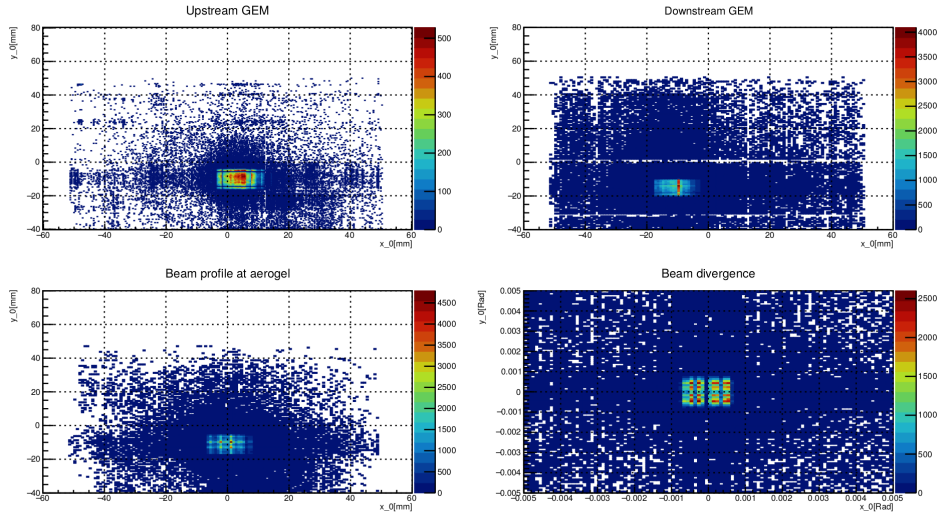
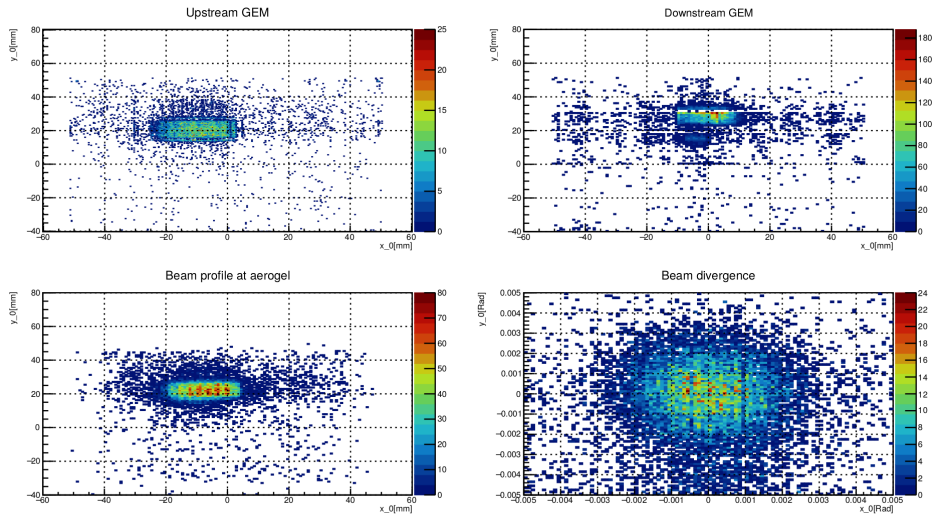


Figure 4.17: Experimental setup of the 2023 test beam at PS. The beam income from the left side. From the left to the right of the picture, it is possible to find the upstream GEM, inserted in the safety box to mitigate the high-voltage risk; the mechanical structure sustaining the detector, which is adjustable in height and inclination; the aerogel container, that is the small black box 3D-printed; the MAPMT box, in the “Corner” configuration as deductible from the position of the electronic boards; the cylinders constituting the dRICH, which are filled of C_2F_6 ; the light blue optical fibers, for the communication of the MAROC readout with the storage; the power supplies, both for the readout electronic and for the tracking; the black pipe of the gas distribution system; the electronics boards handling and merging the tracking and trigger and beam Cherenkov signals; and finally the downstream GEM, placed also in the safety box. The beam Cherenkov detectors are placed upstream of the prototype and are not visible.



(a) The tracking plots for one run at SPS. The top plots show the beam profile in the two gems; the bottom plots show the extrapolated beam profile at the aerogel position and the divergence of the beam.



(b) The tracking plots for one run at PS. The top plots show the beam profile in the two gems; the bottom plots show the extrapolated beam profile at the aerogel position and the divergence of the beam.

Figure 4.18: Comparing the top and bottom plots, it is visible that the beam spot at SPS is smaller rather than at PS, and also it is smaller than the trigger $20 \times 10 \text{ mm}^2$, although the signal is noisier. Moreover, the divergence of the SPS beam is less than half in radius of the PS.

can host various gases and set the inner pressure, modifying the refractive index. This procedure permits setting a threshold for the mass of the particles producing the Cherenkov photons for a given beam momentum. Particles lighter than the threshold will produce light inside the detector, while heavier particles will not. Combining the information from various detectors with different settings makes it possible to tag different species of particles. For example, a detector activation scheme for the PS is reported in Table 4.2. The signals provided by the trigger signal and the beam Cherenkov were

Particle	Threshold $\leq m_K$	Threshold $\leq m_p$
π	✓	✓
K	✗	✓
p	✗	✗

Table 4.2: It reports if the beam Cherenkov detector produces an output signal for the threshold given in the first line. The combined information permits the identification of the hadron passing the detector.

read using a special adapter board coupling them to the MAROC, the same readout of the MAPMT. This allowed us to handle them easily with the same data acquisition software as the photo-detector.

The MAPMT box design supports two different configurations, called “Cross”, with the projection of the photo-detectors placed close to the side of the aerogel tile, and “Corner”, with the photo-detectors placed in the corner of the aerogel tile. The two options were designed because the MAPMTs in the Cross configuration cover almost the whole gas ring but only $\sim 40\%$ of the aerogel ring; moreover, the aerogel ring is close to the external edge of the photodetection area for the refractive index expected from the experiment original design ($n = 1.020$). The Corner configuration permits covering the rest of the aerogel ring and the study of aerogel with a larger refractive index (1.023, 1.026) characterized by better transparency properties. The plots of the rings acquired in Cross and Corner configurations are visible in Figure 4.19.

Data analysis

The author wrote the data analysis software in C++, using the data analysis framework ROOT by CERN. The software is based on modular logic, so new information can be added at each step, allowing access to them along the entire analysis chain. It was designed this way because the software has been developed over the years, starting from the first test beams in 2021, making it easier to introduce modifications. The software performs the following operations:

- Reconstruction of the hits by coupling falling and rising edges and applying time calibration.

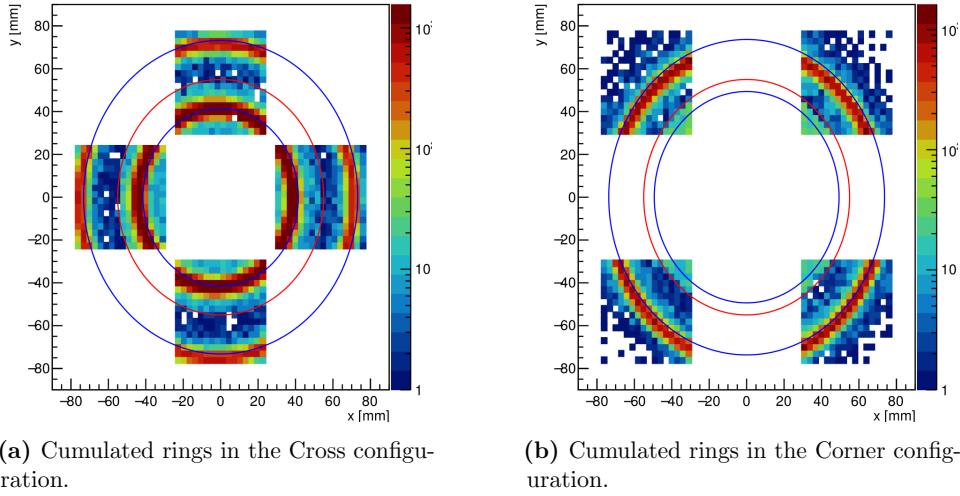


Figure 4.19: The two configurations of the MAPMT detector box. On the left, the two rings produced in gas and aerogel are visible. On the right, the ring produced by the aerogel is in the center of the photo-detectors and well defined than the other configuration. The blue circles are the ring reconstructed during the analysis for gas (inner) and aerogel photons (outer), and the red one is the geometrical selection that is part of the photon assignment to the right ring.

- Selection of real photons based on the hit duration.
- Distinction of the photons produced in aerogel and gas based on their time-of-flight and a geometrical cut on the radius.
- Selection of ring photons using the coincidence technique.
- Computation and application of a primary correction of photon position for small misalignments of the mirrors, computing a new mean center for each run based on the average of the hit position.
- If the tracking information is available, computation and application of a secondary correction of the position of each photon based on the misalignment of the mother particle from the center of the beamline.
- Averaging over the photon associated with the particle, computation of the mean Cherenkov angle and time.
- Computation of the single-photon resolution, single-particle resolution, and its relation with the number of photons detected.
- When the beam Cherenkov detectors are available, computation of the same results for particle species.

The assignment of photons to the ring is carried out in two steps. A preliminary distinction is based on a geometrical selection by defining “gas

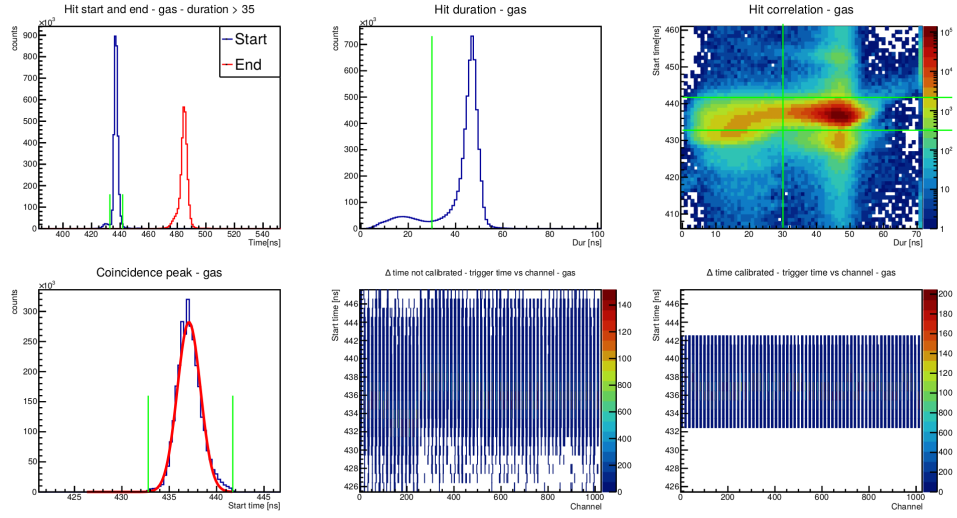


Figure 4.20: Plots summarizing the analysis operation to identify and assign the photon to the rings, for gas in this case.

photons” as those with a radius lower than 55 mm and “aerogel photons” as the others. This permits the identification of two time-coincidence peaks, with a detectable difference of ~ 7 ns; the standard deviation of both peaks is ~ 1.2 ns. Then, belonging to the time-coincidence peak became the main criterion for assigning the photons to the right ring. Figure 4.20 summarizes the operation performed by the software on the hit. It includes the distribution of the start and end timing of the hit, the hit duration with the green line representing the relative selection to exclude the secondary shorter signals generated by cross-talk, the coincidence peak of photons belonging to the gas ring, and the effect of the time calibration.

The main condition to be satisfied to consider a ring good is that it includes at least 3 photons. A second selection is based on the misalignment of the track from the beamline, which is defined as the trajectory misalignment with respect to the line connecting the center of the beam spot in the two GEMs. This is not a squeezing condition because the correction developed reduces the effect of misalignment. In any case, incident particles with a polar angle larger than 2 mRad are erased from the sample.

The primary correction on photon position was developed to compensate for small misalignment of the mirrors with respect to the detector axis. The correction starts from the computation of the mean center of the event, obtained by averaging the x coordinate of all the photons hitting the two MAPMTs placed along the horizontal axis and averaging the y coordinate of all the photons hitting the two MAPMTs placed along the vertical axis of the detector box. This operation is made separately for gas and aerogel rings because the mirrors are not coupled so they can affect the photon direction

differently. Then, the mean center is defined as the origin of a new coordinate system, and the position of the photons is shifted accordingly.

The event-for-event correction based on the particle track misalignment with respect to the beam center was developed after the first test beam when a correlation between the half-difference between a coordinate and the correspondent projection of the polar angle was noted. This permits the definition of a specific center for the ring associated with the particle, constituted by the new center defined by the main correction plus the projection of the misalignment. The effect of the two corrections can be neglected, reducing the resolution by up to one-third.

The output of the analysis of data acquired using a beam of 120 GeV, on which both the aerogel and gas rings are saturated, is considered to explain the output of the analysis. In Figure 4.21, the first plot shows the distribution of the single-particle Cherenkov angle, the mean time-of-flight of the photons associated with the particle, and the distribution of the number of photons for the particle. The first of these three plots is fitted with a Gaussian, whose mean value is the Cherenkov angle associated with the particle, and the standard deviation is the resolution. Comparing the first and the second line plots, it is possible to note the differences between the gas (on top) and the aerogel (bottom) rings. The other output plots produced by the analysis are shown in Figure 4.22. The left ones are the distribution of the Cherenkov angle of each photon associated with the ring for gas (on top) and aerogel (bottom), fitted again using a Gaussian function on which the mean corresponds to the Cherenkov angle and the standard deviation with the single photon resolution. The right ones show the single particle resolution as a function of the number of photons associated with the ring. This graph is fitted with the function

$$\sigma_{sing_part}(n_\gamma) = \sqrt{\frac{p_0^2}{n_\gamma} + p_1^2} \quad (4.5)$$

where parameter p_0 represents the single photon resolution, the best resolution achievable with only one photon, and p_1 is the asymptotic single particle resolution, the minimum achievable in an ideal situation of detecting infinite photons for a ring.

4.4 Results of the prototype studies

In this section, the measured performances of the prototype are reported and compared with the expected values provided by the simulation.

4.4.1 Resolution expected and achieved

The simulation described in section 4.3.3 is the newest version of the prototype simulation. It has been described because of its importance in the design

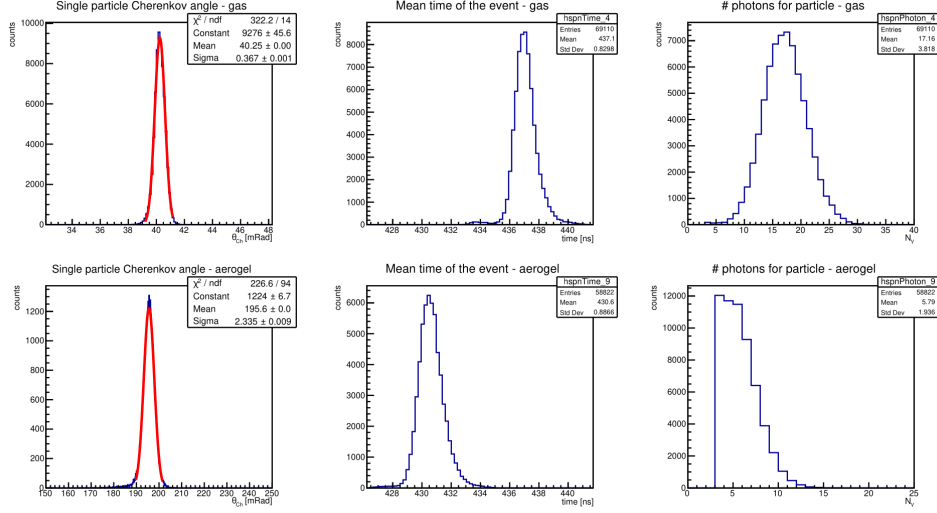


Figure 4.21: Example of the results of the analysis, for a 120 GeV of mixed hadrons. From left to right: the distribution of single-particle mean Cherenkov angle, the distribution of the mean time-of-flight of photons, and the distribution of the number of photons for particle. In the top line are the plots for gas, and at the bottom are the plots for aerogel.

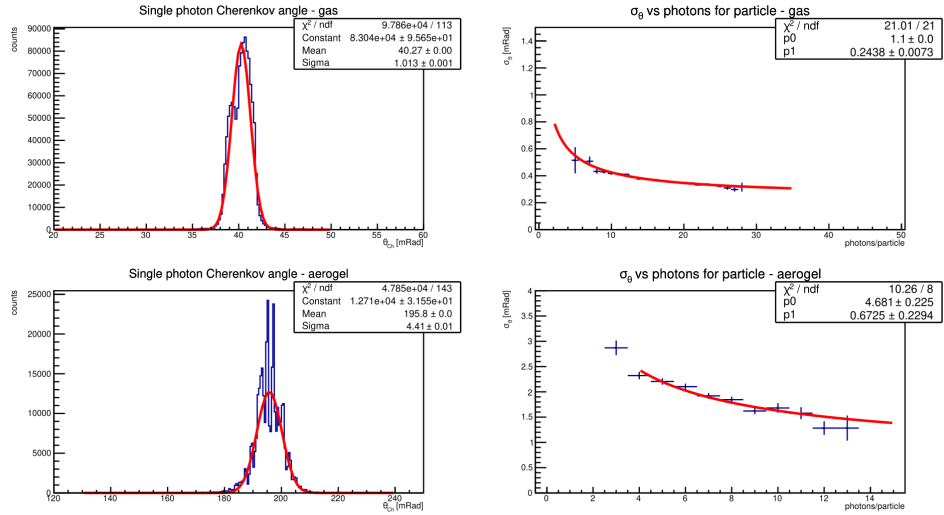


Figure 4.22: Example of the results of the analysis, for a 120 GeV of mixed hadrons. From left to right: the distribution of single-photon Cherenkov angle and the scatter plot of the single-particle resolution vs the number of photons. In the top line are the plots for gas, and at the bottom are the plots for aerogel.

phase and because the author developed it. Despite being the last version, it is optimistic and reproduces the prototype only partially. This implies that the simulation's resolution is better than the prototype's truly achievable. The results of the prototype simulation are described and were used in the first evaluation of the prototype. However, the results for the single photon resolution achievable obtained by the full detector simulation group are considered to be the real goal of the prototype. In particular, the expected single photon resolution they provided for gas and aerogel are 1 mRad and 3 mRad, respectively.

The simulation used a 120 GeV π^+ beam, a momentum value for which the aerogel and gas rings are both saturated. The results of the simulation are shown in Figure 4.23 and Figure 4.24.

The results for gas were obtained using a 120 GeV beam of positive mixed hadrons; for this momentum value, the gas ring is saturated independently from the particle species. The plots are shown in Figure 4.25 and Figure 4.26.

The results for aerogel were extracted from data acquired with a 12 GeV beam of negative mixed hadrons, on which the pion component was dominant over kaon and antiproton. The aerogel sample with the best results has a refractive index of $n = 1.026$. The data were acquired using the MAPMT box in the Corner configuration. The plots are shown in Figure 4.27 and Figure 4.28.

The numerical results are summarized in Table 4.3. It shows that the prototype performance satisfies the expectations both for gas and aerogel. The gas SPE resolution of 1.1 mRad has been obtained since the 2022 test beam, and further developments will be studied with the new prototype, which is also designed to test non-greenhouse pressurized gas. For the aerogel ring, the best SPE resolution obtained from the 2022 test beams was about 4.5 mRad, 1.5 times the expected value of 3 mRad. The study performed in the 2023 test beam, described in the following, permits achieving of a SPE resolution of 3.3 mRad, which is closer to the goal.

Future developments of the reconstruction software, for example, by implementing a ray-tracing algorithm to reconstruct the ring, will allow further refinements of the difference between measurement and simulation.

4.4.2 Aerogel study with the prototype

The goal of the August 2023 test beam was to deeply study the aerogel resolution, having performed the tiles characterization described in section 4.3.2. Using the aerogel from the Aerogel Factory Co. reported in Table 4.1 and the two configurations of MAPMTs, data were acquired for refractive index between $n_{min} 1.016$ and $n_{max} = 1.026$. Figure 4.29 shows the measured single photon and single particle resolutions. From both plots, it is possible to see that by increasing the refractive index, the resolution became smaller;

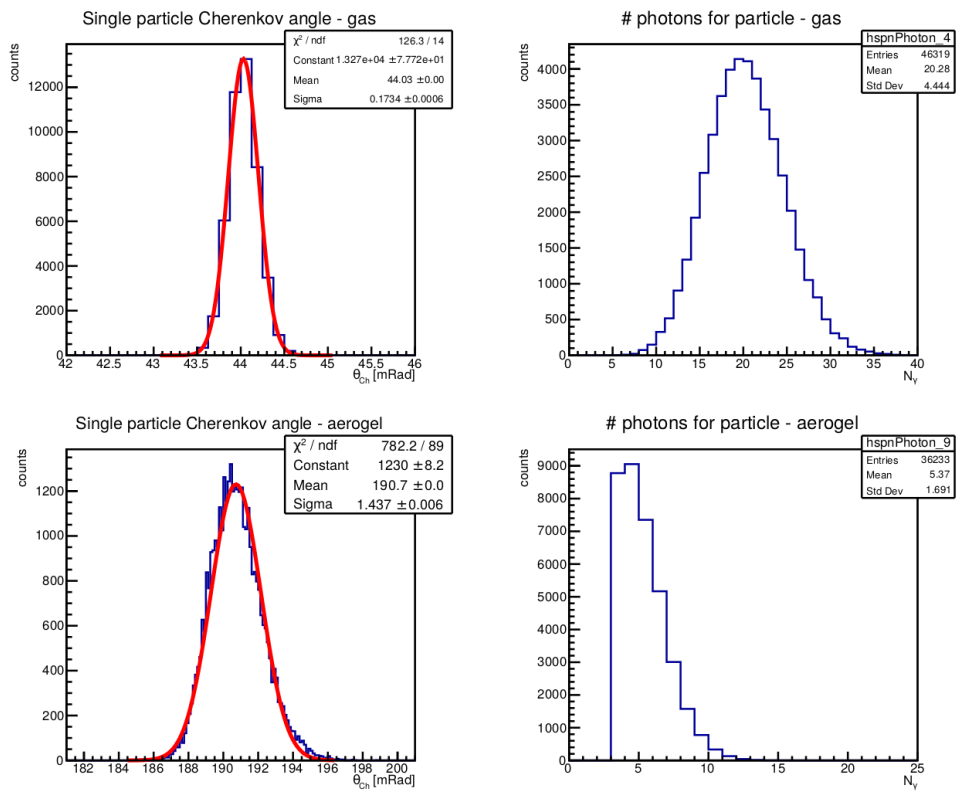


Figure 4.23: Simulation results. From left to right: the single particle Cherenkov angle, the mean time of the photons associated with the particle, and the number of photons detected. On top are plots for the gas ring, and on the bottom are plots for the aerogel ring.

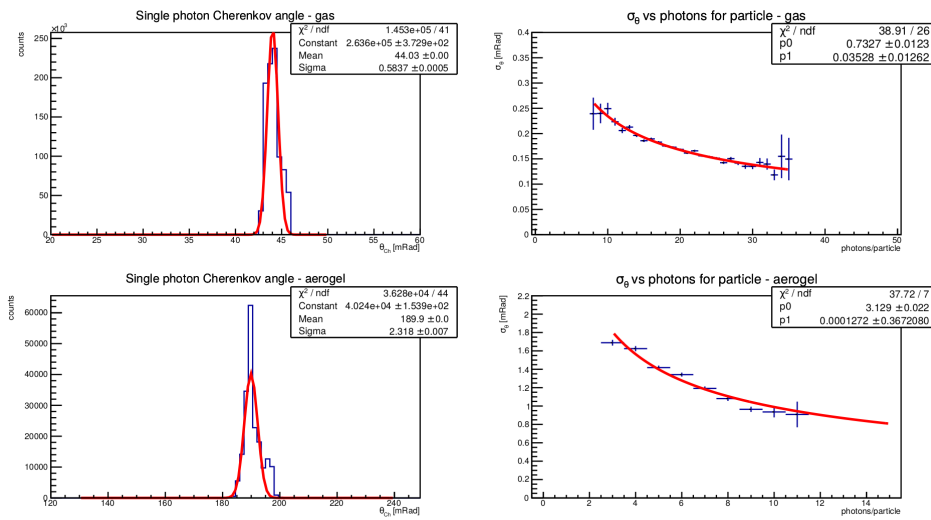


Figure 4.24: Simulation results. From left to right: the single photon Cherenkov Angle and the single particle resolution as a function of the number of photons. On top are plots for the gas ring, and on the bottom are plots for the aerogel ring.

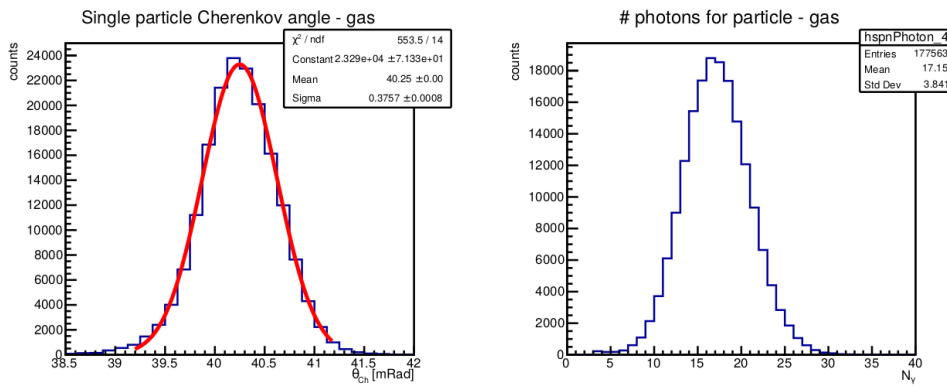


Figure 4.25: Plot of the results for gas. From left to right: the single particle Cherenkov angle, the mean time of the photons associated with the particle, and the number of photons detected.

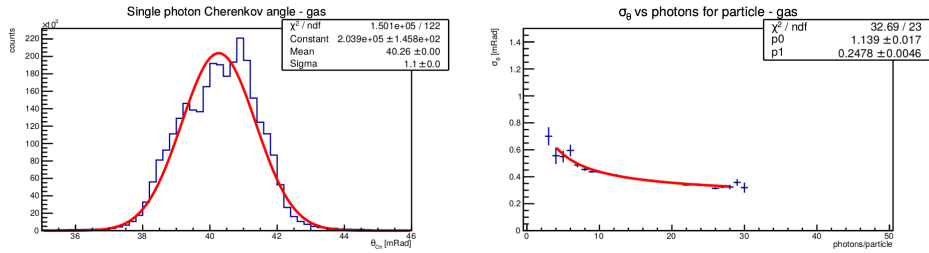


Figure 4.26: Plot of the results for gas. From left to right: the single photon Cherenkov Angle and the single particle resolution as a function of the number of photons. On top are plots for the gas ring, and on the bottom are plots for the aerogel ring.

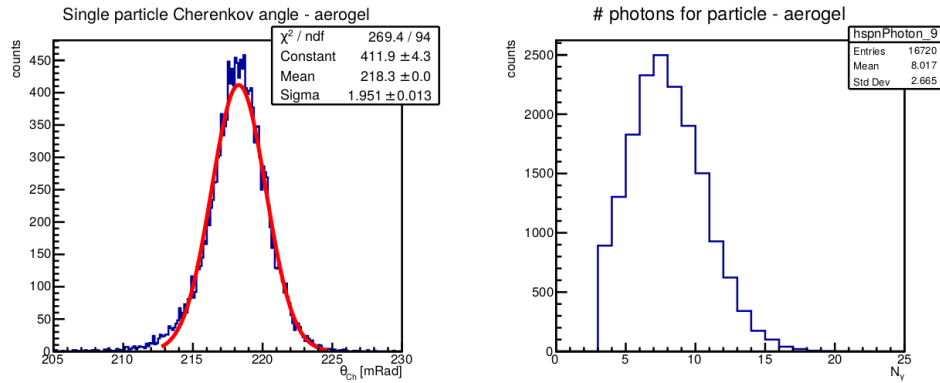


Figure 4.27: Plot of the results for aerogel. From left to right: the single particle Cherenkov angle, the mean time of the photons associated with the particle, and the number of photons detected.

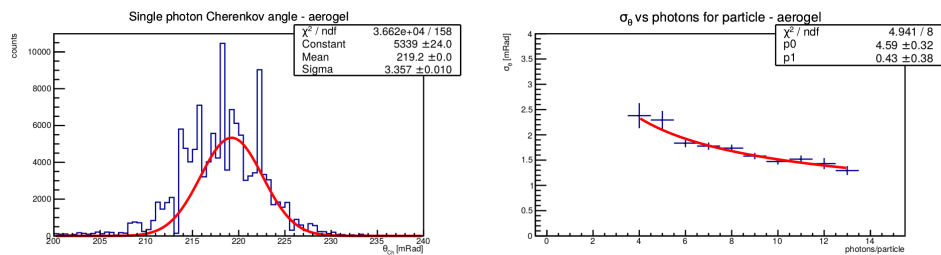


Figure 4.28: Plot of the results for aerogel. From left to right: the single photon Cherenkov Angle and the single particle resolution as a function of the number of photons. On top are plots for the gas ring, and on the bottom are plots for the aerogel ring.

Summary table of the prototype performance						
Source	SPE σ [mRad]	Single-particle σ [mRad]	Photons/particle	p_0 [mRad]	p_1 [mRad]	
Gas						
Simulation	$0.5837 \pm 0.0005 / 1$	0.1734 ± 0.0006	20 ± 4	0.733 ± 0.012	0.035 ± 0.012	
Data	1.1 ± 0.0	0.3757 ± 0.0008	17 ± 4	1.14 ± 0.02	0.248 ± 0.005	
Aerogel						
Simulation	$2.318 \pm 0.0007 / 3$	1.437 ± 0.006	5.4 ± 1.7	3.13 ± 0.02	0.0 ± 0.4	
Data	3.357 ± 0.010	1.951 ± 0.013	8 ± 3	4.6 ± 0.3	0.4 ± 0.4	

Table 4.3: Table summarizing the performance of the prototype. The error reported is the statistical error provided by ROOT for quantities extracted by a fit and the standard deviation for the number of photons. The Single PhotoElectron (SPE) column includes two values: the former is obtained from the prototype simulation, and the full detector simulation group provided the latter.

in particular, for $n = 1.026$, the $\text{SPE} = 3.3 \text{ mRad}$, which is the best result achieved. Figure 4.30a shows the number of photons for particle detected by the prototype as a function of the refractive index; as hypothesized from the increasing of Λ_T , aerogel with larger refractive index yields more photons. Figure 4.30b completes the results of this study, showing the measured Cherenkov angle that grows with the increase of the refractive index. This study showed that aerogel with a larger refractive index provides more defined rings. This result led to giving input to the full detector simulation group to evaluate the impact of increasing the aerogel refractive index.

4.4.3 Studies using the beam PID system

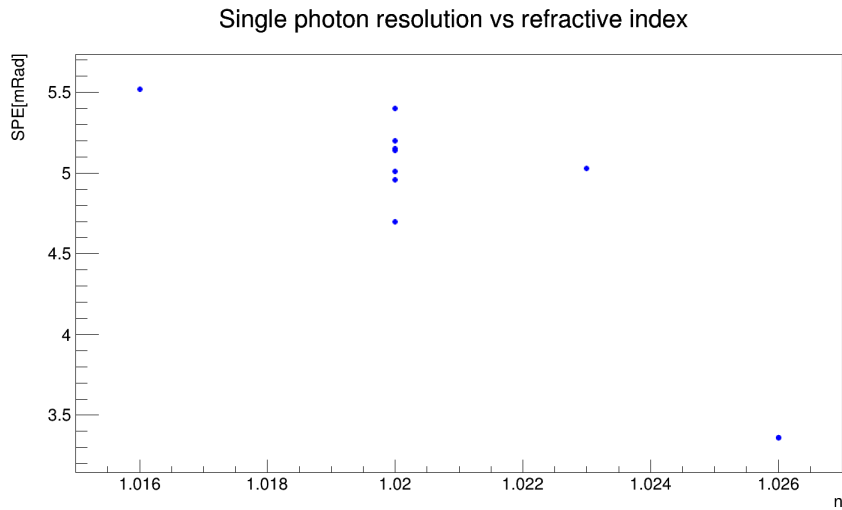
The beam PID system described in section 4.3.4 permits the identification of the hadron passing through the detector with good efficiency and then the study of the Cherenkov angle measured by the dRICH. For the gas component, this study used a beam of positive mixed hadrons with a momentum of 20 GeV and momentum of 50 GeV, covering the range on which the identification is based on that radiator. Most of the beam is constituted by pions, then the protons; although the kaons are a few percent, they are detected by the prototype. The single-particle Cherenkov angle distribution is shown in Figure 4.31 and Figure 4.32. In the former, the kaon peak is separate from the pion one. The proton peak appears in the latter, while the kaon starts to overlap with the pion peak. In both cases, a small inefficiency of the beam PID system is visible but does not affect the result.

The aerogel component was studied using beams of mixed positive hadrons with 6, 8, and 10 GeV momentum. The plots are reported in Figure 4.33, Figure 4.34, and Figure 4.35. In this case, the beam Cherenkov had more inefficiencies, but the peaks of the three species are still visible. These data were acquired with the $n = 1.026$ aerogel, then with the MAPMTs in the Corner configuration, then any information from the gas was lost. Comparing the three plots, the modification of the beam composition while energy grows is also visible: the proton components became mainly at 10 GeV.

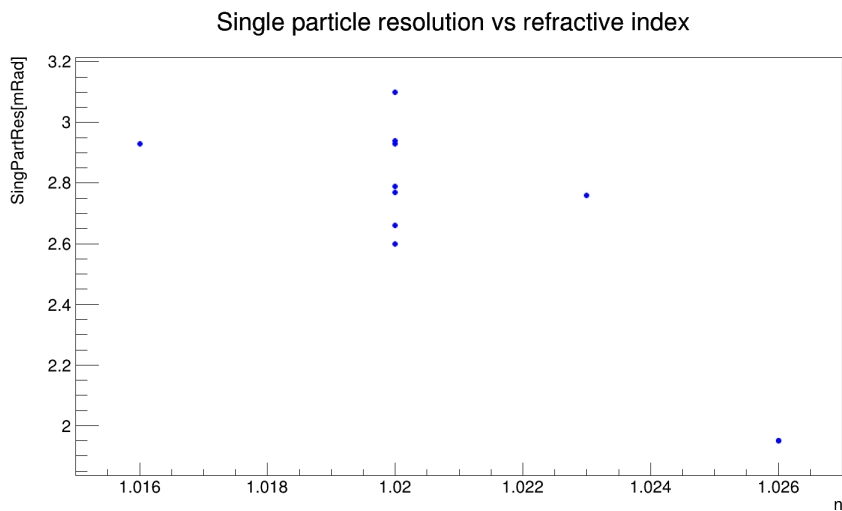
These results confirm the capability of the prototype to detect and identify different particles

4.5 Conclusions

The Electron-Ion Collider will be the machine to expand the frontiers of the known Quantum Chromodynamics. Colliding high momentum and highly polarized beams with a high luminosity will produce data, allowing us to understand the nuclear structure further. This can also be done by studying SIDIS, which requires the detection of at least one hadron in the final state. The particle identification in the hadronic endcap of the ePIC experiment will be carried out by a dual-radiator Ring Imaging Cherenkov detector. The

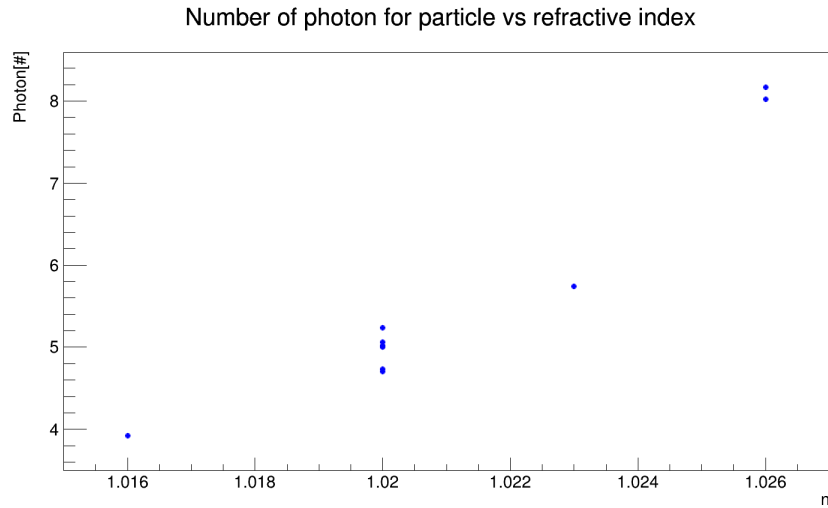


(a) Single photon resolution measured by the prototype using aerogel with different refractive index. The cluster of measurement at $n = 1.020$ is because several tiles with this refractive index were tested, and the result from the 2022 test beam was included.

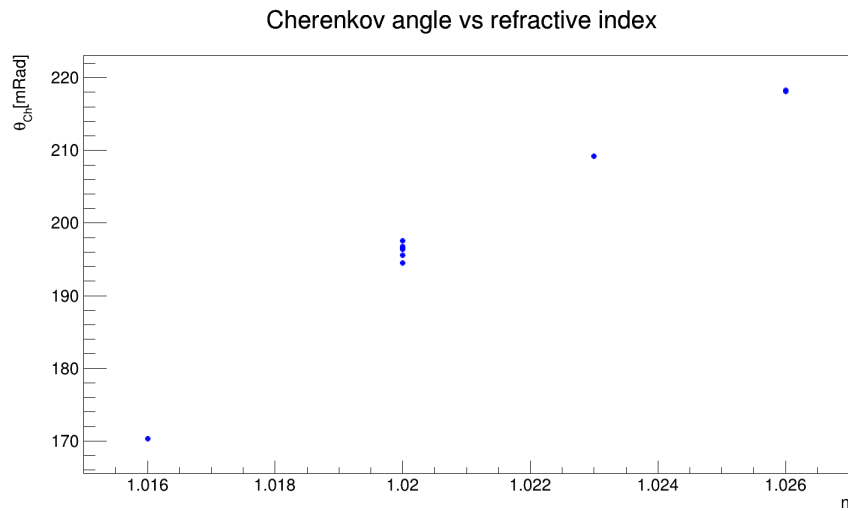


(b) Single particle resolution measured by the prototype using aerogel with different refractive index. The cluster of measurement at $n = 1.020$ is because several tiles with this refractive index were tested, and the result from the 2022 test beam was included.

Figure 4.29: Results of the aerogel study



(a) The number of photons for particles detected by the prototype using aerogel with different refractive indices. The cluster of measurement at $n = 1.020$ is because several tiles with this refractive index were tested, and the result from the 2022 test beam was included.



(b) Cherenkov angle measured by the prototype using aerogel with different refractive index. The cluster of measurement at $n = 1.020$ is because several tiles with this refractive index were tested, and the result from the 2022 test beam was included.

Figure 4.30: Results of the aerogel study

Single particle Cherenkov angle - Gas - $p_b = 20 \text{ GeV}/c$

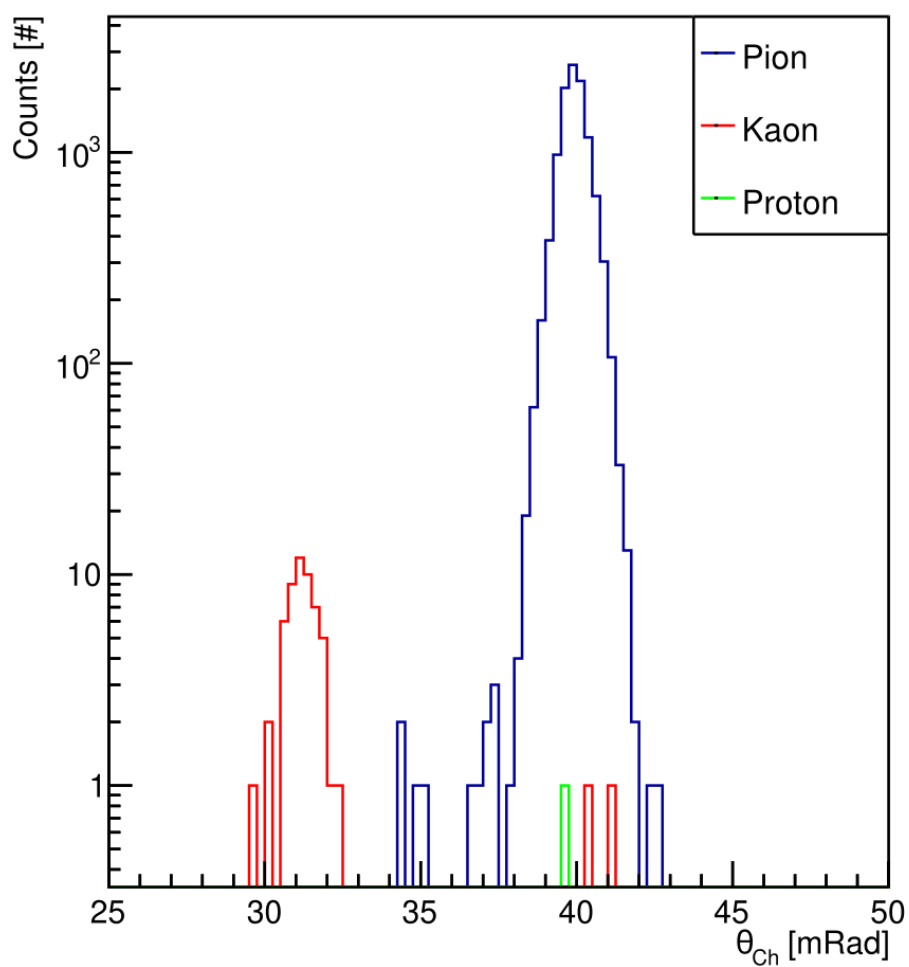


Figure 4.31: Distribution of the single-particle Cherenkov angle for gas photons, applying the tags of the beam PID system. The kaon peak is clearly separated from the pion peak. The proton does not produce a ring for $p_b = 20 \text{ GeV}$.

Single particle Cherenkov angle - Gas - $p_b = 50 \text{ GeV}/c$

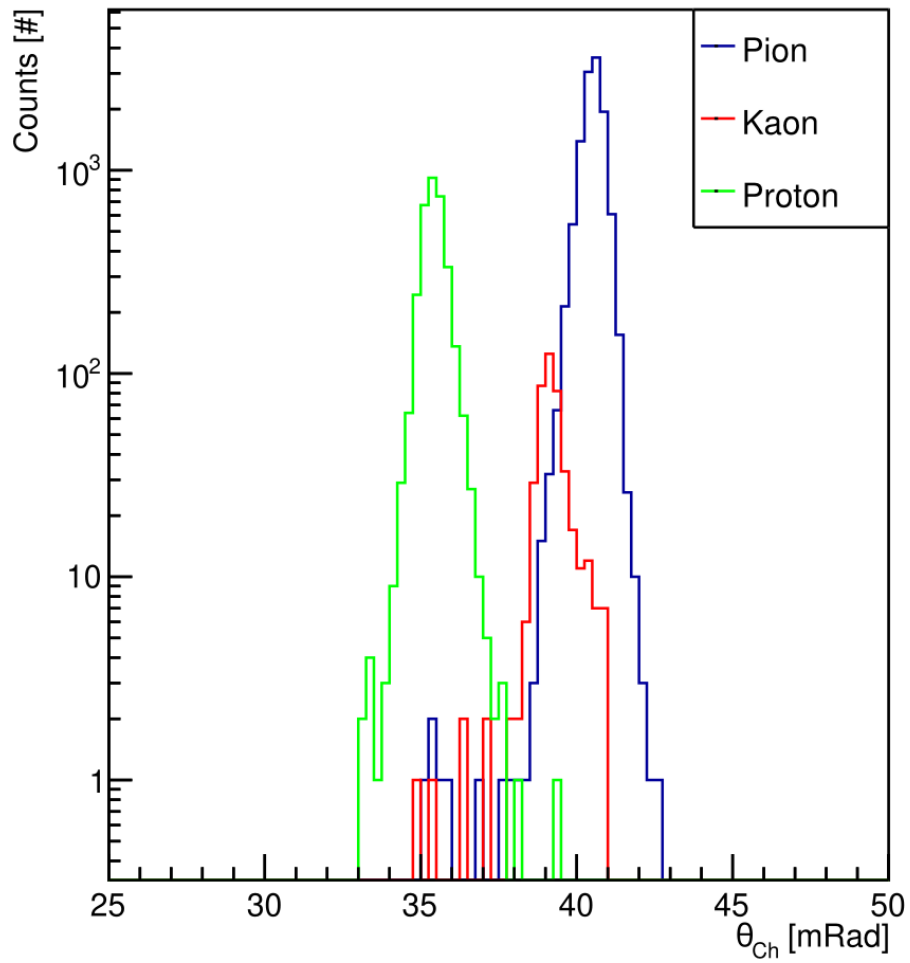


Figure 4.32: Distribution of the single-particle Cherenkov angle for gas photons, applying the tags of the beam PID system. The kaon peak is started merging into the pion peak. The proton peak is well separated from the others.

Single particle Cherenkov angle - Aerogel - $p_b = 6 \text{ GeV}/c$

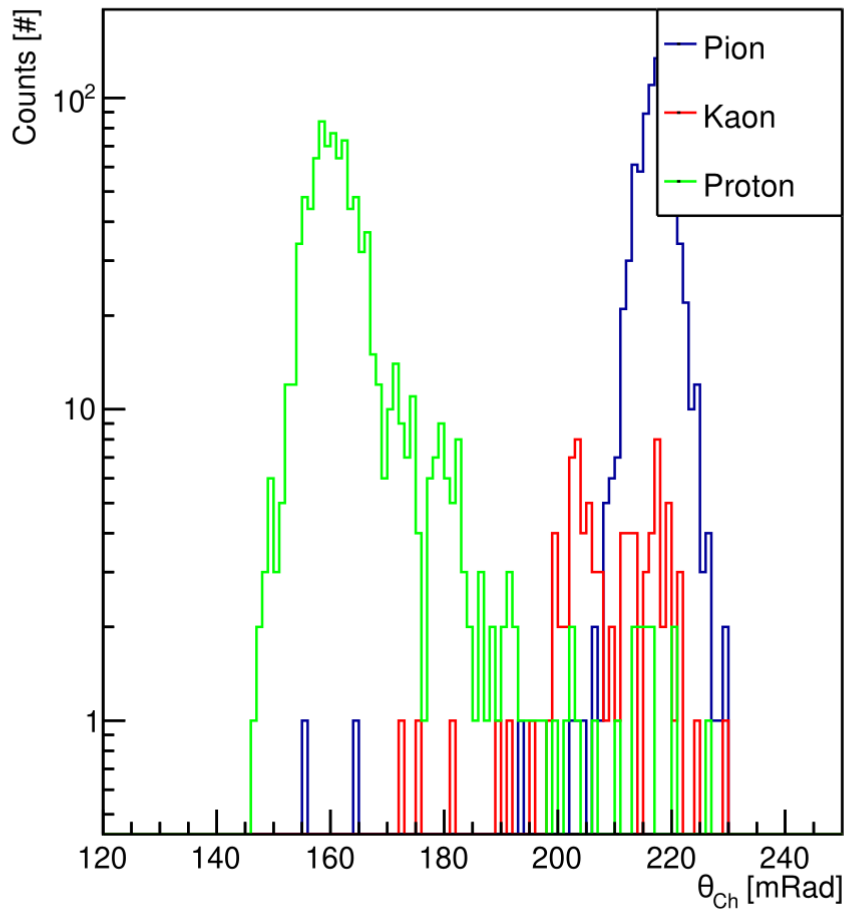


Figure 4.33: Distribution of the single-particle Cherenkov angle for aerogel photons, applying the tags of the beam PID system. The proton peak is well separated from the others. The kaon peak is visible at 205 mRad, although it is not so clear for the beam PID inefficiency.

Single particle Cherenkov angle - Aerogel - $p_b = 8 \text{ GeV}/c$

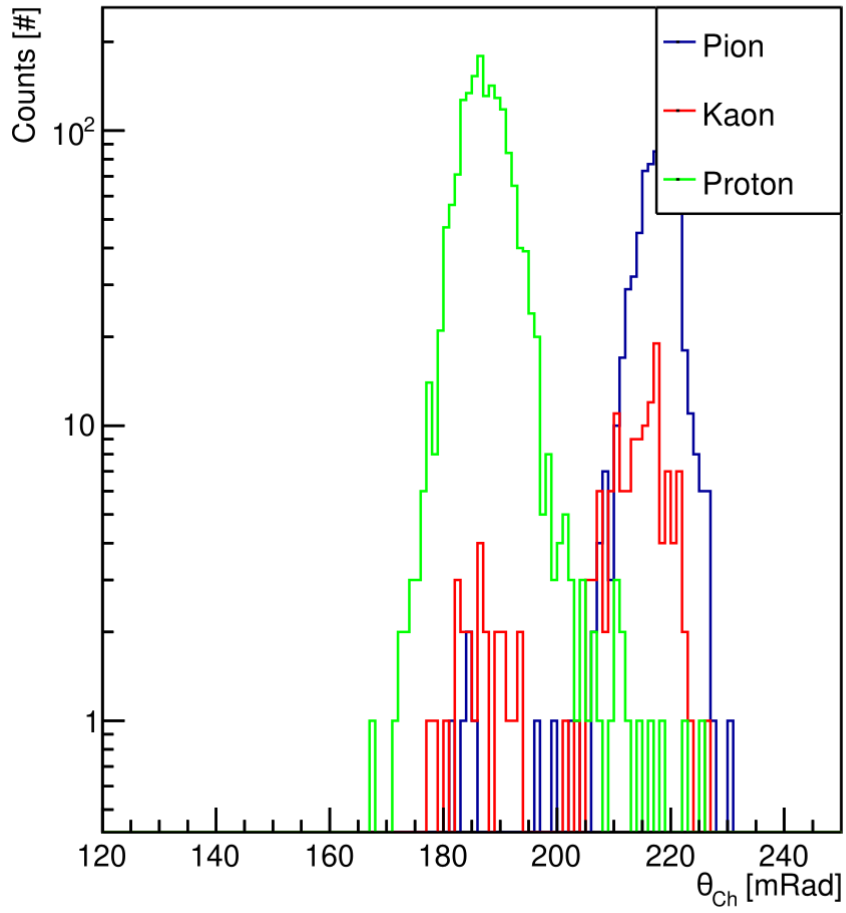


Figure 4.34: Distribution of the single-particle Cherenkov for aerogel photons, applying the tags of the beam PID system. The proton peak is well separated from the others. Although the kaon peak is visible, it started merging into the pion peak.

Single particle Cherenkov angle - Aerogel - $p_b = 10 \text{ GeV}/c$

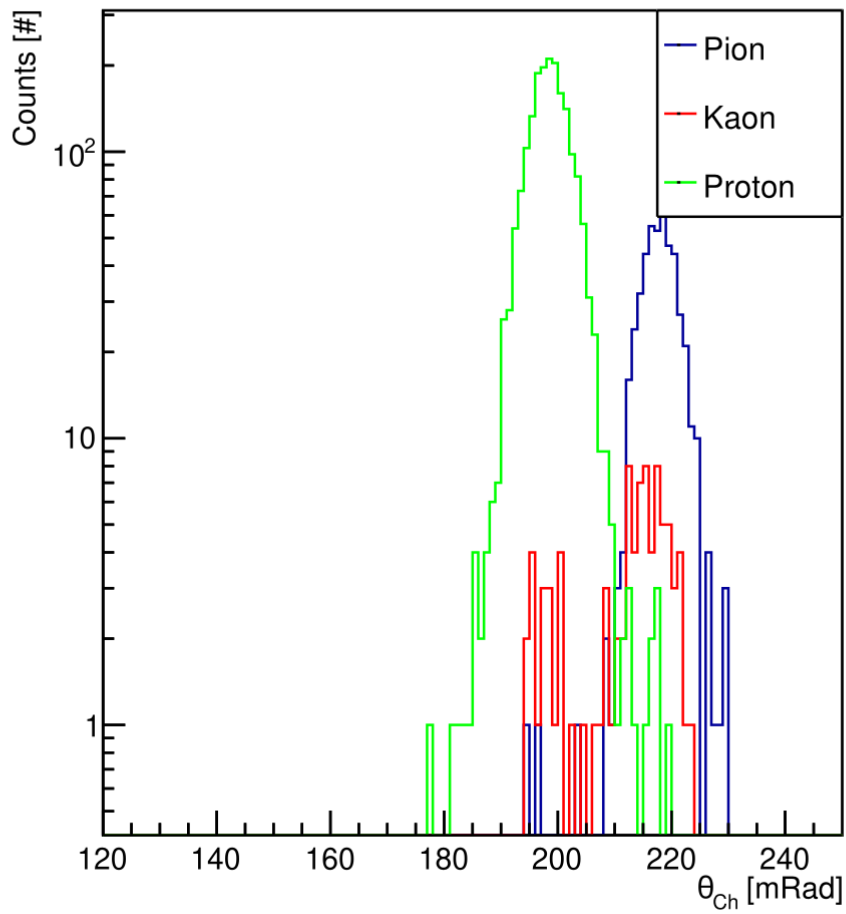


Figure 4.35: Distribution of the single-particle Cherenkov angle for aerogel photons, applying the tags of the beam PID system. The proton peak is well separated from the others. The kaon peak results inside of the pion peak.

dRICH is being designed by collaborating with several institutions led by the University of Ferrara and the INFN Ferrara division. This detector will face two main challenges: the broad momentum range in which the hadron must be identified and the intense background radiation that will damage the magnetic-insensitive photosensors SiPMs. For the last question, a study on recovering the photo-detectors via annealing provided good results, making us imagine the possibility of performing it directly in situ without removing the SiPMs.

A prototype was realized and tested between 2020 and 2023 to support the detector design phase. It allowed us to test the SiPM data acquisition and to measure the performance using a reference photon detector. The double rings were detected using the SiPM, and the SPE resolution measured for gas and aerogel is similar to the values expected from the simulation. These results support the capability to design and build the full detector, which will be confirmed with a new prototype currently being designed.

Conclusions

This chapter

Acronyms

ALCOR A Low Power Chip for Optical Sensor Readout.

BAND Back Angle Neutron Detector.

BNL Brookhaven National Laboratory.

BSA Beam-Spin Asymmetry.

CD Central Detector.

CEBAF Continuous Electron Beams Accelerator Facility.

CERN European Council for Nuclear Research.

CLAS12 CEBAF Large Acceptance Spectrometer for operation at 12 GeV.

CND Central Neutron Detector.

CTOF Central Time-Of-Flight.

CVT Central Vertex Tracker.

DC Drift Chamber.

DCR Dark Count Rate.

DESY Deutsches Elektronen-Synchrotron.

DIS Deep Inelastic Scattering.

dRICH dual-radiator Ring Imaging Cherenkov.

EC Electromagnetic Calorimeter.

EIC Electron-Ion Collider.

ePIC Electron-Proton/Ion Collider Experiment.

FBK Fondazione Bruno Kessler.

FD Forward Detector.

FF Fragmentation Function.

FFs Fragmentation Functions.

FT Forward Tagger.

FTOF Forward Time-Of-Flight.

GEM Gas Electron Multiplier.

GEMC GEant4 Monte-Carlo.

GPDs Generalized Parton Distributions.

HIPO Highly Performance Output.

HTCC High Threshold Cherenkov Counter.

INFN Istituto Nazionale di Fisica Nucleare.

JLab Jefferson Lab.

JLab Thomas Jefferson National Accelerator Facility.

LTCC Low Threshold Cherenkov Counter.

MAPMT Multi-Anode Photo-Multiplier.

MAPMTs Multi-Anode Photo-Multipliers.

MARCO MAgnet with Renewed COils.

MAROC Multi-Anode ReadOut Chip.

MPPC Multi-Pixel Photon Counter.

MPPCs Multi-Pixel Photon Counters.

PCAL Pre-shower Calorimeter.

PDF Parton Distribution Function.

PDF Probability Density Function.

PDFs Parton Distribution Functions.

PID Particle Identification.

PM Parton Model.

PS Proton Synchrotron.

QCD Quantum Chromodynamics.

QM Quark Model.

QPM Quark Parton Model.

RG-A Run Group A.

RG-B Run Group B.

RICH Ring Imaging Cherenkov.

SIDIS Semi-Inclusive Deep Inelastic Scattering.

SiPM Silicon Photo-Multiplier.

SiPMs Silicon Photo-Multipliers.

SLAC Stanford Linear Accelerator Center.

SPE Single PhotoElectron.

SPS Super Proton Synchrotron.

SSAs Single-Spin Asymmetries.

TMD Transverse-Momentum-Dependent distribution.

TMDs Transverse-Momentum-Dependent distributions.

UML Unbinned Maximum Likelihood.

Bibliography

- [1] E Aschenauer et al. “Optical characterization of $n=1.03$ silica aerogel used as radiator in the RICH of HERMES”. In: *Nuclear Instruments and Methods in Physics Research Section A: Accelerators, Spectrometers, Detectors and Associated Equipment* 440.2 (2000), pp. 338–347. ISSN: 0168-9002. DOI: [https://doi.org/10.1016/S0168-9002\(99\)00923-7](https://doi.org/10.1016/S0168-9002(99)00923-7). URL: <https://www.sciencedirect.com/science/article/pii/S0168900299009237>.
- [2] Alessandro Bacchetta et al. “Semi-inclusive deep inelastic scattering at small transverse momentum”. In: *Journal of High Energy Physics* 2007.02 (Feb. 2007), p. 093. DOI: 10.1088/1126-6708/2007/02/093. URL: <https://dx.doi.org/10.1088/1126-6708/2007/02/093>.
- [3] M. Contalbrigo et al. “Aerogel mass production for the CLAS12 RICH: Novel characterization methods and optical performance”. In: *Nuclear Instruments and Methods in Physics Research Section A: Accelerators, Spectrometers, Detectors and Associated Equipment* 876 (2017). The 9th international workshop on Ring Imaging Cherenkov Detectors (RICH2016), pp. 168–172. ISSN: 0168-9002. DOI: <https://doi.org/10.1016/j.nima.2017.02.068>. URL: <https://www.sciencedirect.com/science/article/pii/S0168900217302644>.
- [4] L. Re et al. “Characterization of three GEM chambers for the SBS front tracker at JLab Hall A”. In: *Radiation Effects and Defects in Solids* 173.9-10 (2018), pp. 818–828. DOI: 10.1080/10420150.2018.1528607. eprint: <https://doi.org/10.1080/10420150.2018.1528607>. URL: <https://doi.org/10.1080/10420150.2018.1528607>.
- [5] A. Airapetian et al. “Azimuthal single- and double-spin asymmetries in semi-inclusive deep-inelastic lepton scattering by transversely polarized protons”. In: *Journal of High Energy Physics* 2020.12 (2020). A comprehensive set of azimuthal single-spin and double-spin asymmetries in semi-inclusive lepto-production of pions, charged kaons, protons, and antiprotons from transversely polarized protons is presented. These asymmetries include the previously published HERMES results on Collins and Sivers asymmetries, the analysis of which has been extended to include protons and antiprotons and also to an extraction

in a three-dimensional kinematic binning and enlarged phase space. They are complemented by corresponding results for the remaining four single-spin and four double-spin asymmetries allowed in the one-photon-exchange approximation of the semi-inclusive deep-inelastic scattering process for target-polarization orientation perpendicular to the direction of the incoming lepton beam. Among those results, significant non-vanishing $\cos(\phi - \phi_S)$ modulations provide evidence for a sizable worm-gear (II) distribution, $g_{1T}^q(x, p_T^2)$. Most of the other modulations are found to be consistent with zero with the notable exception of large $\sin(\phi_S)$ modulations for charged pions and K^+ , p. 10. ISSN: 1029-8479. DOI: 10.1007/JHEP12(2020)010. URL: [https://doi.org/10.1007/JHEP12\(2020\)010](https://doi.org/10.1007/JHEP12(2020)010).

- [6] V. D. Burkert et al. “The CLAS12 Spectrometer at Jefferson Laboratory”. In: *Nucl. Instrum. Meth. A* 959 (2020), p. 163419. DOI: 10.1016/j.nima.2020.163419.
- [7] M. Contalbrigo et al. “The CLAS12 Ring Imaging Cherenkov detector”. In: *Nuclear Instruments and Methods in Physics Research Section A: Accelerators, Spectrometers, Detectors and Associated Equipment* 964 (2020), p. 163791. ISSN: 0168-9002. DOI: <https://doi.org/10.1016/j.nima.2020.163791>. URL: <https://www.sciencedirect.com/science/article/pii/S0168900220303235>.
- [8] M. Ungaro et al. “The CLAS12 Geant4 simulation”. In: *Nuclear Instruments and Methods in Physics Research Section A: Accelerators, Spectrometers, Detectors and Associated Equipment* 959 (2020), p. 163422. ISSN: 0168-9002. DOI: <https://doi.org/10.1016/j.nima.2020.163422>. URL: <https://www.sciencedirect.com/science/article/pii/S0168900220300279>.
- [9] T. B. Hayward. *Dihadron beam spin asymmetries on an unpolarized hydrogen target with CLAS12*. PhD thesis. 2021. URL: https://www.google.com/url?sa=t&rct=j&q=&esrc=s&source=web&cd=&ved=2ahUKEwjH19L5_4SEAxXFVPEDHTLyC_kQFnoECBMQAQ&url=https%3A%2F%2Fwww.jlab.org%2FHall-B%2Fgeneral%2Fthesis%2FTHayward_thesis.pdf%20usg=AOvVaw1ZQ96MA0ai8RhLwjbGSWnT&opi=89978449.
- [10] R. Abdul Khalek et al. “Science Requirements and Detector Concepts for the Electron-Ion Collider: EIC Yellow Report”. In: *Nuclear Physics A* 1026 (2022), p. 122447. ISSN: 0375-9474. DOI: <https://doi.org/10.1016/j.nuclphysa.2022.122447>. URL: <https://www.sciencedirect.com/science/article/pii/S0375947422000677>.
- [11] S. Diehl et al. “Multidimensional, High Precision Measurements of Beam Single Spin Asymmetries in Semi-inclusive π^+ Electroproduction off Protons in the Valence Region”. In: *Phys. Rev. Lett.* 128 (6 Feb.

- 2022), p. 062005. DOI: [10.1103/PhysRevLett.128.062005](https://doi.org/10.1103/PhysRevLett.128.062005). URL: <https://link.aps.org/doi/10.1103/PhysRevLett.128.062005>.
- [12] A. R. Altamura. *Aerogel characterization*. dRICH Meeting. 2023. URL: <https://indico.bnl.gov/event/19345/?print=1>.
- [13] Renaud Boussarie et al. *TMD Handbook*. 2023.
- [14] John Collins. *Foundations of Perturbative QCD*. Cambridge Monographs on Particle Physics, Nuclear Physics and Cosmology. Cambridge University Press, 2023.
- [15] Roberto Preghenella et al. “A SiPM-based optical readout system for the EIC dual-radiator RICH”. In: *Nuclear Instruments and Methods in Physics Research Section A: Accelerators, Spectrometers, Detectors and Associated Equipment* 1046 (2023), p. 167661. ISSN: 0168-9002. DOI: <https://doi.org/10.1016/j.nima.2022.167661>. URL: <https://www.sciencedirect.com/science/article/pii/S0168900222009536>.
- [16] S. Vallarino et al. “Prototype of a dual-radiator RICH detector for the Electron–Ion Collider”. In: *Nuclear Instruments and Methods in Physics Research Section A: Accelerators, Spectrometers, Detectors and Associated Equipment* 1058 (2024), p. 168834. ISSN: 0168-9002. DOI: <https://doi.org/10.1016/j.nima.2023.168834>. URL: <https://www.sciencedirect.com/science/article/pii/S0168900223008252>.
- [17] URL: <https://gemc.jlab.org/gemc/html/index.html>.
- [18] *Aerogel Factory Co*. URL: <https://www.aerogel-factory.jp/>.
- [19] *Composite Mirror Company*. URL: <https://www.compositemirrors.com/>.
- [20] *Evaporated Coatings Inc*. URL: <https://evaporatedcoatings.com/>.
- [21] *Media Lario Company*. URL: <https://www.medialario.com/>.
- [22] A. Vasilescu and G. Lindstroem. *Displacement damage in silicon, online compilation*. URL: <http://rd50.web.cern.ch/NIEL/>.